博士論文

Data-driven approach to images in natural science

（自然科学画像に対するデータ駆動的アプローチ）

中西（大野）　義典

Abstract

Various fields of natural science are abundant in image data and it was reported that there was the case where a method of image analysis in astronomy is effective in life science. Although the subjects of astronomy and life science are greatly different from each other, it is surprising that there is a common approach to image data analysis. Judging from such a situation, we suspect a universal principle of image analysis in natural science, independent of specific fields. This thesis introduces a variety of viewpoints to look for the principle and aims to innovate the whole of natural science.

Natural science has been done by building a hypothesis using measurement data and testing it by new experiment. Ironically, this natural repetition is stopped by the incredibly increasing amount of data due to advances in technology. On the other hand, computers and information science have made progress remarkably. We need a novel framework where information science and natural science cooperate to revive and bring back the traditional loop of hypothesis and testing to the present. We call such a framework *data-driven science*.

When people in information science and people in natural science try to collaborate, the following problems often arise. One is that there are too many methods developed in information science for people in natural science to select an adequate one. Another is that natural science is too subdivided for people in information science to understand all of the expert knowledge. In order to achieve a breakthrough, We propose the three levels of data-driven science as a guiding principle of data-driven science.

The three levels of data-driven science is highly influenced by David Marr ' s three levels at which any machine carrying out information processing should be discussed. The modeling level is newly inserted between the level of computational theory and the level of representation/algorithm, both of which are included in Marr ' s three levels, to form the three levels of data-driven science. At the level of computational theory, people in natural science discusses what to do in data analysis based on their own prior knowledge. At the level of representation/algorithm, people in information science develop an efficient solution to mathematically hard problems with the aid of computers. At the center level of modeling, people in natural science state clearly the goal and strategy of data analysis with as few a technical terms as possible. This helps the understanding of people in information science. Not only that, the discussion at the modeling level promotes the recognition of similar problems in different fields. What is most important is that all

the people share the fundamental problems accumulated at the modeling level, and recall at all times that such sophisticated problems are worth solving at all costs. The thesis presents three topics of modeling contributed by the author: Markov random field (MRF), compressed sensing and solution-space analysis.

It is important to extract latent variables from image data in natural science. In particular, the estimation of the diffusion coefficient of target phenomena is essential. We focus on the correspondence between the diffusion equation and MRF developed in the field of image processing, and explain a method for estimating the diffusion coefficient, proposed by the author.

MRF is used to model image data based on the knowledge that the target phenomenon is spatially smooth. For example, in image restoration, one introduces a regularization term, which imposes a penalty on pairs of adjacent pixels if their values are distant, to estimate the original image. The coefficient is called a hyperparameter and the performance is sensitive to its adjustment. Actually, this hyperparameter corresponds the diffusion coefficient. We stress that, in natural science, the diffusion coefficient itself is a significant quantity. The proposed method enables us to evaluate the confidence of data as well as to estimate the value of hyperparameters, using the framework of Bayesian inference.

The proposed method is unique in focusing on the posterior distribution itself. In particular, the posterior distribution of hyperparameters is calculated exactly regarding a minimum model needed to understand the diffusion phenomena. It is shown that the breadth of posterior distribution is used to evaluate the confidence of the data. Besides, the approximate posterior distribution obtained by the method of variational Bayes overestimates the confidence.

The purpose of compressed sensing is to reconstruct the original signal from a reduced amount of data by designing efficient experiment. We need to solve an underdetermined problem where the amount of data is smaller than the number of variables to be determined. The strategy adopted here is to assume the sparseness of the original signal. A signal is called to be sparse if there are few nonzero components. When the original signal is sure to be sparse, one can obtain it by selecting the sparsest one among a lot of solution candidates which could describe the measurement data.

We apply compressed sensing to the observation of quasiparticle interference using scanning tunneling microscopy/spectroscopy. This application is considered to be effective because the pattern of interference can be assumed to be sparse in Fourier space. This observation plays an important role in condensed matter physics. In addition, it is a really interesting subject in the context of compressed sensing. It is because complementary methods of experiment exist and the measuring system is controllable enough to adapt flexibly to newly designed experiments.

Specifically, we demonstrate whether, from a reduced amount of data, the circular pattern unique to electrons on the Ag(111) surface is reconstructed. First, without

utilizing the sparseness assumption, the pseudoinverse operation fails to obtain a proper Fourier-transformed image. Then, we examined the performance of LASSO (Least Absolute Shrinkage and Selection Operator), which prefers a sparse solution. In the case of data which are downsampled at regular intervals, even LASSO fails, but in the case of randomly reduced data, LASSO succeeds in compressed sensing. We show that the synergy between measurement methods and analysis methods is essential in the improvement of experiment.

When we try to obtain the posterior distribution of hyperparameters and the sparsest solution numerically, it causes the issue of combinatorial explosion. These problems have an energy function which has too a complex structure to be optimized using naive algorithms. In such a case, two approaches are conceived. One is to narrow the search space, such as the methods of variational Bayes in Bayesian inference. The other is to replace the energy function by a tractable one, such as the method of convex relaxation in sparse estimation. In order to take advantage of knowledge from information science, it is important to reveal the structure of solution space as well as the properties of these approaches.

The solution space is too high-dimensional to be visualized. Then, we focus on the density of states of solution space. The density of states is obtained by counting the number of states which realize a certain value of energy, and expressing the numbers as a function of energy.

We apply the analysis of the density of states to the problem of overcomplete sparse approximation. The purpose of overcomplete sparse approximation is to select a small number of basis vectors among a given overcomplete basis to approximate a given data as precisely as possible, using a linear combination of the selected basis vectors. This problem was proved to be NP-hard. We analyze the density of states in the large-size limit, using the replica method developed in statistical-mechanical informatics. Besides, the performances of two algorithms, called LASSO and OMP (Orthogonal Matching Pursuit), are examined and compared to the theoretical performance limit led by solution-space analysis. LASSO employs convex relaxation, and OMP employs the approach of narrowing the search space by neglecting collaboration effects of a certain pair of basis vectors. As a result, OMP outperforms LASSO, but does not achieve the performance limit.

In conclusion, we state the relation between the three research topics. It is easy to understand if the very deed of acquiring image data in natural science is discussed under the three levels of data-driven science. The goal of data acquisition is to see unseen objects. There are two strategies. One is to model target phenomena to extract latent structures from image data. The problem is how the model is approximated precisely to the reality and is addressed by the MRF study. The other is the attempt to measure target phenomena directly by well-calculated experiment. The problem is how such a difficult experiment is conducted efficiently and is addressed by the research of compressed sensing. Needless to say, the knowledge of the solution-space analysis is the key to both

of the problems. We discuss the modeling of phenomena, measurement, and analysis, and this triangle should be shared by natural science and information science. Consequently, data-driven science will be created.

Acknowledgements

Foremost, I would like to express my sincere gratitude to my supervisor Masato Okada for his constant support of my studies. I was often surprised at his unique insight, and later on, astonished again to find it consistent with his rigorous strategy. He let me instruct some of my juniors directly, for me to look objectively at myself. His advice, at first, seemed to be reckless, but it was deliberately made to allow me to exceed my self-imposed limitations.

My sincere thanks also goes to Kenji Nagata, the present assistant professor of my research group. He gave me a wealth of technical advice since my days as a master's student. He never hesitated to discuss my work with me, and encouraged me whenever I was frustrated with my work.

Next, I would like to express my appreciation to my collaborators: Hayaru Shouno, Yoshiyuki Kabashima, Tomoyuki Obuchi, Yukio Hasegawa, Yasuo Yoshida, Masahiro Haze, Koji Hukushima, Toshiaki Omori, Tatsu Kuwatani, and Yasuhiko Igarashi. The wide scope of my thesis is ascribed to the fruitful discussions with them from various viewpoints: experimental, theoretical, and computational physics; theoretical neuroscience; and mathematical geoscience.

In addition to the aforementioned thanks, I am deeply obliged to Masato Okada, Yukio Hasegawa, and the rest of my thesis committee: Masashi Sugiyama, Takehiko Sasaki, and Noboru Kunihiro. Their effective comments and hard questions were essential to make my thesis more complete.

Next, I am indebted to the support by JSPS KAKENHI (Grant Number 13J04920). I also appreciate the many opportunities I had to meet new people through the academic activities of JSPS Grant-in-Aid for Scientific Research on Innovative Areas, Initiative for High-Dimensional Data-Driven Science through Deepening of Sparse Modeling.

Moreover, I greatly thank all of my lab members and alumni. I am happy to share enjoyable times and discussions with them. In particular, I am really glad Hirotaka Sakamoto took over one of my research topics to develop it further with me. This experience allowed me to grow a lot.

Last but not least, I would like to heartily thank my family: my late grandmother 七三枝, my grandfather 誠太郎, my parents 進 and 幹枝, my adopted parents 達也 and 洋子, and my brother 正貴. Their implicit but warm care about my health and stress enables me to be devoted to my research life. I cannot thank them enough for every possible

support imaginable I have received and continue to receive since birth.

Contents

Chapter 1

Introduction

1.1 Image data and natural science

Seeing is believing. Image data often surprise and inspire us to believe what we could not be sure of. Wilhelm Röntgen took the first photograph of his wife's bones along with her ring, using X-ray [93]. This achievement made him the first laureate of the Nobel Prize in Physics in 1901. The photographic methods for elementary particles developed by Cecil Powell were used to demonstrate the existence of mesons that Hideki Yukawa already predicted [109, 69]. Gerd Binnig and Heinrich Rohrer invented STM (Scanning Tunneling Microscopy) to confirm the 7×7 reconstruction structure of the Si(111) surface that was a controversial topic in surface science for a long time [6, 7]. The scope of image data is not limited to physics. MRI (Magnetic Resonance Imaging) enables us to see the internal parts of a body without any radiation exposure [70]. The GFP (Green Fluorescent Protein) discovered by Osamu Shimomura enables us to visualize intracellular phenomena such as signal transduction in real time [97]. In geophysics and seismology, the seismic tomography reveals the three-dimensional geologic structure and advances our understanding of various dynamic processes in Earth [1, 50, 51, 48]. Modern astronomers are endeavoring to take a photograph of a black hole using an array of radio telescopes called ALMA (Atacama Large Millimeter/submillimeter Array) [25, 54, 4].

Various fields of natural science are abundant in image data due to recent progress in experimental and measurement techniques. Taking such an influential trend into account, one of the leading journals *Science* featured data science in 2011. This volume has an interesting article reporting interdisciplinary collaborations which were unusual in those days [91]. The article starts with two images: one is from astronomy, and the other is from medicine. The topics of these two disciplines are completely different, but the article introduces some cases where a medical method of data analysis was found to perform well in analyzing image data in astronomy, and vice versa. For example, an astronomer surveying star-forming regions wanted a three-dimensional view of the regions, but astronomers had no access to it using two-dimensional images. When the astronomer

presented her problem at a workshop, however, a radiologist in the audience recognized that the method needed in astronomy already existed in medicine. The method enables us to view the accumulation of tomographic data in three dimensions and was developed for use with medical scans such as MRIs. Their collaboration began immediately. On the other hand, there is a case where computer algorithms designed for picking out galaxies, nebulae, or star clusters in large batches of astronomical images were found to be useful in the hunt for cancer in medical images. After reading the article, one would probably notice that the first two images are similar to each other *somehow*.

It is expected that interdisciplinary collaborations will occur in other fields of natural science. In order to accomplish a lot of collaborations, we should reveal the background of the collaborations between astronomy and medicine reported in the article. We need to discuss the part of *somehow* in the similarity further. In the article, an astronomy student says that his data became amazingly more intuitive to understand when they were visualized in three dimensions with the above-mentioned medical software, for the first time. An oncologist involved with the collaboration says that, once noticed, astronomy and medicine may well have the same goal to identify and quantify obscure objects in a lot of image data, though their subjects are different. However, how can we pass by the scene of academic encounter, or take it as merely a surprise, much less as something natural? It is more natural to believe that fundamental principles of data analysis lie in various fields. This belief cannot be confirmed until we look out over the diversity in natural science without being trapped in a single discipline. It is indispensable, therefore, to discover something independent of different fields and then establish a universal framework for scientific image data. As a result, the whole of natural science will be innovated.

1.2 Data-driven science

Truthfully speaking, the innovation of natural science requires another collaboration. It is information science that should be incorporated as well. In earlier times, natural science was driven by scientists' intuition about data. For example, Johannes Kepler derived his laws of planetary motion from Tycho Brahe's data of astronomical observations. It was fortunate that something inspiring Kepler was included in Brahe's data, the amount of which was as small as a genius could manage by hand. Nowadays, an incredible amount of data is available, but ironically, many scientists are bewildered at this amount, never to make the most of their precious data. The only thing that we should do then, is to look somewhere else: the field of information science. The recent progress in information science has provided elaborate solutions to a variety of problems regarding data analysis, involving machine learning, information theory, artificial intelligence, statistical-mechanical informatics, and so forth. We will therefore establish a novel framework where information science and natural science are closely cooperated to revive and bring back the traditional loop of hypothesis and testing into the present. Let us call this framework *data-driven science*.

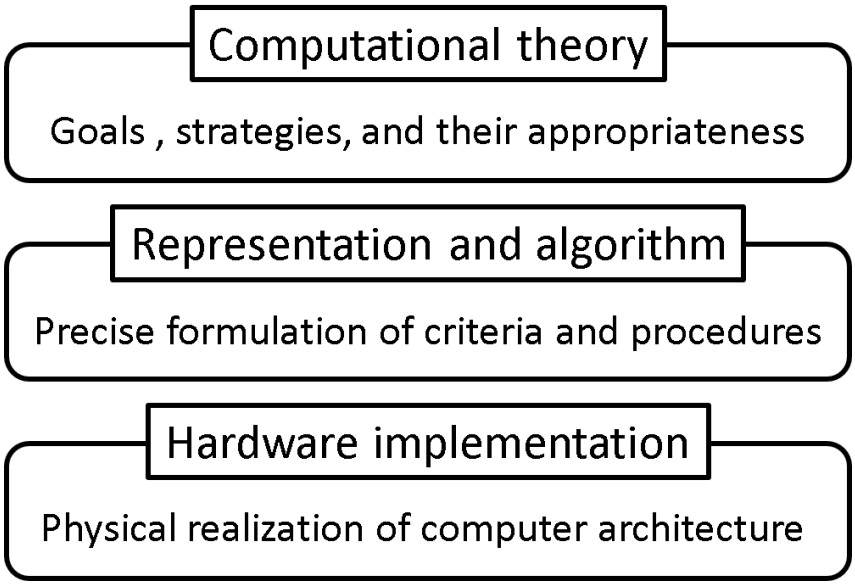

Figure 1.1: Marr's three levels where any machine of information processing should be understood.

It is important to remember Marr's three levels, when data-driven science is thought of as an information-processing system. David Marr, a neuroscientist, proposed in his book *Vision* [74], that any machine carrying out an information-processing task be understood at three different levels: computational theory, representation and algorithm, and hardware implementation, as shown in Fig. 1.1. At the first level of computational theory, the goal and strategy of information processing are clearly stated and their appropriateness is judged from given data and prior knowledge. At the second level of representation and algorithm, the procedure of information processing and the criterion for the evaluation of achievement are formulated mathematically or in an alternative way. At the third level of hardware implementation, the physical realization of information processing is discussed from the viewpoint of the detailed computer or brain architecture. The second and third levels are well-studied in information science and the translation between them is relatively smooth. However, most of the existing approaches to data-driven science lack sufficient communication between the first and second levels, in other words, that between natural science and information science. It is, therefore, most necessary to bridge the gap.

What we should do before anything else is to unravel the many-to-many correspondence between the two sciences. Natural science has been too subdivided for people in information science to follow everything technical in all the disciplines. Information science is also being split gradually. People in natural science are often at a loss as to what algorithms to use. Here, let us turn to the case of bioinformatics, a successful example of the collaboration between information science and a specific field of natural science. A goal of bioinformatics is, for example, to search the whole genome

for a small number of genes, with which a person is susceptible to a certain disease. The achievements of bioinformatics can be attributed to the smooth translation between the level of computational theory and the level of representation and algorithm. A genome is represented by only four letters, that is, adenine (A), cytosine (C), guanine (G), and thymine (T), and their sequences are suitable for sophisticated algorithms developed in the field of natural language processing. Bioinfomatics restricted itself to a one-to-one correspondence spontaneously from the very beginning.

Natural science abruptly gets crowded with a variety of *something informatics*, but it is doubtful whether all of them will perform well. In the case of bioinfomatics, the history of genome research was not so long, and humans had little knowledge about genetic code itself. Then, one had no choice but to adopt whatever might be useful in analyzing massive genetic data produced by high-throughput sequencing methods. On the other hand, most fields of natural science are built on a lot of previous discoveries. Elaborate algorithms, however fast they are, are not suitable for data analysis, if they do not match the goal and strategy derived from the known facts. Conversely, simple algorithms, however old-fashioned they are in a certain field, could be epoch-making in other fields. From the above argument, we can understand that it is inevitable to form common bases where people in different disciplines are brought together, in order to solve the problem of many-to-many correspondence.

Lately, the author, with his colleagues, proposed the *three levels of data-driven science* as a guiding principle of data-driven science as shown in Fig. 1.2 [58]. The concept of our three levels of data-driven science is highly influenced by Marr's three levels and composed of the level of computational theory, the level of modeling, and the level of representation and algorithm. The modeling level is newly inserted as the place where common bases of data-driven science are discussed. In the modeling level, researchers in natural science explain their goal and strategy with as few a technical terms as possible, and those in information science classify their methods systematically in accordance with the essential request offered by natural science. The common knowledge acquired at the modeling level enables researchers to recognize more frequently that methods developed for achieving a seemingly different goal can be effective in their own field, as reported in the article of *Science*. In this way, our three levels of data-driven science would probably connect natural science and information science.

1.3 Overview of Thesis

The thesis focuses on image data in natural science to promote data-driven science. We consider that there are three targets to be discussed at the modeling level: phenomena, measurement, and analysis. In accordance with them, we will explain three topics contributed by the author: Markov random field, compressed sensing, and solution-space analysis. Markov random field is used to model natural phenomena to estimate latent structures from image data. Compressed sensing makes many kinds of experiments

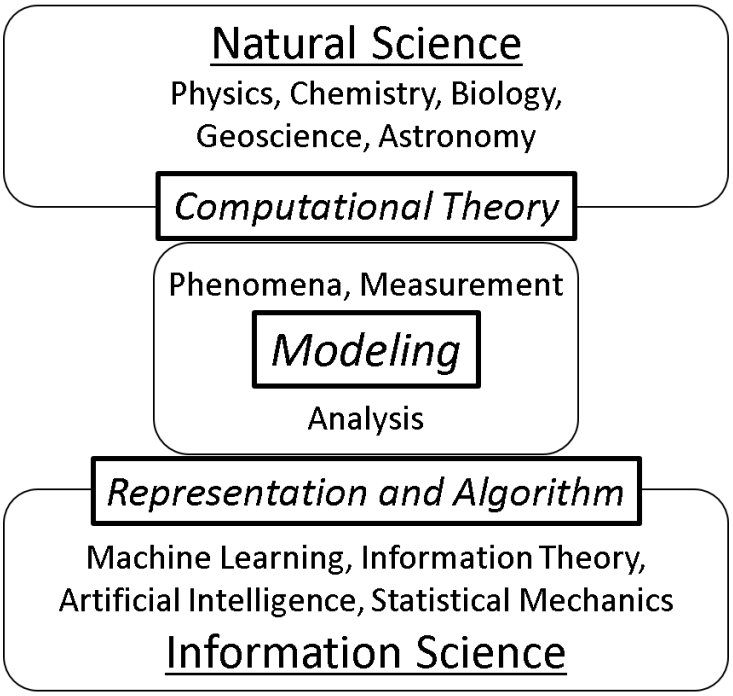

Figure 1.2: Three levels of data-driven science. The modeling level is inserted between the level of computational theory and the level of representation and algorithm.

efficient according to their measurement principles. Solution-space analysis provides a common basis where a lot of methods of data analysis should be compared.

1.3.1 Markov random field

Roughly speaking, natural phenomena are spatially and temporally continuous, and image data recording them are also smooth. Each pixel of scientific images is considered to take a value close to those of its adjacent pixels. Let us begin our discussion with this simple statistical property of image data. The proximity of neighbors is well described by Markov random field (MRF) developed in information science. MRF has been popular in the field of image processing since Stuart Geman and Donald Geman published their work in 1984 [41]. The task of image restoration by MRF is illustrated in Fig. 1.3. The energy function E is given by

$$E(\boldsymbol{x}|\boldsymbol{y}) = \frac{1}{2}\sum_i (y_i - x_i)^2 + \frac{\lambda}{2}\sum_i (x_{i+1} - x_i)^2, \tag{1.1}$$

where $\boldsymbol{x}$ is an original image, $\boldsymbol{y}$ is an observed image, and the estimated image is given by $\boldsymbol{x}$ that minimizes E. The concept of MRF is included in the second term. This

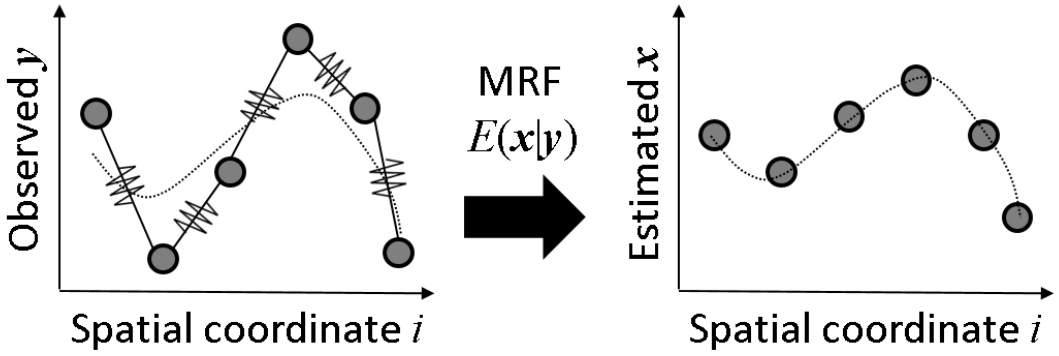

Figure 1.3: An illustration of image restoration by Markov random field. The energy function E is given by Eq. (1.1). The original image is recovered from the observed image as if the measured values of neighboring pixels were linked with springs.

regularization term has an effect of bringing the measured values of neighboring pixels close to each other, as if the values were linked with springs. The coefficient λ of the regularization term is called a regularization parameter, and it plays the role of adjusting the strength of springs.

MRF is very suitable for image analysis in natural science due to its equivalence with the diffusion equation [82]:

$$\frac{\partial \phi}{\partial t} = D \frac{\partial^2 \phi}{\partial x^2}, \tag{1.2}$$

where the time derivative is proportional to the second derivative with respect to space, and its proportionality constant is determined by the diffusion coefficient D. Now, let us consider $\boldsymbol{x}$ that minimizes the MRF term in Eq. (1.1). The method of steepest descent for this minimization is represented by

$$\frac{\partial x_i}{\partial t} = -\frac{\lambda}{2} \frac{\partial}{\partial x_i} \left[\sum_i (x_{i+1} - x_i)^2 \right]. \tag{1.3}$$

The right-hand side is calculated as follow:

$$\begin{aligned} & -\frac{\lambda}{2} \frac{\partial}{\partial x_i} \left[\cdots + (x_i - x_{i-1})^2 + (x_{i+1} - x_i)^2 + \cdots \right] \\ = \; & -\frac{\lambda}{2} \left[2(x_i - x_{i-1}) - 2(x_{i+1} - x_i) \right] \\ = \; & \lambda \left[(x_{i+1} - x_i) - (x_i - x_{i-1}) \right]. \end{aligned} \tag{1.4}$$

This result of calculation indicates a discretized second derivative with respect to space. Consequently, Eq. (1.3) corresponds to the diffusion equation (1.2), and the regularization parameter λ is nothing but the diffusion coefficient.

The estimation of the diffusion coefficient from image data is attractive as a primitive problem in natural science. It is well-known in information science that the framework of Bayesian inference is helpful in executing this [9]. Many methods of point estimation were proposed to determine the values of hyperparameters properly to improve the performance of image processing. Note that the variables corresponding to the regularization parameter is often called hyperparameters in the framework of Bayesian inference. However, these methods are not sufficient, because they miss the general goal of evaluating how much confidence one can say something scientific from the given data with. The estimate of the diffusion coefficient, a physical quantity, should be evaluated not only in terms of accuracy, but also in terms of reliability. The author, therefore, proposed a Bayesian method of distribution estimation [82]. This method enables us to calculate the posterior distribution itself of hyperparameters in MRF analytically, and to evaluate the confidence of data by the breadth of the distribution. MRF and this proposed method are explained in Chapter 2.

1.3.2 Compressed sensing

Indeed, MRF is a general tool for modeling natural phenomena described by diffusion processes. Besides, some fundamental equations include diffusion terms, such as the Navier-Stokes equations in fluid dynamics, and the Schrödinger equation in quantum mechanics. It could be possible to some extent to apply the concept of MRF to such an intricate system with a slight modification. However, there is a limit. For example, the formation mechanisms of internal organs, protein molecules, and black holes are difficult to be deduced from fundamental equations. What interests us then, is how image data of these things are obtained experimentally. Internal organs are scanned using MRI, protein molecules are investigated using NMR (Nuclear Magnetic Resonance), and black holes are observed by astronomical interferometers. Recently, it was reported that experiments of MRI, NMR, and interferometry could be more efficient by compressed sensing [72, 73, 61, 53, 54]. We are, therefore, curious about compressed sensing.

Figure 1.4 describes a very simple model of scientific measurements, formulated by

$$\boldsymbol{y} = \boldsymbol{A}\boldsymbol{x}, \tag{1.5}$$

where $\boldsymbol{y}$ is a data vector, $\boldsymbol{x}$ is an original signal, and $\boldsymbol{A}$ is a measurement marix. The problem addressed by compressed sensing is, in short, as to how to obtain the original signal from a reduced amount of data, as shown in Fig. 1.4. In the case where the data is scarce, the number of rows of the measurement matrix is decreased and the problem becomes underdetermined. The strategy of compressed sensing is to reduce the number of parameters to be estimated, by confidently assuming that the original signal $\boldsymbol{x}$ has a few nonzeros. This sparseness assumption can be justified by the derivation of Kepler's law, where a large amount of astronomical data is reduced to a few explanatory variables such as the orbital period, the semi-major axis of the orbit, and so forth. Anyway, one can recover the original signal from scarce data by techniques of compressed sensing.

Figure 1.4: An illustration of compressed sensing, formulated by $\boldsymbol{y} = \boldsymbol{A}\boldsymbol{x}$. The case where the data $\boldsymbol{y}$ is scarce, is dealt with by assuming that the original signal $\boldsymbol{x}$ is sparse.

To the best of our knowledge, the author is the first to apply compressed sensing to the observation of QPI (quasiparticle interference) using STM/S (scanning tunneling microscopy/spectroscopy) [84]. This experiment of physics is a really important target of compressed sensing for three reasons. The first reason is that the measurement principle of STM/S is Fourier transform, as well as that of MRI, NMR, and astronomical interferometry. Then, it is considered that the application of compressed sensing to STM/S performs well in a certain degree. The second reason is that experimental physics has more than one approaches to the same subject. In the case of QPI study, ARPES (angle-resolved photoemission spectroscopy) plays a complementary role to STM/S. From the viewpoint of computational physics, *ab initio* calculations can be used to confirm the experimental results. Unlike MRI or NMR studies, where the accuracy of data analysis is eventually judged by professionals, such as radiologists and biologists, there are some other evidence that supports the results of data analysis. The third reason is that STM/S measurments are flexible for the design of experiments. In the research of compressed sensing, it is often argued that the number of measurements can be reduced, but it is seldom discussed how to reduce it. In the first place, there are few places on Earth where astronomical observatories can be built, and there is little room to design measurement. On the other hand, STM/S enables us to measure the surface of materials at arbitrary locations. It means that we are able to examine the performance of efficient methods for compressed sensing, by putting them into practice. The theoretical aspect of compressed sensing is reviewed in Chapter 3, and our application of compressed sensing to STM/S measurements is explained in Chapter 4.

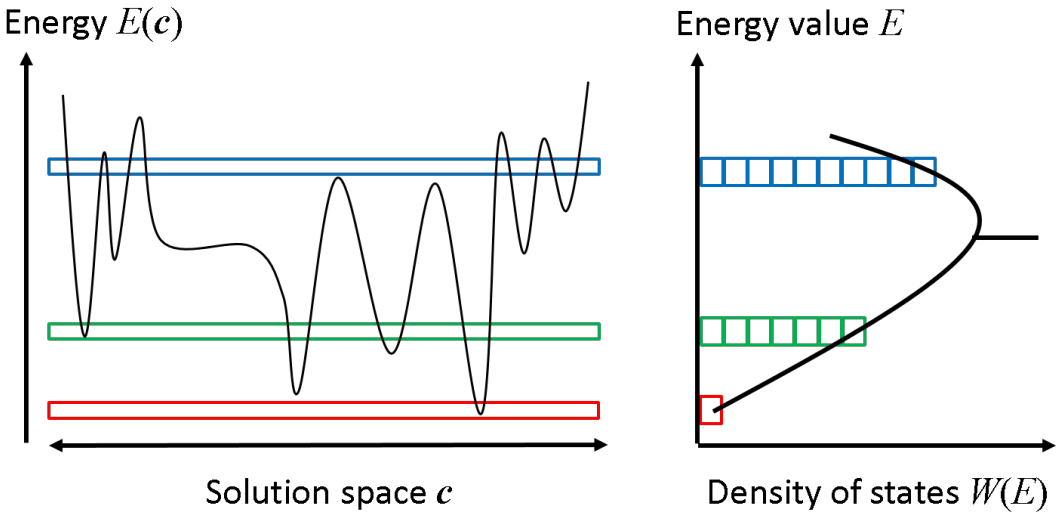

Figure 1.5: An illustration of solution-space analysis. The left shows the multi-valley landscape of a complex energy function $E(\boldsymbol{c})$ which has a lot of local optima. The right shows the density of states $W(E)$ standing for the solution space of the left. $W(E)$ counts the number of states $\boldsymbol{c}$ that satisfy $E(\boldsymbol{c}) = E$.

1.3.3 Solution-space analysis

The two topics so far are regarding image data itself and its measurement, both of which are motivated by the side of natural science. The other side of information science should be discussed at the modeling level. Information science provides so many methods for data analysis that people in natural science are often confused as to what method to use. Information science itself has begun to branch as shown in the lower part of Fig. 1.2, and then, some algorithms could perhaps be named differently among separate divisions. Our purpose here is to establish a common base where data-analysis methods are classified and compared systematically according to their goals. In order to achieve this purpose, we focus on analyzing the solution space itself, apart from conventional attempts to search for only the optimal solution.

Most of the difficult problems arise from the complexity of energy function (also called cost function and objective function). The left of Fig. 1.5 shows the landscape of an energy function, which has a multi-valley structure. If you try to optimize the energy function with the method of steepest descent, you will be trapped in any one of many local minima, never to reach the global minima. There are two representative approaches to manage such a situation. One is the restriction approach where the solution space to be searched is limited to some extent, such as the method of variational Bayes in Bayesian inference [3]. The other is the relaxation approach where the energy function is replaced by a more tractable one, such as convex relaxation of compressed sensing [18, 19]. Sometimes, either

will do, but in most cases, both will not perform well at the beginning. Then, we have to locate the cause of failure in the whole solution space.

It is true that the solution space is too high-dimensional to be visualized, but it is possible to see the density of states, as shown in the right of Fig. 1.5. When the solution space is characterized by $\boldsymbol{c}$ and the energy function is given by $E(\boldsymbol{c})$, the density of states $W(E)$ counts the number of states $\boldsymbol{c}$ which satisfy $E(\boldsymbol{c}) = E$, namely,

$$W(E) = \#\{\boldsymbol{c}|E(\boldsymbol{c}) = E\}, \tag{1.6}$$

where # is the cardinality of a set. All the solutions obtained by existing methods can be projected onto the density of states, and compared with each other. The shape of the density of states $W(E)$ would probably tell us the properties of the problem itself and the barriers which hinder existing methods from good performance. In particular, the author analyzed the solution space regarding the problem of overcomplete sparse approximation, by using methods of statistical mechanics [83]: the replica method as a theoretical tool [86] and the exchange Monte Carlo method as a numerical tool [99, 56]. This analysis is explained in detail in Chapter 5.

Chapter 2

Markov Random Field

2.1 Introduction

It is important to focus on spatial continuity often assumed to exist in a broad field of natural science. The Markov random field (MRF) approach is a useful method of representing the smoothness in image processing such as image restoration and image segmentation [41, 89, 101, 87, 82]. We will introduce the concept of MRF, giving cases of image restoration.

We consider cases where an original image $\boldsymbol{x} \in \mathbb{R}^N$ is estimated from an observed image $\boldsymbol{y} \in \mathbb{R}^N$. Figures 2.1 and 2.2 illustrate the one- and two-dimensional cases of image restoration, respectively. The naivest method of image restoration is to swallow the observed image as an estimator of the original image, formulated as the following minimization problem

$$\min_{\boldsymbol{x}} \left\{ \frac{1}{2} \sum_i (y_i - x_i)^2 \right\}. \tag{2.1}$$

However, this method causes over-fitting when the observed image has been blurred by measurement noise, shown in Figs. 2.1(b) and 2.2(b). Noise is considered to be added independently to each pixel of the observed noise and break the smoothness of the original image.

Regularization techniques are often employed to deal with the problem of over-fitting. Regularization is based on modifying the objective function by adding a regularization term which can be regarded as a penalty. According to the notion of MRF, differences between values of neighboring pixels should be punished in image restoration, as follows:

$$\min_{\boldsymbol{x}} \left\{ \frac{1}{2} \sum_i (y_i - x_i)^2 + \frac{\lambda}{2} \sum_{\langle i,j \rangle} (x_i - x_j)^2 \right\}, \tag{2.2}$$

where $\sum_{\langle i,j \rangle}$ represents summation over a set of all pairs of neighboring pixels. The second term is a regularization term, which has an effect of making values of neighboring pixels

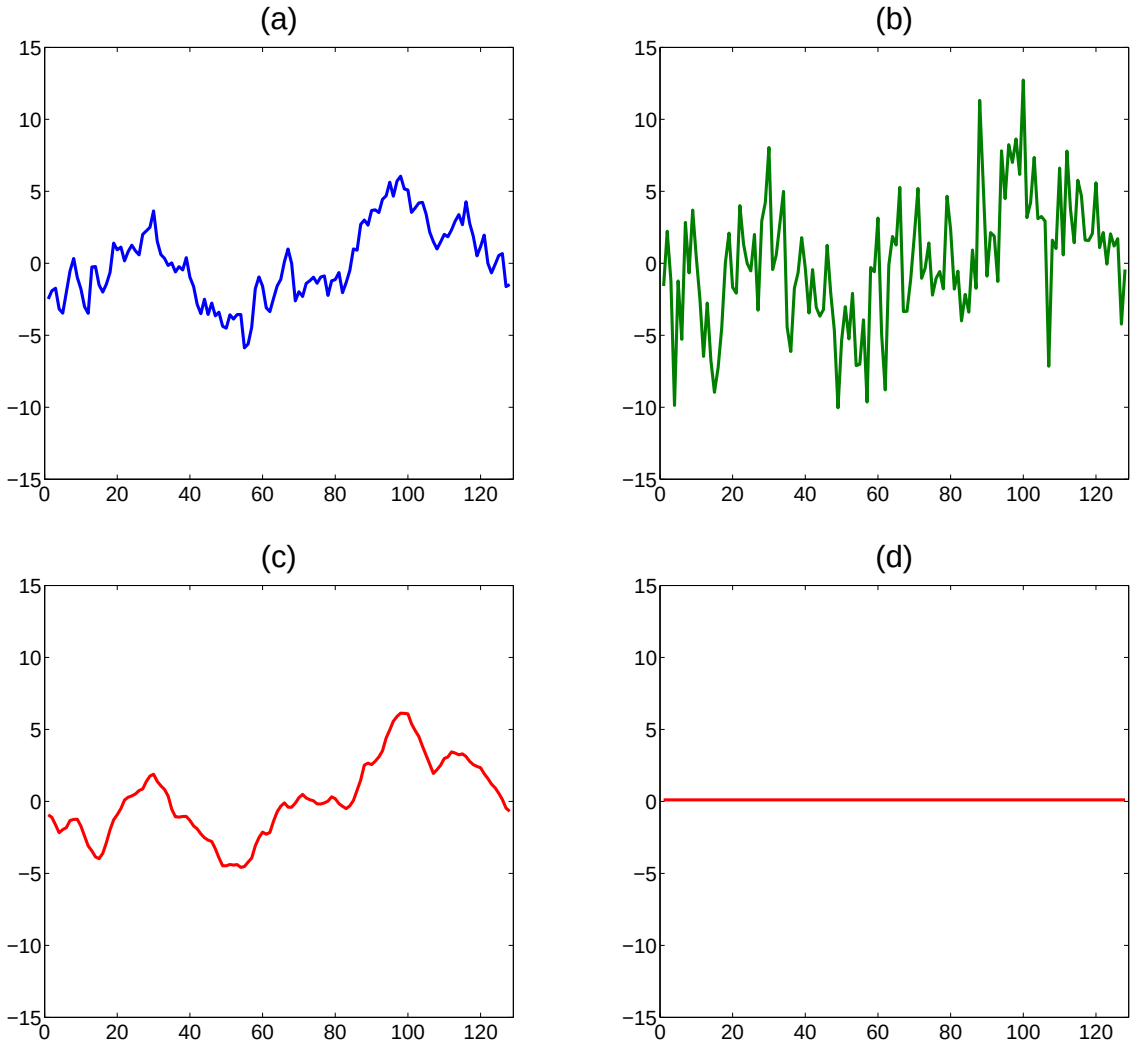

Figure 2.1: Image restoration by MRF is illustrated in the one-dimensional case. (a) Original image. (b) Observed image. (c) Estimated image with a proper value of the regularization parameter λ. (d) Estimated image with an infinitely large value of λ.

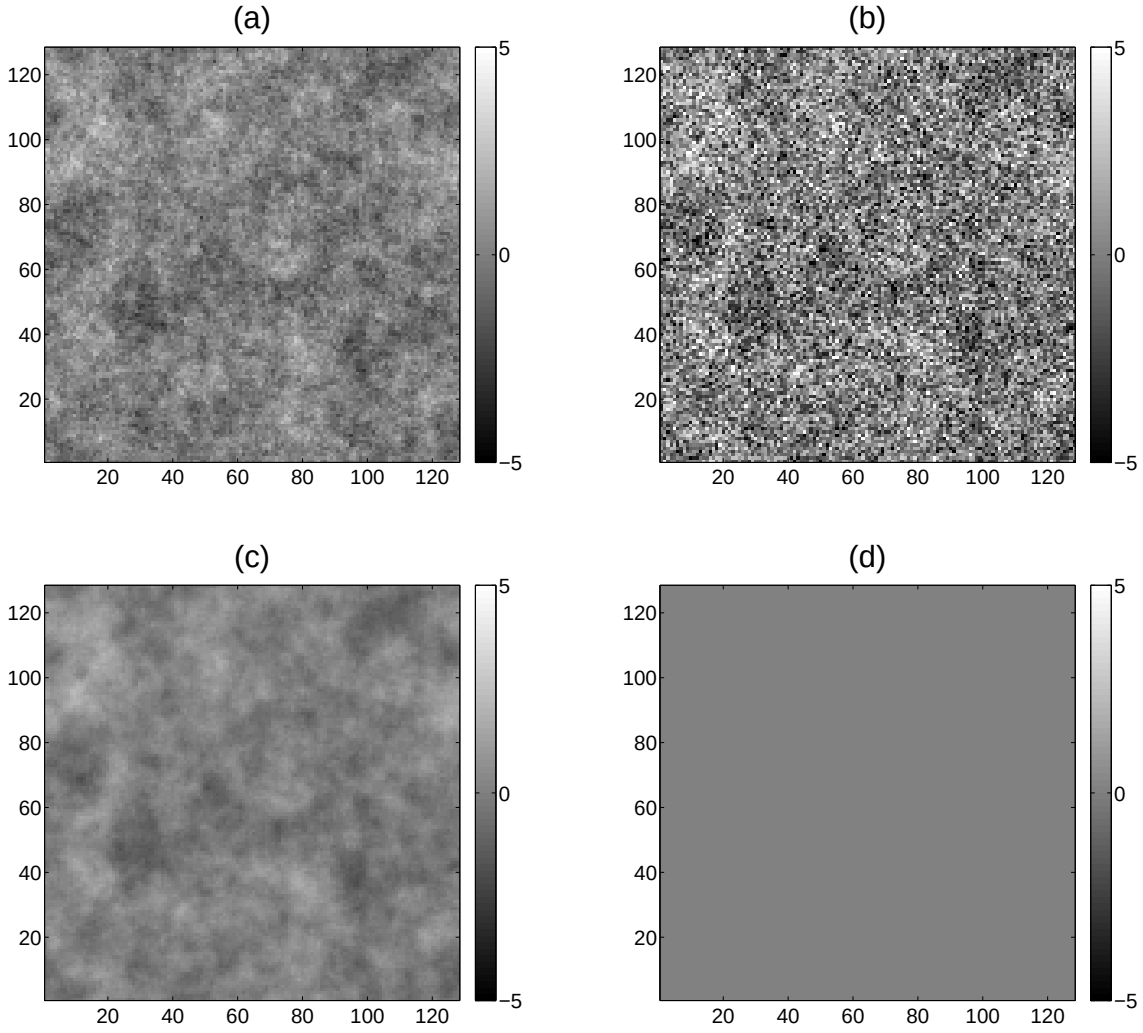

Figure 2.2: Image restoration by MRF is illustrated in the two-dimensional case. (a) Original image. (b) Observed image. (c) Estimated image with a proper value of the regularization parameter λ. (d) Estimated image with an infinitely large value of λ.

close to each other. The coefficient of the regularization term, λ, is called a regularization parameter.

The solution to the regularization problem can be obtained by using methods of linear algebra. The objective function of the problem (2.2) is also expressed as

$$E(\boldsymbol{x}; \boldsymbol{y}, \lambda) = \frac{1}{2}(\boldsymbol{y} - \boldsymbol{x})^{\mathrm{T}}(\boldsymbol{y} - \boldsymbol{x}) + \frac{\lambda}{2}\boldsymbol{x}^{\mathrm{T}}\boldsymbol{L}\boldsymbol{x}, \tag{2.3}$$

where $(\cdot)^{\mathrm{T}}$ represents the transpose of a matrix. The matrix $\boldsymbol{L}$ is known as a Laplacian matrix, whose components are given by

$$L_{ij} = \begin{cases} (\text{the number of neighboring pixels to } i) & \text{if } i = j \\ -1 & \text{if } i \text{ and } j \text{ are neighboring} \\ 0 & \text{otherwise} \end{cases}. \tag{2.4}$$

Minimizing the function (2.3), we obtain an estimator of the original image

$$\hat{\boldsymbol{x}}^{\mathrm{MRF}} = (\boldsymbol{I} + \lambda \boldsymbol{L})^{-1}\boldsymbol{y}, \tag{2.5}$$

where $\boldsymbol{I}$ is the identity matrix.

When the regularization parameter is set to a proper value, the solution (2.5) is a good estimator of the original image, as shown in Figs. 2.1(c) and 2.2(c). Nevertheless, the performance of image restoration depends highly on the value of the regularization parameter λ. If λ is set to zero, the regularization term plays no role, only to produce the same results with those of the naivest method. If λ is set to a too large value, the estimator is excessively smooth as shown in Figs. 2.1(d) and 2.2(d). In order to recover the original image, it is important to adjust the regularization parameter λ in a proper way. The framework of Bayesian inference helps us to understand the relation of this parameter λ to the observed image.

2.2 Bayesian inference

Bayesian inference is a methodology to tackle inverse problems such as image restoration [9]. In applying Bayesian inference, it is essential to make use of forward models and prior knowledge of target data. Therefore, we clarify the measurement process of image data before a Bayesian method of image restoration is explained.

Our measurement process of image data is illustrated by using a graphical model as shown in Fig. 2.3. In the measurement process, noise is added to each pixel of image data,

$$y_i = x_i + n_i, \tag{2.6}$$

where n_i denotes the noise term. When the measurement noise n_i can be regarded as independent and identically distributed Gaussian random variables, the measurement

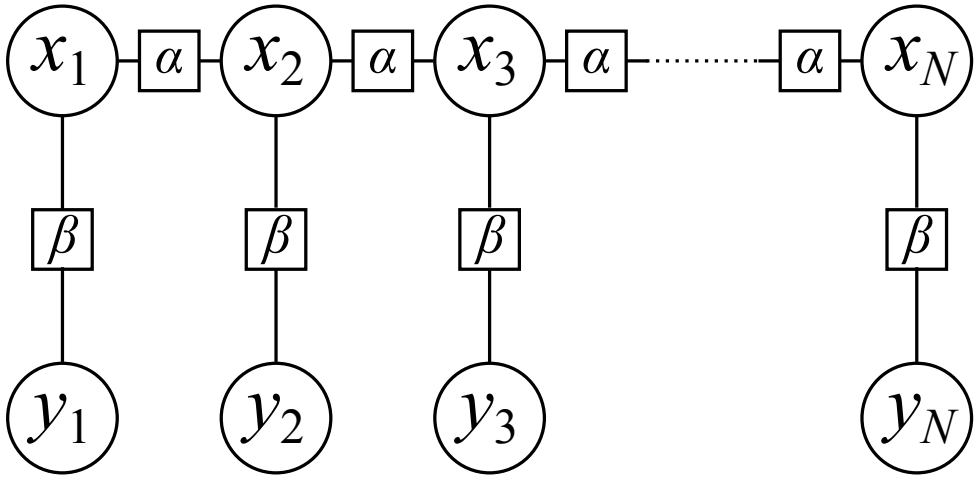

Figure 2.3: Graphical model of measurement process. The variables $\boldsymbol{x}$ and $\boldsymbol{y}$ represent an original image and an observed image, respectively. The variables α and β are hyperparameters in our model.

process is represented in a stochastic way as follows:

$$p(\boldsymbol{y}|\boldsymbol{x},\beta) = \frac{1}{Z_{\text{like}}(\boldsymbol{x},\beta)} \exp\left[-\frac{\beta}{2}\sum_i (y_i - x_i)^2\right]. \tag{2.7}$$

This probability distribution function is called a likelihood function in the context of Bayesian inference. The normalization factor Z_{like} is given by

$$Z_{\text{like}}(\boldsymbol{x},\beta) \;=\; \int \mathrm{d}\boldsymbol{y} \exp\left[-\frac{\beta}{2}\sum_i (y_i - x_i)^2\right]. \tag{2.8}$$

The parameter β represents the precision of measurement and is called a hyperparameter. When the value of β is larger, it means that the magnitude of noise is smaller.

An advantage of Bayesian inference is its ability to utilize prior knowledge of target objects. A useful knowledge for image restoration is the smoothness of the original image, which is represented as the following probability distribution function according to the notion of MRF,

$$p(\boldsymbol{x}|\alpha) = \frac{1}{Z_{\text{pri}}(\alpha)} \exp\left[-\frac{\alpha}{2}\sum_{\langle i,j\rangle} (x_i - x_j)^2\right]. \tag{2.9}$$

This probability distribution function is called a prior distribution in the context of

Bayesian inference. The normalization factor $Z_{\rm pri}$ is given by

$$Z_{\rm pri}(\alpha) \;=\; \int {\rm d}\boldsymbol{x} \exp\left[-\frac{\alpha}{2}\sum_{\langle i,j\rangle}(x_i - x_j)^2\right]. \tag{2.10}$$

The parameter α is another hyperparameter which represents the degree of smoothness of the original image. When the value of α is larger, there is a higher probability that the original image has a lot of pairs of neighboring pixels whose values are close to each other.

Bayesian inference is carried out on the basis of posterior distributions, which are calculated from likelihood functions and prior distributions. According to Bayes' theorem, we are able to calculate posterior distributions of the original image $\boldsymbol{x}$ given an observed image $\boldsymbol{y}$ as follows:

$$p(\boldsymbol{x}|\boldsymbol{y},\beta,\alpha) = \frac{p(\boldsymbol{y}|\boldsymbol{x},\beta)p(\boldsymbol{x}|\alpha)}{p(\boldsymbol{y}|\beta,\alpha)}. \tag{2.11}$$

The denominator of the right-hand side of Eq. (2.11) is also calculated by using likelihood functions and prior distributions as follows:

$$p(\boldsymbol{y}|\beta,\alpha) = \int {\rm d}\boldsymbol{x} p(\boldsymbol{y}|\boldsymbol{x},\beta)p(\boldsymbol{x}|\alpha). \tag{2.12}$$

Bayes' theorem (2.11) claims direct connection between posterior distributions, the key to inverse problems, and generative models of data represented as likelihood functions and prior distributions, and hence it seems as if we could trace back along the law of causality with the help of the theorem.

Maximum *a posteriori* estimation is a Bayesian method of image restoration and it is conducted by maximizing the posterior distribution as follows:

$$\hat{\boldsymbol{x}}^{\rm MAP} = \mathop{\rm argmax}_{\boldsymbol{x}} \left\{p(\boldsymbol{x}|\boldsymbol{y},\beta,\alpha)\right\}. \tag{2.13}$$

In our model, the posterior distribution is given by

$$p(\boldsymbol{x}|\boldsymbol{y},\beta,\alpha) \propto \exp\left[-\frac{\beta}{2}\sum_{i}(y_i - x_i)^2 - \frac{\alpha}{2}\sum_{\langle i,j\rangle}(x_i - x_j)^2\right], \tag{2.14}$$

substituting Eqs. (2.7) and (2.9) into Eq. (2.11). Comparing maximum *a posteriori* estimation with the regularization approach (2.2), we see that both methods yield the same estimator on condition that the regularization parameter λ is set to be equal to the ratio of hyperparameters, α/β. A different point between the two methods is that there is a framework of hyperparameter estimation in Bayesian inference. This framework allows us to determine hyperparameters, which can be regarded as the regularization parameter, in an objective way from image data.

2.3 Hyperparameter estimation

Our purpose is to launch and promote image data-driven sciences beyond ordinary image processing. Then, let us discuss the physical significance of hyperparameters in our forward model [82]. Our MRF model is related with the following stochastic diffusion equation,

$$\frac{\partial \phi}{\partial t}(x,t) = D\frac{\partial^2 \phi}{\partial x^2}(x,t) + \zeta(x,t), \tag{2.15}$$

where ϕ is a scalar field and ζ represents stochastic fluctuations whose correlations are given by

$$\langle \zeta(x_1,t_1)\zeta(x_2,t_2)\rangle = \sigma^2\delta(x_1-x_2)\delta(t_1-t_2). \tag{2.16}$$

In the limit $t \to +\infty$, we obtain

$$\left\langle \frac{\partial \phi}{\partial x}(x_1,t)\frac{\partial \phi}{\partial x}(x_2,t)\right\rangle \ \ \to \ \ \frac{\sigma^2}{2D}\delta(x_1-x_2), \tag{2.17}$$

though the detail of calculation is explained in Appendix A. The coefficient of the right-hand side of Eq. (2.17), $\sigma^2/(2D)$, is the variance of spatial derivative values of ϕ and, comparing with Eq. (2.9), the hyperparameter α is considered to be directly proportional to the parameter D called the diffusion coefficient. Hyperparameters are often regarded as mere tuning parameters in image processing, but it should be stressed that they play an important role of physical parameters which are used to explain the dynamics of target objects. Therefore, we have to estimate hyperparameters not only by point estimators but also with error-bars in order to evaluate the confidence of measurement. The framework of Bayesian inference enables us to do such a thing.

We start here to explain a Bayesian method of hyperparameter estimation. The key function is a posterior distribution of hyperparameters given image data, $p(\alpha,\beta|\boldsymbol{y})$. According to Bayes' theorem, we obtain

$$p(\alpha,\beta|\boldsymbol{y}) \propto p(\boldsymbol{y}|\beta,\alpha)p(\beta,\alpha). \tag{2.18}$$

The probability function $p(\beta,\alpha)$ is a prior distribution of hyperparameters and we employ a uniform prior

$$p(\beta,\alpha) \propto \text{constant}, \tag{2.19}$$

assuming that there is no prior knowledge of hyperparameters. We substitute Eqs. (2.12) and (2.19) into Eq. (2.18) to obtain

$$p(\alpha,\beta|\boldsymbol{y}) \propto \int \mathrm{d}\boldsymbol{x} p(\boldsymbol{y}|\boldsymbol{x},\beta)p(\boldsymbol{x}|\alpha). \tag{2.20}$$

At a glance, we get aware of a multiple integral in the right-hand side of Eq. (2.20). This operation of integration, called marginalization, is essential to hyperparameter estimation, because in order to estimate latent variables we have to take all the cases of ordinary parameters such as $\boldsymbol{x}$ into consideration.

We substitute our model into Eq. (2.20) to obtain

$$\begin{aligned} p(\alpha, \beta|\boldsymbol{y}) \quad \propto \quad & \int \mathrm{d}\boldsymbol{x} \frac{1}{Z_{\mathrm{like}}(\boldsymbol{x}, \beta)} \exp\left[-\frac{\beta}{2}\sum_i (y_i - x_i)^2\right] \\ & \times \frac{1}{Z_{\mathrm{pri}}(\alpha)} \exp\left[-\frac{\alpha}{2}\sum_{\langle i,j\rangle}(x_i - x_j)^2\right]. \end{aligned} \tag{2.21}$$

Our generative model is based on normal distributions, and therefore we are able to marginalize the parameters $\boldsymbol{x}$ analytically, by using Gaussian integral,

$$\int \mathrm{d}x \mathrm{e}^{-\frac{a}{2}x^2} = \sqrt{\frac{2\pi}{a}} \tag{2.22}$$

Results of the calculation are given by

$$p(\alpha, \beta|\boldsymbol{y}) \propto \prod_{k=1}^{N} \sqrt{\frac{\beta\alpha}{\beta + \alpha l_k}} \exp\left[-\frac{1}{2}\frac{\beta\alpha l_k}{\beta + \alpha l_k}|\tilde{y}_k|^2\right]. \tag{2.23}$$

The variables l_k $(k = 1, \ldots, N)$ are eigenvalues of the Laplacian matrix $\boldsymbol{L}$ defined by Eq. (2.4). The matrix $\boldsymbol{L}$ is a Hermitian matrix and can be diagonalized by a unitary matrix $\boldsymbol{P}$ as follows:

$$\boldsymbol{P}^* \boldsymbol{L} \boldsymbol{P} = \mathrm{diag}(l_1, l_2, \ldots, l_N), \tag{2.24}$$

where $(\cdot)^*$ is the conjugate transpose of a matrix and $\mathrm{diag}(\cdot)$ represents a diagonal matrix. The vector $\tilde{\boldsymbol{y}} = (\tilde{y}_1, \tilde{y}_2, \ldots, \tilde{y}_N)^{\mathrm{T}}$ is given by

$$\tilde{\boldsymbol{y}} = \boldsymbol{P}^* \boldsymbol{y}. \tag{2.25}$$

In more general cases where an original image $\boldsymbol{x}$ is observed more than once to obtain a set of image data $\{\boldsymbol{y}^t\} = \{\boldsymbol{y}^1, \boldsymbol{y}^2, \ldots, \boldsymbol{y}^T\}$, the measurement process is expressed as

$$p(\{\boldsymbol{y}^t\}|\beta, \alpha) = \int \mathrm{d}\boldsymbol{x} \left\{\prod_{t=1}^{T} p(\boldsymbol{y}^t|\boldsymbol{x}, \beta)\right\} p(\boldsymbol{x}|\alpha). \tag{2.26}$$

According to Bayes' theorem, the posterior probability is given by

$$\begin{aligned} & p(\alpha, \beta|\{\boldsymbol{y}^t\}) \\ \propto \quad & \prod_{k=1}^{N} \sqrt{\frac{\beta\alpha}{\beta T + \alpha l_k}} \exp\left[-\frac{1}{2}\frac{\beta\alpha l_k}{\beta + \alpha l_k}|\tilde{y}_k^{\mathrm{ave}}|^2\right] \beta^{\frac{T-1}{2}} \exp\left[-\frac{\beta(T-1)}{2}(\tilde{y}_k^{\mathrm{std}})^2\right], \end{aligned} \tag{2.27}$$

where

$$\tilde{y}_k^{\rm ave} = \frac{1}{T}\sum_t \tilde{y}_k^t, \tag{2.28}$$

$$\tilde{y}_k^{\rm std} = \sqrt{\frac{1}{T-1}\sum_t |\tilde{y}_k^t - \tilde{y}_k^{\rm ave}|^2}. \tag{2.29}$$

Our method of hyperparameter estimation is based on the posterior distribution, Eq. (2.27), derived analytically. The posterior distribution has more information than point estimators, such as the maximum likelihood estimator, do. For example, the breadth of posterior distribution is expected to reflect the confidence of measurement. We will examine the performance of our method of hyperparameter estimation by numerical simulation in the following section.

2.4 Numerical simulation

We evaluate our Bayesian method of hyperparameter estimation by numerical simulation. In this section, for the sake of simplicity, original images are assumed to satisfy periodic boundary conditions. On this assumption, the discrete Fourier transform can be used as a diagonalization matrix of the Laplacian matrix, namely $\boldsymbol{P}$ in Eq. (2.24).

We examine the case of two-dimensional images. In simulations, we generate image data which follow Eqs. (2.7) and (2.9) and calculate posterior distributions based on Eq. (2.27), substituting values of the synthetic data into $\{\boldsymbol{y}^t\}$. The number of pixels of image data is set to $N = 128^2$. The true values of hyperparameters are set to $(\alpha_0, \beta_0) = (1, 0.03)$. Figure 2.4 shows joint posterior distributions $p(\alpha, \beta|\{\boldsymbol{y}^t\})$, and Figs. 2.5 and 2.6 show marginalized posterior distributions of α and those of β, respectively defined by

$$p(\alpha|\{\boldsymbol{y}^t\}) = \int p(\alpha, \beta|\{\boldsymbol{y}^t\})\mathrm{d}\beta, \tag{2.30}$$

$$p(\beta|\{\boldsymbol{y}^t\}) = \int p(\alpha, \beta|\{\boldsymbol{y}^t\})\mathrm{d}\alpha. \tag{2.31}$$

In these figures, we see that the location of posterior distributions is closer to the true value as the number of measurements, T, increases. Figure 2.7 shows the posterior mean values of hyperparameters, defined by such as

$$\hat{\alpha}^{\rm PM} = \langle\alpha\rangle_{\alpha,\beta|\{\boldsymbol{y}^t\}} = \int \alpha p(\alpha, \beta|\{\boldsymbol{y}^t\})\mathrm{d}\alpha\mathrm{d}\beta, \tag{2.32}$$

$$\hat{\beta}^{\rm PM} = \langle\beta\rangle_{\alpha,\beta|\{\boldsymbol{y}^t\}} = \int \beta p(\alpha, \beta|\{\boldsymbol{y}^t\})\mathrm{d}\alpha\mathrm{d}\beta. \tag{2.33}$$

We see that, in both cases of α and β, posterior mean gets closer to the true value and its standard deviation decreases as the number of image data used in estimation increases.

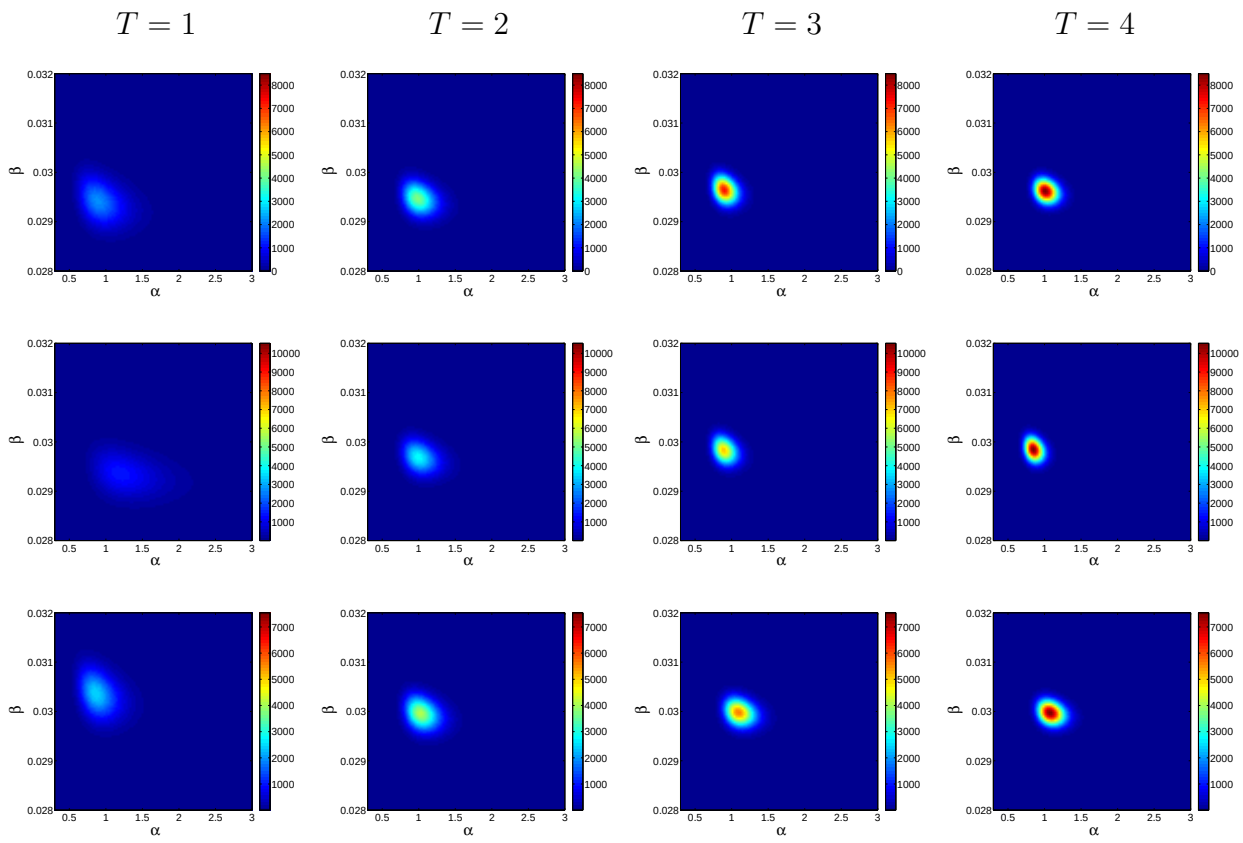

Figure 2.4: Joint posterior distributions of (α, β) calculated from two-dimensional observed images. The horizontal and vertical axes represent α and β, respectively. Cases of $T = 1, 2, 3, 4$ are listed from the left to the right. Distributions in the same row are obtained by the same original image. The true values of hyperparameters are set to $(\alpha_0, \beta_0) = (1, 0.03)$. The number of pixels of image data is set to $N = 128^2$.

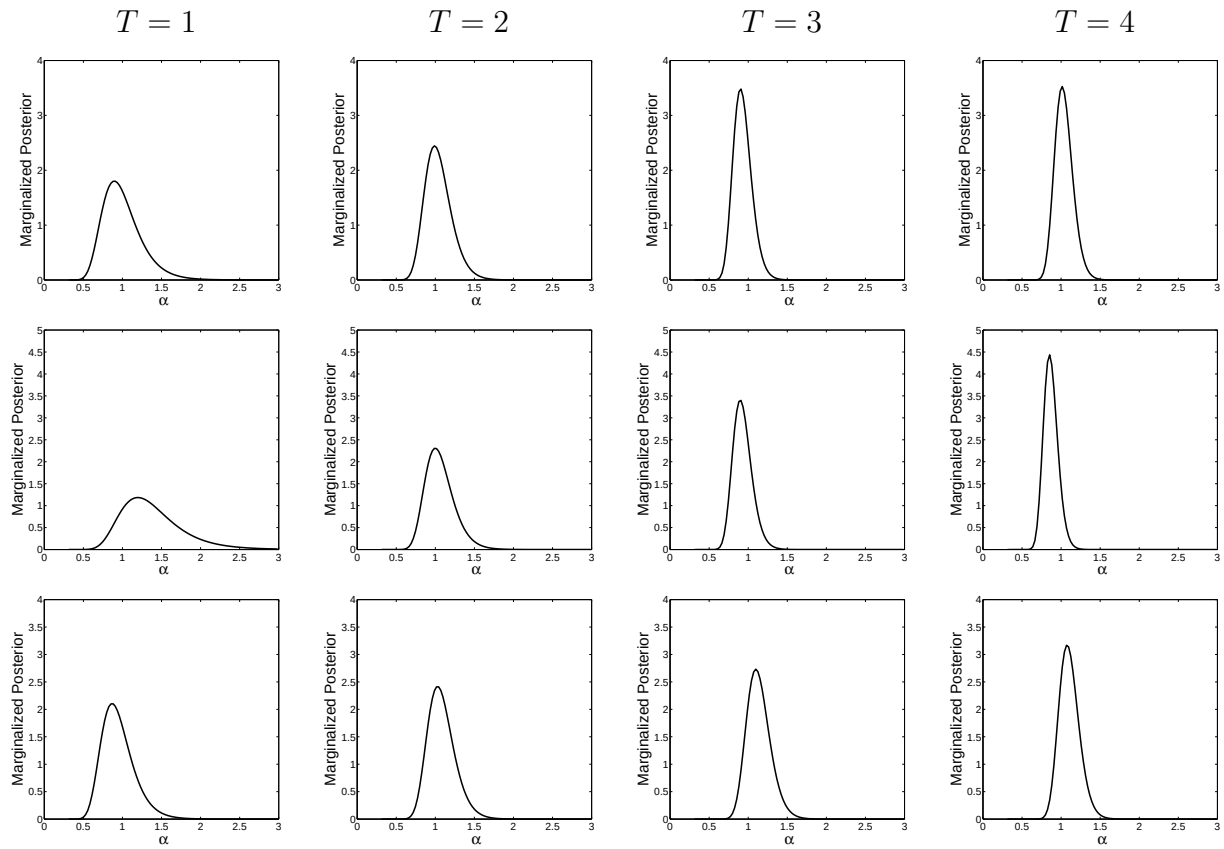

Figure 2.5: Marginalized posterior distributions of α calculated from two-dimensional observed images. Cases of $T = 1, 2, 3, 4$ are listed from the left to the right. Distributions in the same row are obtained by the same original image. The true values of hyperparameters are set to $(\alpha_0, \beta_0) = (1, 0.03)$. The number of pixels of image data is set to $N = 128^2$.

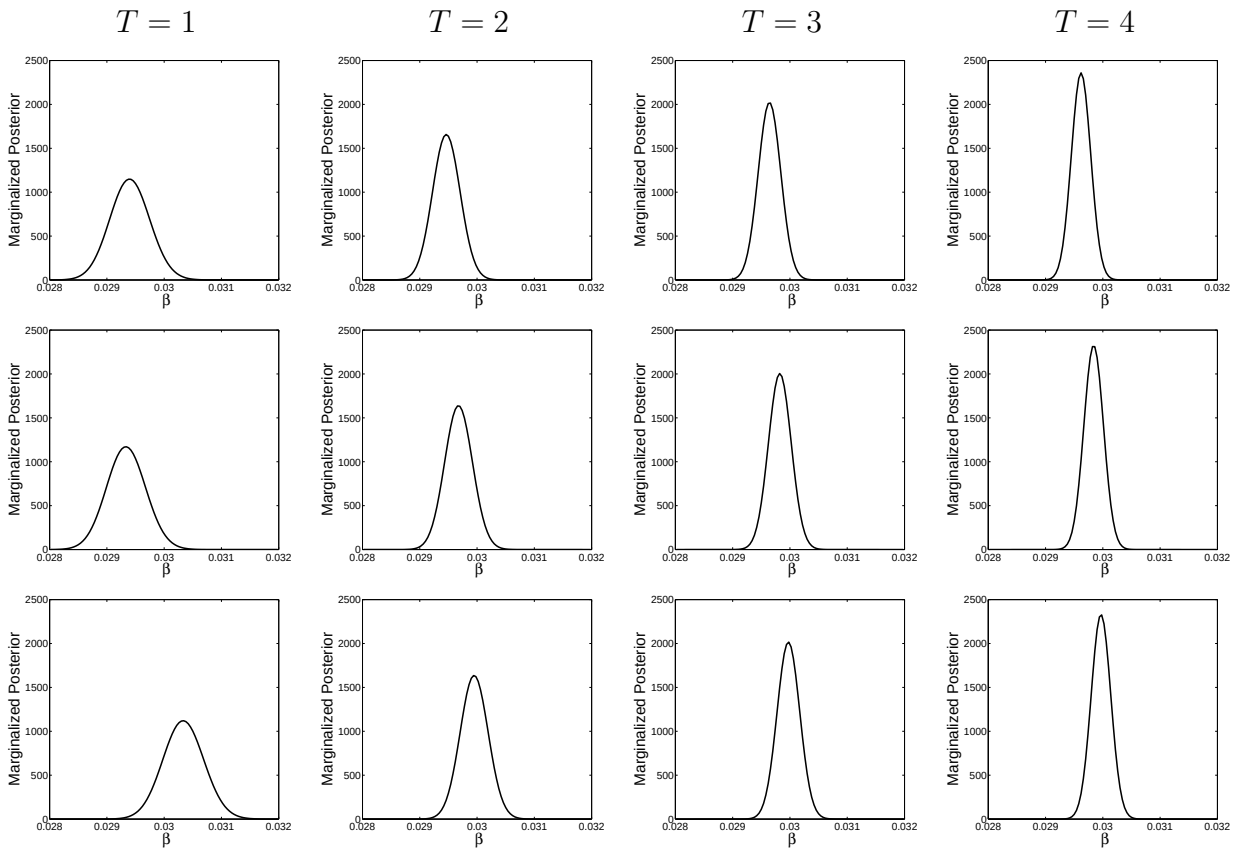

Figure 2.6: Marginalized posterior distributions of β calculated from two-dimensional observed images. Cases of $T = 1, 2, 3, 4$ are listed from the left to the right. Distributions in the same row are obtained by the same original image. The true values of hyperparameters are set to $(\alpha_0, \beta_0) = (1, 0.03)$. The number of pixels of image data is set to $N = 128^2$.

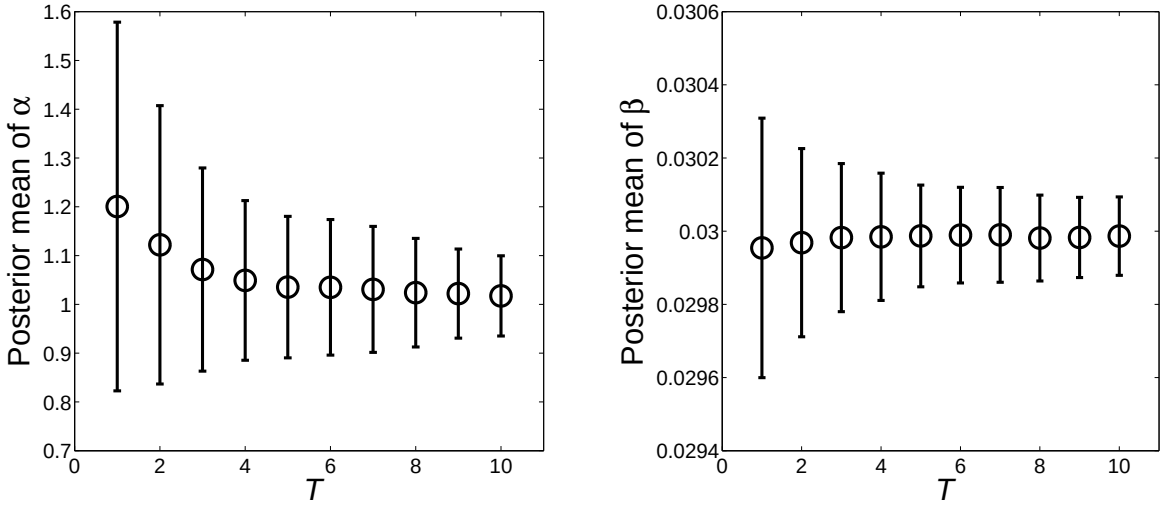

Figure 2.7: Posterior mean values of hyperparameters calculated from two-dimensional observed images in the case of $T = 1$ to 10. Averaged values over 100 trials are shown and error-bars represent standard deviations. The left and the right panels are about α and β, respectively. The true values of hyperparameters are set to $(\alpha_0, \beta_0) = (1, 0.03)$. The number of pixels of image data is set to $N = 128^2$.

Bayesian inference based on posterior mean values performs well for hyperparameter estimation in our MRF model. Simultaneously, we can assure that we are able to enhance the confidence of measurements by obtaining more data.

Evaluation of the confidence of measurements by using methods of point estimation such as posterior mean needs a lot of data obtained on the same conditions as shown in Fig. 2.7. However, such an abundant data are not necessarily available in the scene of natural science. Once we acquire a posterior distribution, we are able to focus on its breadth, which can be evaluated quantitatively by entropy. The entropy of probability distribution functions is defined by such as

$$H_\alpha = \langle -\ln p(\alpha|\{\boldsymbol{y}^t\})\rangle_{\alpha|\{\boldsymbol{y}^t\}}, \tag{2.34}$$

$$H_\beta = \langle -\ln p(\beta|\{\boldsymbol{y}^t\})\rangle_{\beta|\{\boldsymbol{y}^t\}}. \tag{2.35}$$

Figure 2.8 shows the entropy values of hyperparameters. We see that the entropy values decrease as the confidence of measurements is raised by increasing the number of measurements T. The entropy is highly correlated with the standard deviation of posterior mean values and can be used as a criterion to evaluate the confidence of measurements.

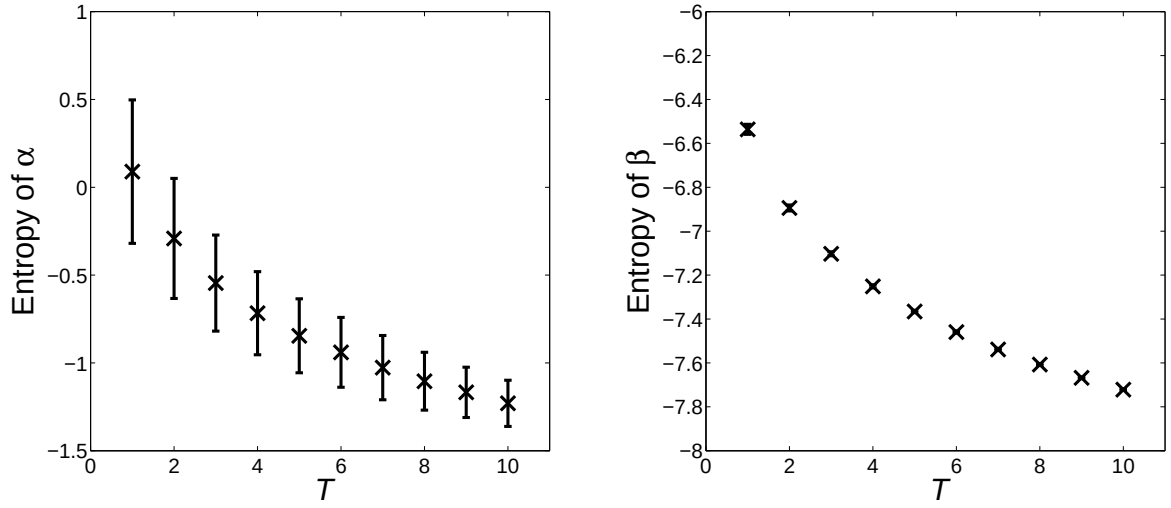

Figure 2.8: Entropy values of hyperparameters calculated from two-dimensional observed images in the case of $T = 1$ to 10. Averaged values over 100 trials are shown and error-bars represent standard deviations. The size of some error-bars are comparable to that of markers. The left and the right panels are about α and β, respectively. The true values of hyperparameters are set to $(\alpha_0, \beta_0) = (1, 0.03)$. The number of pixels of image data is set to $N = 128^2$.

2.5 Variational Bayesian method

Variational Bayesian inference is a well-known approach for calculating intractable posterior distributions of a number of random variables approximately [3]. A variational Bayesian method employs a tractable trial function and is conducted by minimizing the distance between the trial function and the posterior distribution. As a trial function of our posterior distributions $p(\alpha, \beta, \boldsymbol{x}|\{\boldsymbol{y}^t\})$, we use the following factorized distribution,

$$q(\alpha, \beta, \boldsymbol{x}) = q(\alpha)q(\beta)q(\boldsymbol{x}). \tag{2.36}$$

The distance is often measured by the Kullback-Leibler divergence defined by

$$\mathrm{KL}(q||p) = \int q(\alpha, \beta, \boldsymbol{x}) \ln \frac{q(\alpha, \beta, \boldsymbol{x})}{p(\alpha, \beta, \boldsymbol{x}|\boldsymbol{y})} \mathrm{d}\alpha \mathrm{d}\beta \mathrm{d}\boldsymbol{x}. \tag{2.37}$$

Our purpose is to minimize the divergence on the condition that the probability of the whole parameter space is equal to one and we conduct it using the method of Lagrange multipliers. The objective functional is

$$\begin{aligned} \mathcal{L}(q) &= \mathrm{KL}(q||p) + \lambda_\alpha \left[\int q(\alpha) \mathrm{d}\alpha - 1 \right] \\ &\quad + \lambda_\beta \left[\int q(\beta) \mathrm{d}\beta - 1 \right] + \lambda_{\boldsymbol{x}} \left[\int q(\boldsymbol{x}) \mathrm{d}\boldsymbol{x} - 1 \right], \end{aligned} \tag{2.38}$$

and its minimizer is given by

$$\ln q(\alpha) = \langle \ln p(\alpha, \beta, \boldsymbol{x} | \{\boldsymbol{y}^t\} \rangle_{\beta, \boldsymbol{x}} + \text{constant}, \tag{2.39a}$$

$$\ln q(\beta) = \langle \ln p(\alpha, \beta, \boldsymbol{x} | \{\boldsymbol{y}^t\} \rangle_{\alpha, \boldsymbol{x}} + \text{constant}, \tag{2.39b}$$

$$\ln q(\boldsymbol{x}) = \langle \ln p(\alpha, \beta, \boldsymbol{x} | \{\boldsymbol{y}^t\} \rangle_{\alpha, \beta} + \text{constant}, \tag{2.39c}$$

Eqs. (2.39) are not closed because the right-hand sides include the operation of expectation value with regard to the probability distribution functions shown in the left-hand sides. We need to solve them in a self-consistent way.

Returning to our MRF model, we substitute Eqs. (2.7) and (2.9) into Eqs. (2.39) to obtain the solution

$$q(\alpha) \propto \alpha^{\frac{N}{2}} \exp\left[-\left(\frac{N}{2} + 1 \right) \frac{\alpha}{\theta_\alpha} \right] \tag{2.40a}$$

$$q(\beta) \propto \beta^{\frac{TN}{2}} \exp\left[-\left(\frac{TN}{2} + 1 \right) \frac{\beta}{\theta_\beta} \right] \tag{2.40b}$$

$$q(\boldsymbol{x}) \propto \prod_{k=1}^{N} \exp\left[-\frac{\theta_\alpha l_k + \theta_\beta T}{2} \left| \tilde{x}_k - \frac{\theta_\beta T}{\theta_\alpha l_k + \theta_\beta T} \tilde{y}_k^{\text{ave}} \right|^2 \right] \tag{2.40c}$$

where the values of θ_α and θ_β are determined by repeating the following iteration

$$\theta_\alpha = \left(\frac{N}{2} + 1 \right) \left[\sum_k \frac{l_k}{2} \left\{ \frac{1}{\theta_\alpha l_k + \theta_\beta T} + \left(\frac{\theta_\beta T}{\theta_\alpha l_k + \theta_\beta T} \right)^2 |\tilde{y}_k^{\text{ave}}|^2 \right\} \right]^{-1}, \tag{2.41a}$$

$$\theta_\beta = \left(\frac{TN}{2} + 1 \right) \left[\sum_k \frac{T}{2} \left\{ \frac{1}{\theta_\alpha l_k + \theta_\beta T} + \left(\frac{\theta_\alpha l_k}{\theta_\alpha l_k + \theta_\beta T} \right)^2 |\tilde{y}_k^{\text{ave}}|^2 + \frac{1}{T} \sum_t |\tilde{y}_k^t - \tilde{y}_k^{\text{ave}}|^2 \right\} \right]^{-1}. \tag{2.41b}$$

We will now evaluate the performance of our variational Bayesian method by numerical simulations. We deal with the same situation with the previous section. We examine the case of two-dimensional images which satisfy periodic boundary conditions. The number of pixels of image data is set to $N = 128^2$. The true values of hyperparameters are set to $(\alpha_0, \beta_0) = (1, 0.03)$.

Figure 2.9 shows joint posterior distributions obtained by our variational Bayesian method, $q(\alpha, \beta) = q(\alpha)q(\beta)$, and Figs. 2.10 and 2.11 show its marginalized posterior distributions of α and those of β, respectively. In these figures, we see that the location of posterior distribution is closer to the true value as the number of measurements, T, increases. Figure 2.12 shows the posterior mean values of hyperparameters. We see that both of the posterior mean of α and β get closer to the true value and its standard deviation decreases as the number of image data used in estimation increases. Comparing

Figs. 2.7 and 2.12, we find that our variational Bayesian method performs almost as well as the exact calculation in terms of point estimation. Besides, we can make sure that the confidence of measurements is enhanced by increasing the amount of data.

From the viewpoint of distribution estimation, the results of our variational Bayesian method change from those of the exact calculation. Figure 2.9 shows joint posterior distributions of α and β calculated using our variational Bayesian method. As is clearly seen in Figs. 2.4 and 2.9, the shape of posterior distributions obtained by the two methods are different from each other. Our variational Bayesian method gives us narrower posterior distributions. This fact means that one can overestimate the confidence of measurements.

The degree of overestimation seems to depend on the kind of hyperparameters to be estimated. We show marginalized posterior distributions of α and β in Figs. 2.10 and 2.11. We compare them with Figs. 2.5 and 2.6 to find the confidence of α is overestimated too much while that of β is not so. Figure 2.13 plots the entropy of the posterior distribution against the amount of image data. In the case of β, the entropy decreases as the number of observations increases. In the case of α, on the other hand, the decrease in the entropy seems to stop where T is approximately equal to five. According to this result it is considered that for the purpose of estimating the value of α it is sufficient to observe five sheets of image data. However, this behavior of the entropy does not capture the decreasing tendency of the standard deviation of posterior mean values which happens as the amount of data increases. We claim that it is risky to use posterior distributions obtained by variational Bayesian methods for evaluating the confidence of hyperparameter estimation.

What is the difference between α and β? Let us recall the meaning of the hyperparameters. The hyperparmaeter α represent the degree of smoothness of original images and can be interpreted as the diffusion coefficient. The other hyperparameter β is the precision of measurements. As indicated in Fig. 2.3, α is farther away from the observed data in the data-generating mechanism than β is. We infer that deep parameters such as α are hard to estimate and are sensitive to approximation employed for estimation even if it is little.

2.6 Discussion

The chapter has explained the MRF approach to image data analysis. We pointed out that MRF is equivalent to the diffusion equation and the hyperparameters represent significant physical quantities as well as tuning parameters. Then, we proposed a Bayesian method of hyperparameter estimation and evaluate its performance by numerical simulations. We made the most of the framework of Bayesian method to evaluate data reliability by calculating the entropy of posterior distributions. In addition, we demonstrated that the variational Bayesian method fails to calculate posterior distributions.

It is trivial that the reliability of data increases as the amount of data increases without deteriorating their quality. From the viewpoint of design of experiments, it is significant to

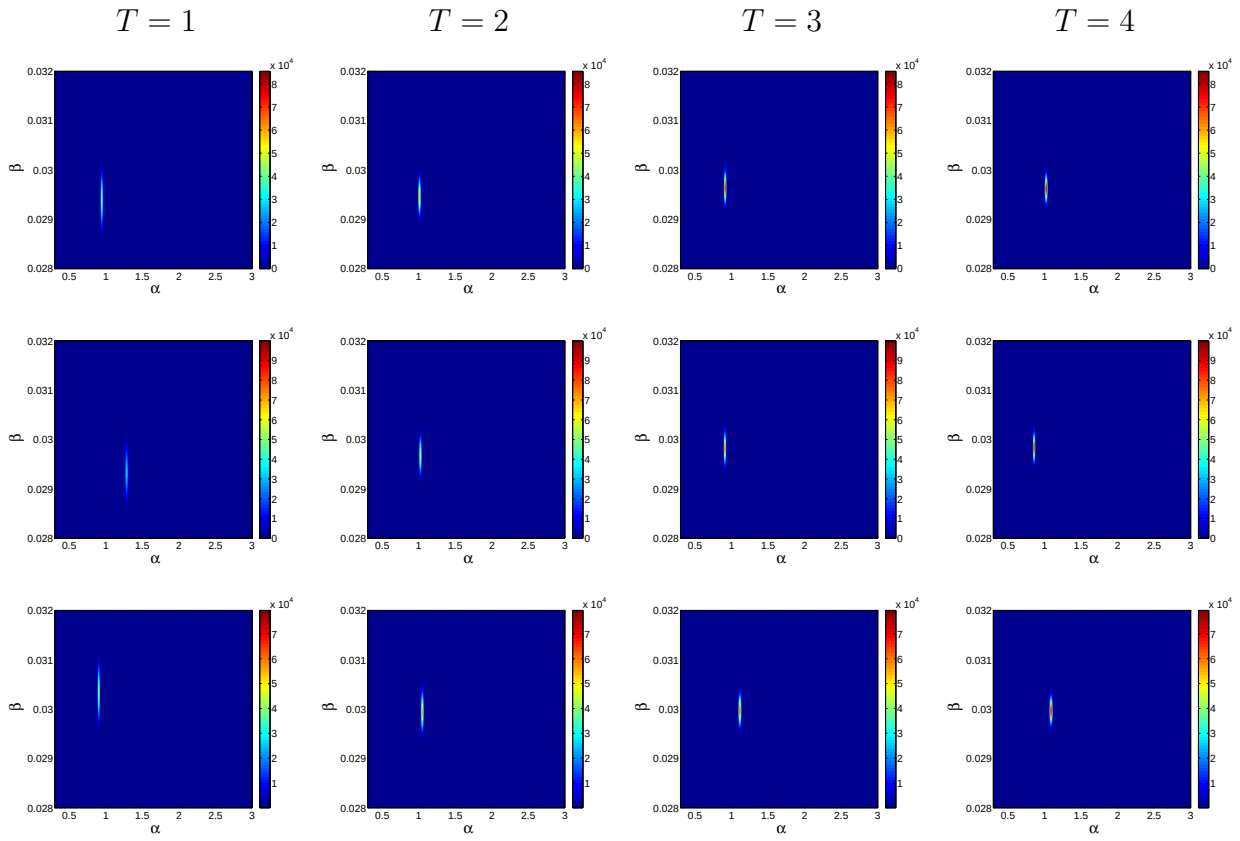

Figure 2.9: Joint posterior distributions of (α, β) approximately calculated from two-dimensional observed images using our variational Bayesian method. The horizontal and vertical axes represent α and β, respectively. Cases of $T = 1, 2, 3, 4$ are listed from the left to the right. Distributions in the same row are obtained by the same original image. The true values of hyperparameters are set to $(\alpha_0, \beta_0) = (1, 0.03)$. The number of pixels of image data is set to $N = 128^2$.

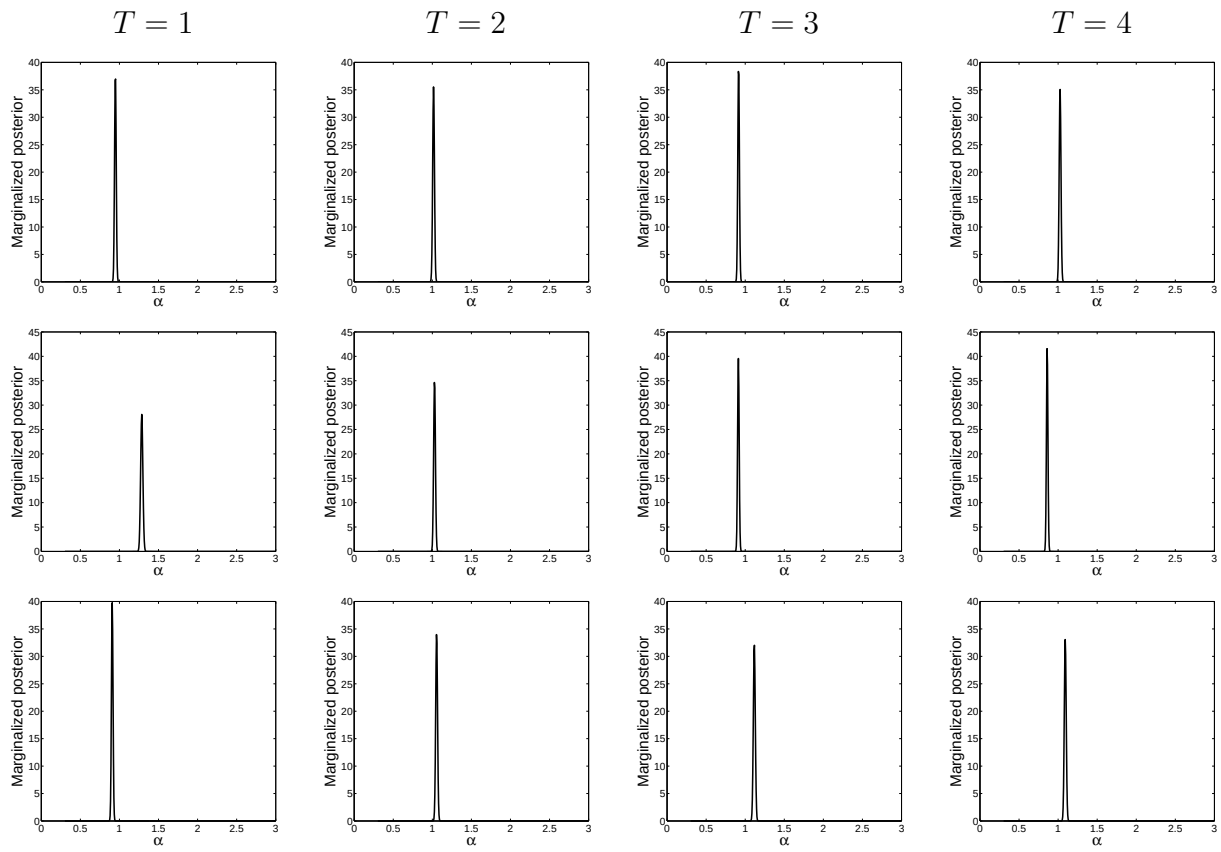

Figure 2.10: Marginalized posterior distributions of α calculated from two-dimensional observed images using our variational Bayesian method. Cases of $T = 1, 2, 3, 4$ are listed from the left to the right. Distributions in the same row are obtained by the same original image. The true values of hyperparameters are set to $(\alpha_0, \beta_0) = (1, 0.03)$. The number of pixels of image data is set to $N = 128^2$.

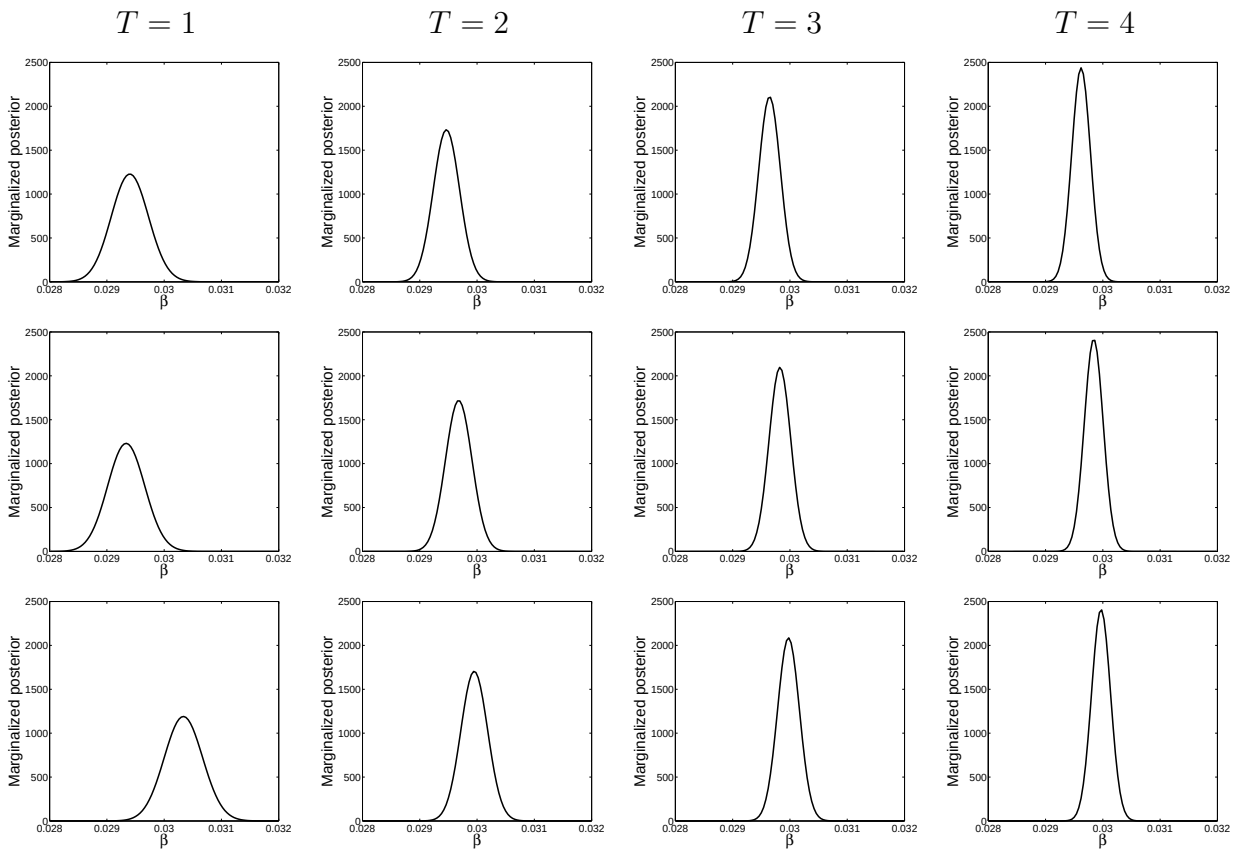

Figure 2.11: Marginalized posterior distributions of β calculated from two-dimensional observed images using our variational Bayesian method. Cases of $T = 1, 2, 3, 4$ are listed from the left to the right. Distributions in the same row are obtained by the same original image. The true values of hyperparameters are set to $(\alpha_0, \beta_0) = (1, 0.03)$. The number of pixels of image data is set to $N = 128^2$.

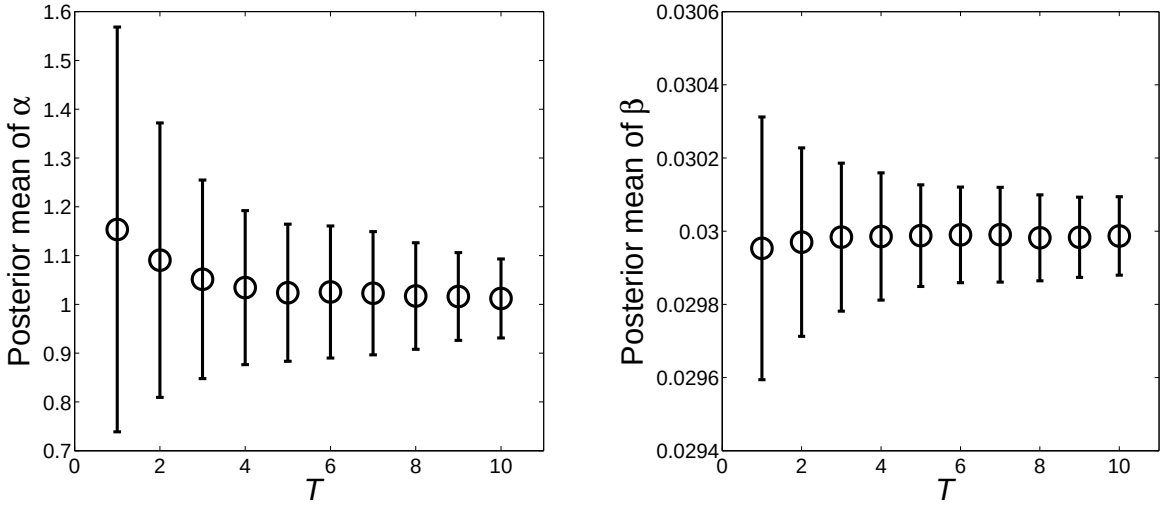

Figure 2.12: Posterior mean values of hyperparameters calculated from two-dimensional observed images in the case of $T = 1$ to 10, obtained by our variational Bayesian method. Averaged values over 100 trials are shown and error-bars represent standard deviations. The left and the right panels are about α and β, respectively. The true values of hyperparameters are set to $(\alpha_0, \beta_0) = (1, 0.03)$. The number of pixels of image data is set to $N = 128^2$.

optimize experimental conditions in practical situations where a trade-off problem exists. For example, when the measurement time is limited, it is difficult to determine whether to increase the number of image data at the expense of measurement precision. We will probably take not only the Gaussian noise but also the Poissonian noise into consideration if very little time is available [105, 94].

Much more still remains to be discussed. For example, let us consider the discipline of geoscience where the concept of MRF has recently begun to be utilized [64, 87, 65, 66, 60]. It is also important how many measurement points to prepare for obtaining image data of broad regions. In the case of geological boring survey, one cannot cover the whole earth with innumerable holes. Our framework of evaluating the reliability is expected to be helpful for planning where to investigate the next. Actually, there are few methods for observing the inside of the earth directly like boring survey. In this case, one has no choice but to use an indirect method such as seismic tomography. However, wave velocity maps obtained by seismic tomography are nonlinearly connected to the distribution of geofluids. Our framework should be extended so as to apply such a nonlinear measurement.

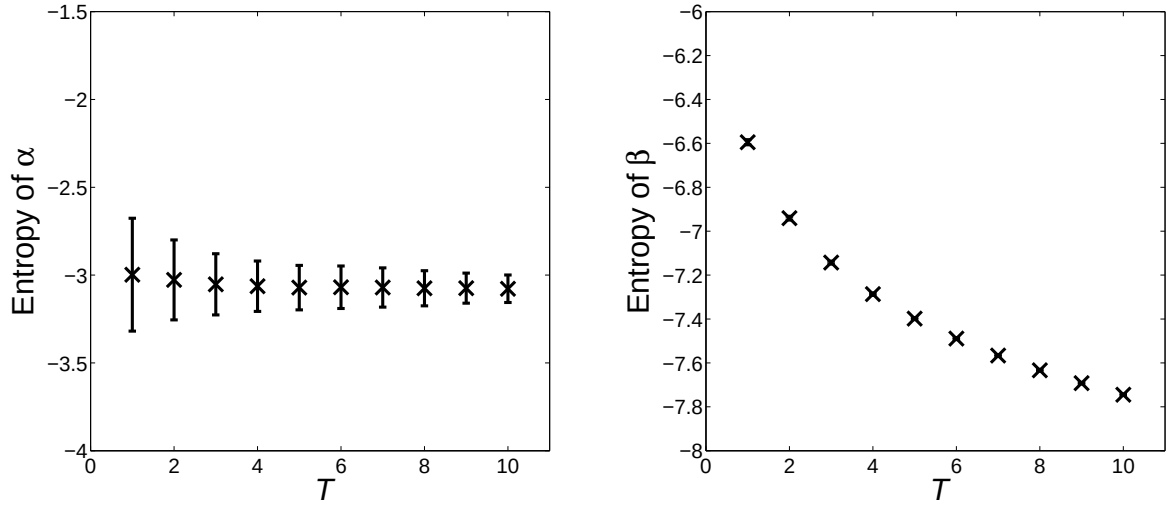

Figure 2.13: Entropy values of hyperparameters calculated from two-dimensional observed images in the case of $T = 1$ to 10, obtained by our variational Bayesian method. Averaged values over 100 trials are shown and error-bars represent standard deviations. The size of some error-bars are comparable to that of markers. The left and the right panels are about α and β, respectively. The true values of hyperparameters are set to $(\alpha_0, \beta_0) = (1, 0.03)$. The number of pixels of image data is set to $N = 128^2$.

Chapter 3

Theory of Compressed Sensing

3.1 Introduction

Most of the measurement systems in natural science are regarded as linear. We will formulate a linear model of the measurement process. Let a column vector $\boldsymbol{x}^0 = (x_1^0, x_2^0, \ldots, x_N^0)^{\mathrm{T}}$ be an original signal and the number of its non-zero elements is denoted by K. When the measurement system is described by a set of N-dimensional row vectors, $\{\bar{\boldsymbol{a}}_1, \ldots, \bar{\boldsymbol{a}}_M\}$, each of the data y_μ is obtained by

$$y_\mu = \bar{\boldsymbol{a}}_\mu \boldsymbol{x}^0 \ (\mu \in \{1, 2, \ldots, M\}) \tag{3.1}$$

and the whole data $\boldsymbol{y} = (y_1, \ldots, y_M)^{\mathrm{T}}$ are expressed as

$$\boldsymbol{y} = \boldsymbol{A}\boldsymbol{x}^0, \tag{3.2}$$

where the matrix $\boldsymbol{A}$ is called a measurement matrix defined by $\boldsymbol{A} = (\bar{\boldsymbol{a}}_1^{\mathrm{T}}, \ldots, \bar{\boldsymbol{a}}_M^{\mathrm{T}})^{\mathrm{T}}$. A measurement matrix $\boldsymbol{A}$ is also called a basis matrix because a data vector is expressed as a linear combination of its column vectors $\{\boldsymbol{a}_1, \ldots, \boldsymbol{a}_N\}$ in the following way,

$$\boldsymbol{y} = \sum_i x_i^0 \boldsymbol{a}_i. \tag{3.3}$$

The purpose is to estimate the original signal $\boldsymbol{x}^0$ from the data $\boldsymbol{y}$ based on the relation Eq. (3.2). If the number of measurements is larger than the dimension of the original signal, that is $M > N$, we are able to acquire the original signal from the data $\boldsymbol{y}$ as a solution of the least-squares method,

$$\hat{\boldsymbol{x}}_{\mathrm{ls}} = \underset{\boldsymbol{x}}{\mathrm{argmin}} \left\{ ||\boldsymbol{y} - \boldsymbol{A}\boldsymbol{x}||_2^2 \right\}. \tag{3.4}$$

The solution is obtained by

$$\hat{\boldsymbol{x}}_{\mathrm{ls}} = \boldsymbol{A}^{+}\boldsymbol{y}, \tag{3.5}$$

where $\boldsymbol{A}^+$ is the Moore-Penrose pseudoinverse matrix of $\boldsymbol{A}$. Compressed sensing is aimed at the situation where the number of measurements is smaller than the dimension of the original signal, $M < N$, but in this case the linear system Eq. (3.2) is underdetermined and the least-squares method cannot lead to a unique solution.

Sparseness is the secret to compressed sensing. A signal is called to be sparse if its non-zero elements are few. In the case of a sparse signal, the l_0-minimization method is considered to perform well even if $M < N$. Let us introduce the l_0-norm, denoted by $||\cdot||_0$, which is the number of non-zero elements of a vector and $||\boldsymbol{x}^0||$ is set to be equal to K. The l_0-minimization method is carried out by solving the following constrained optimization problem,

$$\min_{\boldsymbol{x}}\{||\boldsymbol{x}||_0\}, \text{ subject to } \boldsymbol{y} = \boldsymbol{A}\boldsymbol{x}, \tag{3.6}$$

where $||\cdot||_0$ is called the l_0-norm of a vector, defined as the number of non-zero elements of a vector (though l_0-norm is not a proper norm in a mathematical sense). However, it is difficult to carry out the l_0-norm minimization method because the problem, Eq. (3.6), is NP-hard and it causes a combinatorial explosion [85]. It is necessary to design an efficient algorithm for practical use of compressed sensing.

3.2 Approximate algorithms

A lot of approximate algorithms have been designed in order to address the problem of combinatorial explosion and some of them have recently become popular because it was demonstrated that their solutions are equal to or close to the original signal under appropriate conditions. Most of the algorithms are divided into two approaches: relaxation and greedy approaches [38, 92]. We will explain these approaches and their representative algorithms.

3.2.1 Relaxation approach

The relaxation approach is based on replacing the original optimization problem by a tractable one. For example convex relaxations are often employed to approximate a non-convex optimization problem by a convex one close to the original one. Convex relaxations are useful because there are well-known algorithms to carry out convex optimization efficiently.

In compressed sensing, the cost function of the l_0-minimization method, Eq. (3.6), is non-convex and intractable. We are interested in the performance of convex-relaxation approaches where the l_0-norm is replaced by the l_1-norm or by the l_2-norm as follows:

$$\min_{\boldsymbol{x}}\{||\boldsymbol{x}||_1\} \text{ subject to } \boldsymbol{y} = \boldsymbol{A}\boldsymbol{x}, \tag{3.7}$$

$$\min_{\boldsymbol{x}}\{||\boldsymbol{x}||_2\} \text{ subject to } \boldsymbol{y} = \boldsymbol{A}\boldsymbol{x}, \tag{3.8}$$

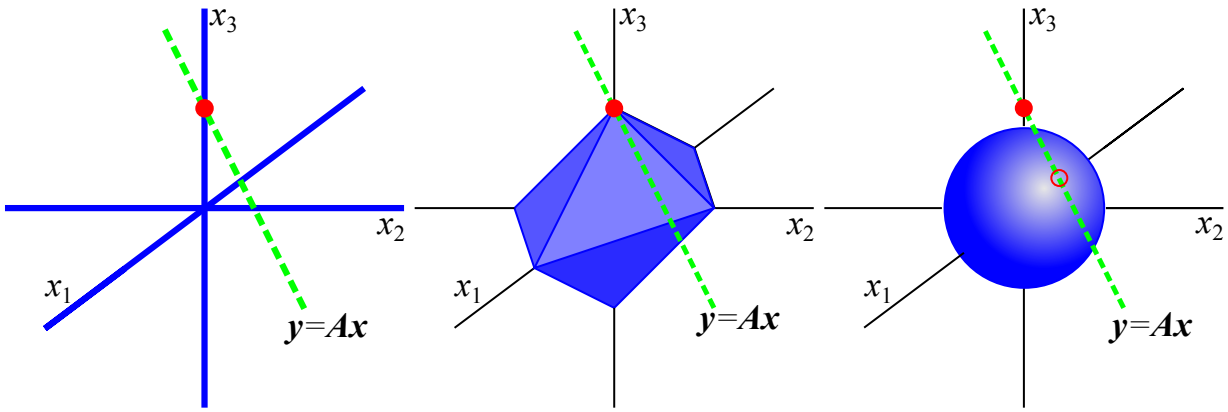

Figure 3.1: Geometric representation of the l_p-norm minimization methods in compressed sensing with $(N, M, K) = (3, 2, 1)$ and the $p = 0, 1, 2$ cases are shown from the left. The red filled circle located at $(x_1, x_2, x_3) = (0, 0, 1)$ is the original signal. The green dashed line is a subspace determined by measurements and of course crosses the original signal point in the noiseless case. The blue subspace is the smallest l_p-ball that touches the measurement line and the point of contact, the red open circle, represents the estimator of the l_p-norm minimization methods. In the $p = 0, 1$ cases, the estimator point is equal to the original point, but in the $p = 2$ case, the estimator point is different from the original point.

where $||\cdot||_1$ is called the l_1-norm of a vector defined as

$$||\boldsymbol{x}||_1 = \sum_{i=1}^{N} |x_i|. \tag{3.9}$$

The l_1-norm minimization method, Eq. (3.7), is also known as basis pursuit [18, 19]. Basis pursuit can be reformulated as a linear program [10]. Linear programming is a well-studied class of optimization problems with efficient solution techniques and needs only polynomial time to execute [62]. The l_2-norm minimization method, Eq. (3.8), can be executed by operating the pseudoinverse $\boldsymbol{A}^+$ to the data vector $\boldsymbol{y}$.

Let us compare the sparseness of solutions obtained by the l_p-norm minimization methods. Figure 3.1 illustrates the methods geometrically. The red filled circle represents a sparse original signal $(s_1, s_2, s_3) = (0, 0, 1)$. If a data vector $\boldsymbol{y} = (y_1, y_2)^{\mathrm{T}}$ is obtained by two trials of measurement $\{\bar{\boldsymbol{a}}_1, \bar{\boldsymbol{a}}_2\}$, the solution space can be restricted to a subspace represented by a green dashed line. Then, the l_p-norm minimization methods are employed to select a unique solution from the measurement line. Carrying out the l_p-norm minimization is equivalent to finding the smallest l_p-ball tangent to the measurement line and the point of contact, denoted by a red open circle, means the estimator. Here, a l_p-ball C_p with a radius R is defined by

$$C_p = \{\boldsymbol{x} \mid ||\boldsymbol{x}||_p \leq R\}. \tag{3.10}$$

Algorithm 1 Orthogonal matching pursuit

Input: a data vector $\boldsymbol{y} \in \mathbb{R}^M$, a measurement matrix $\boldsymbol{A} = (\boldsymbol{a}_1, \ldots, \boldsymbol{a}_N) \in \mathbb{R}^{M \times N}$, Sparseness K.
Initialize: $\boldsymbol{x} \leftarrow \boldsymbol{0}$, $S \leftarrow \emptyset$, $U \leftarrow \{1, 2, \ldots, N\}$
Iterate:
for $n = 1$ to K **do**
  $\boldsymbol{r} \leftarrow \boldsymbol{y} - \boldsymbol{A}\boldsymbol{x}$
  for $i = 1$ to N **do**
    $h_i \leftarrow \boldsymbol{a}_i^{\mathrm{T}} \boldsymbol{r}$
  end for
  $j \leftarrow \arg\max_{i \in U} \{|h_i|\}$
  $S \leftarrow S \cup \{j\}$, $U \leftarrow U \backslash \{j\}$
  $\boldsymbol{x} \leftarrow \arg\min_{\boldsymbol{z} \in \mathbb{R}^N} \{||\boldsymbol{y} - \boldsymbol{A}\boldsymbol{z}||_2\}$ subj. to $\mathrm{supp}(\boldsymbol{z}) \subset S$
end for
Output: a sparse vector $\boldsymbol{x}$

($\emptyset$ represents the empty set, and $\mathrm{supp}(\cdot)$ represents the support of a function)

The estimator of the l_0- and l_1-norm minimization tends to be as sparse as the original signal because l_0- and l_1-balls are pointed outwardly. On the other hand, the l_2-norm minimization method gives not a sparse solution because of the spherical form of l_2-balls. Therefore, basis pursuit is considered to perform well in terms of accuracy and tractability.

3.2.2 Greedy approach

It is beneficial to regard the task of compressed sensing as the problem of subset selection in order to discuss the greedy approach. Compressed sensing is formulated as a problem of selecting a small subset of basis vectors to explain the data sufficiently. The execution of the greedy approach starts with the empty set and is followed by adding basis vectors one by one to make an appropriate subset. The greedy approach employs a criterion to measure the fitness of basis vectors to the target data and at each iteration the best basis vectors among remaining ones is selected according to the criterion. The greedy approach approximates the exhaustive-search method by making the locally optimal choice repeatedly and cuts down its computational cost by not rethinking about basis vectors which were selected once. Of course, greedy algorithms are not necessarily guaranteed to be exact as well as basis pursuit, but are easy to understand and implement intuitively.

A representative algorithm of the greedy approach is orthogonal matching pursuit shown in Algorithm 1. At each iteration of orthogonal matching pursuit, one chooses the best column vector that is closest to the residual vector $\boldsymbol{r}$, where the criterion is the inner product between the residual vector and each of the basis vectors.

3.3 Performance analysis of basis pursuit

As explained so far, basis pursuit is considered to have two advantage points, tractability and accuracy. It is no exaggeration to say that the success of basis pursuit has triggered the recent spread of compressed sensing. It was demonstrated at last that basis pursuit gives the same solution with the l_0-minimization method on appropriate conditions [29, 33, 28]. In this section, we review three approaches to mathematically demonstrate that basis pursuit is useful for compressed sensing, in a brief way: restricted isometry property, geometry, and statistical mechanics.

3.3.1 Restricted isometry property

A series of proof is based on the restricted isometry property also known as the uniform uncertainty principle [14, 15, 13], introduced by Candès and Tao [16, 17]. The s-th restricted isometry constant δ_s of a measurement matrix $\boldsymbol{A}$ is defined by the smallest $\delta \geq 0$ such that

$$(1-\delta)||\boldsymbol{x}||_2^2 \leq ||\boldsymbol{A}\boldsymbol{x}||_2^2 \leq (1+\delta)||\boldsymbol{x}||_2^2 \tag{3.11}$$

for all vectors $\boldsymbol{x}$ such that $||\boldsymbol{x}||_0 \leq s$. A matrix $\boldsymbol{A}$ is said to have the restricted isometry property if δ_s is small for large s. In an extreme case of an orthogonal matrix $\boldsymbol{A}$, the restricted isometry constant is equal to 0 for all s because for all $\boldsymbol{x}$

$$||\boldsymbol{A}\boldsymbol{x}||_2^2 = (\boldsymbol{A}\boldsymbol{x})^{\mathrm{T}}(\boldsymbol{A}\boldsymbol{x}) = \boldsymbol{x}^{\mathrm{T}}\boldsymbol{A}^{\mathrm{T}}\boldsymbol{A}\boldsymbol{x} = \boldsymbol{x}^{\mathrm{T}}\boldsymbol{I}\boldsymbol{x} = \boldsymbol{x}^{\mathrm{T}}\boldsymbol{x} = ||\boldsymbol{x}||_2^2, \tag{3.12}$$

where $\boldsymbol{I}$ is the identity matrix. Then, the restricted isometry property can be regarded as a measure of orthogonality.

We here return to the problem of whether basis pursuit is exact or not. A sufficient condition involving the restricted isometry property was obtained by Candès [13]. More precisely, if the measurement matrix satisfies $\delta_{2s} < \sqrt{2}-1$, the solution to basis pursuit (3.7) is equal to that of the l_0-norm minimization method (3.6) for all sparse signals $\boldsymbol{x}$ such that $||\boldsymbol{x}||_0 \leq s$. This sufficient condition has been improved several times [37, 36, 11, 12, 80]. On the other hand, it was reported that there are matrices with restricted isometry constant δ_{2s} arbitrarily close to $1/\sqrt{2}$ for which some sparse vectors are not recovered by using basis pursuit [24]. This report implies that there is a boundary between success and failure of basis pursuit.

Incidentally, the restricted isometry property is also used to evaluate the performance of greedy approaches in a similar way [38]. It was observed that orthogonal matching pursuit can fail to recover the original signal under a standard restricted isometry condition [27]. On the other hand, it was demonstrated that orthogonal matching pursuit succeeds in compressed sensing when a number of iterations that is proportional to the number of nonzero components [110].

3.3.2 Geometry

A boundary between success and failure of basis pursuit was found by Donoho and Tanner, using methods of geometry [31, 26] as illustrated in Fig. 3.1. They handled the case where the length of signals N is infinitely large with the ratio of M to N fixed and a random matrix is employed as a measurement matrix $\boldsymbol{A}$ [104]. In their proof, a measurement matrix $\boldsymbol{A}$ is associated to a polytope $P \subset \mathbb{R}^M$ such that

$$P = \{\boldsymbol{y} \in \mathbb{R}^M \mid \exists \boldsymbol{x} \in C,\ \boldsymbol{y} = \boldsymbol{A}\boldsymbol{x}\}, \tag{3.13}$$

where C is the N-dimensional l_1-ball, namely

$$C = \{\boldsymbol{x} \in \mathbb{R}^N \mid ||\boldsymbol{x}||_1 \leq 1\}. \tag{3.14}$$

The key concept they introduced is the central neighborliness of centrosymmetric polytopes such as the above P. A centrosymmetric polytope is called central K-neighborly if every subset of K vertices not including an antipodal pair forms a face [42]. Then, they proved that if and only if the polytope P has $2N$ vertices and is central K-neighborly, the basis pursuit method recovers the original signal such that $||\boldsymbol{s}||_0 < K$. Based on this geometric interpretation, they finally derived an explicit form of the boundary separating two regions of success and failure regarding basis pursuit.

Surprisingly, exactly the same form of the boundary was obtained using methods of statistical mechanics although this approach is not mathematically rigorous [59, 40]. Because statistical mechanics has a lot of affinity with Bayesian inference, it is widely applicable to performance analysis of various settings of compressed sensing. Besides, it is useful to design efficient algorithms such as approximate message passing [30]. In the following subsection, we will explain the performance analysis of compressed sensing using methods from statistical mechanics.

3.3.3 Statistical mechanics

Let us formulate the problem of compressed sensing in the language of statistical mechanics or probability theory according to Kabashima *et al.* [59]. We assume that an original signal is sampled from the following probability distribution function

$$p(\boldsymbol{x}^0) = \prod_{i=1}^{N} \left\{ (1-\rho)\delta(x_i^0) + \rho \frac{1}{\sqrt{2\pi}} \exp\left[-\frac{(x_i^0)^2}{2} \right] \right\} \tag{3.15}$$

where the parameter ρ controls the sparseness of the signal. The measurement matrix is drawn from

$$p(\boldsymbol{A}) = \prod_{\mu=1}^{M} \prod_{i=1}^{N} \sqrt{\frac{N}{2\pi}} \exp\left[-\frac{N}{2} (A_{\mu i})^2 \right] \tag{3.16}$$

Considering the noiseless case, the measurement process is expressed as

$$p(\boldsymbol{y}|\boldsymbol{A},\boldsymbol{x}^0)=\delta(\boldsymbol{y}-\boldsymbol{A}\boldsymbol{x}^0)=\prod_{\mu=1}^{M}\delta\left[y_\mu-\sum_{i=1}^{N}A_{\mu i}x_i^0\right]. \tag{3.17}$$

The purpose is to obtain an estimator of $\boldsymbol{x}^0$ given a data vector $\boldsymbol{y}$.

The l_1-norm minimization method is related to the following canonical distribution,

$$p(\boldsymbol{x}|\boldsymbol{y})=\frac{1}{Z(\beta)}\exp\left[-\beta||\boldsymbol{x}||_1\right]\delta\left(\boldsymbol{y}-\boldsymbol{A}\boldsymbol{x}\right), \tag{3.18}$$

where Z is a partition function defined by

$$Z(\beta)=\int \mathrm{d}\boldsymbol{x}\exp\left[-\beta||\boldsymbol{x}||_1\right]\delta\left(\boldsymbol{y}-\boldsymbol{A}\boldsymbol{x}\right). \tag{3.19}$$

The solution of the l_1-norm minimization method corresponds to the ground state sampled from Eq. (3.18) in the limit of $\beta\to+\infty$. From the viewpoint of Bayesian inference, the canonical distribution is regarded as a posterior distribution derived from a prior distribution,

$$p(\boldsymbol{x})\propto\exp\left[-\beta||\boldsymbol{x}||_1\right], \tag{3.20}$$

and a likelihood function,

$$p(\boldsymbol{y}|\boldsymbol{x})=\delta(\boldsymbol{y}-\boldsymbol{A}\boldsymbol{x}). \tag{3.21}$$

Mean squared error is used to evaluate the performance of the l_1-norm minimization method. The typical error value is given by

$$\epsilon=\lim_{\beta\to+\infty}\left[\left\langle\frac{1}{N}||\boldsymbol{x}-\boldsymbol{x}^0||_2^2\right\rangle_{\boldsymbol{x}|\boldsymbol{y}}\right]_{\boldsymbol{y},\boldsymbol{A},\boldsymbol{x}^0}, \tag{3.22}$$

where $\langle\cdot\rangle_{\boldsymbol{x}|\boldsymbol{y}}$ is the thermal average with regard to Eq. (3.18) and $[\cdot]_{\boldsymbol{y},\boldsymbol{A},\boldsymbol{x}^0}$ is the configurational average with regard to Eqs. (3.15) to (3.17). Employing a modified partition function,

$$Z(\beta,\beta_\epsilon)=\int \mathrm{d}\boldsymbol{x}\exp\left[-\beta||\boldsymbol{x}||_1-\beta_\epsilon||\boldsymbol{x}-\boldsymbol{x}^0||_2^2\right]\delta\left(\boldsymbol{y}-\boldsymbol{A}\boldsymbol{x}\right), \tag{3.23}$$

the error value is expressed as

$$\epsilon=\lim_{\beta\to+\infty}\lim_{\beta_\epsilon\to+0}-\frac{\partial}{\partial\beta_\epsilon}\left[\frac{1}{N}\ln Z(\beta,\beta_\epsilon)\right]_{\boldsymbol{y},\boldsymbol{A},\boldsymbol{x}^0}. \tag{3.24}$$

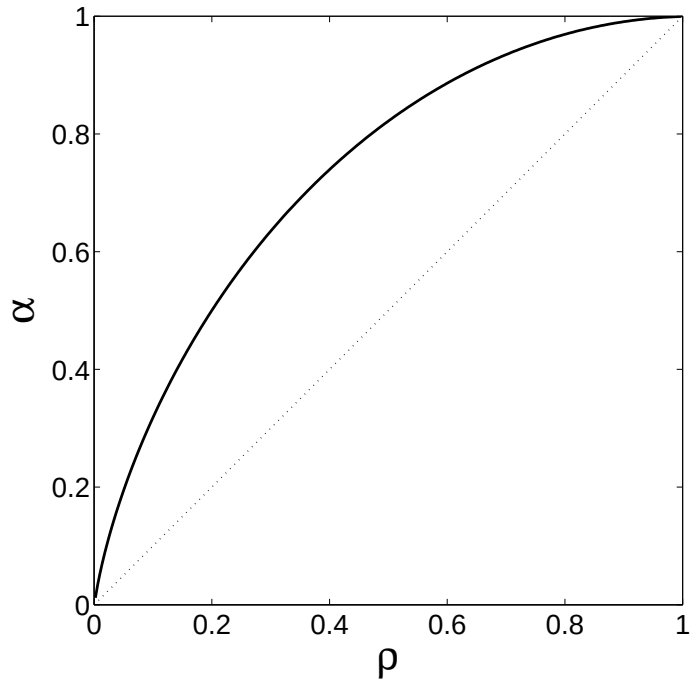

Figure 3.2: The solid line is the boundary between success and failure of the l_1-norm minimization method obtained by a method of statistical mechanics [59]. Above the line is the region of success. The horizontal axis $\rho = K/N$ represents the degree of sparseness of the original signal. The vertical axis $\alpha = M/N$ represents the number of measurements compared to the number of variables

We analyze the performance of the l_1-norm minimization method in the thermodynamic limit, namely $N \to +\infty$ with $\rho = K/N$ and $\alpha = M/N$ fixed, using methods derived from statistical mechanics. The mean squared error can be assessed by the saddle-point method and the replica method to obtain

$$\epsilon = Q - 2m + \rho. \tag{3.25}$$

Here, the equations of state that determine the value of Q and m are given by

$$\hat{m} = \frac{\alpha}{2}\frac{1}{\chi}, \tag{3.26a}$$

$$\hat{Q} = \frac{\alpha}{2}\frac{1}{\chi}, \tag{3.26b}$$

$$\hat{\chi} = \frac{\alpha}{2}\frac{Q-2m+\rho}{\chi^2}, \tag{3.26c}$$

$$m = \rho\frac{\hat{m}}{\hat{Q}}\mathrm{erfc}(\theta_m), \tag{3.26d}$$

$$Q = (1-\rho)\frac{1}{8\theta^2\hat{Q}^2}\left\{(1+2\theta^2)\mathrm{erfc}(\theta) - \theta\frac{2}{\sqrt{\pi}}\mathrm{e}^{-\theta^2}\right\}, \tag{3.26e}$$

$$+\rho\frac{1}{8\theta_m^2\hat{Q}^2}\left\{(1+2\theta_m^2)\mathrm{erfc}(\theta_m) - \theta_m\frac{2}{\sqrt{\pi}}\mathrm{e}^{-\theta_m^2}\right\}, \tag{3.26f}$$

$$\chi = (1-\rho)\frac{1}{2\hat{Q}}\mathrm{erfc}(\theta) + \rho\frac{1}{2\hat{Q}}\mathrm{erfc}(\theta_m), \tag{3.26g}$$

where $\theta = \frac{1}{\sqrt{4\hat{\chi}}}$, $\theta_m = \frac{1}{\sqrt{4\hat{\chi}+8\hat{m}^2}}$, and $\mathrm{erfc}(\cdot)$ is the complementary error function defined by

$$\mathrm{erfc}(x) = \frac{2}{\sqrt{\pi}}\int_x^{+\infty}\mathrm{d}t\mathrm{e}^{-t^2}. \tag{3.27}$$

Figure 3.2 shows the boundary between success and failure of the l_1-norm minimization method. In the top-left region above the boundary, the mean squared error is zero and the l_1-norm minimization method succeeds in compressed sensing. Of course, the l_1-norm minimization method fails in the case where the number of measurements is small though the original signal is not so sparse. However, judging from the breadth of the success region, basis pursuit is considered to be practical.

Chapter 4

Application of Compressed Sensing to Experimental Physics

4.1 Scanning probe microscopy

In 1982, scanning probe microscopy (SPM) originated from the invention of scanning tunneling microscopy (STM) by Binnig and Rohrer [6, 5]. SPM is a group of experimental technology in which, as shown in Fig. 4.1, a characteristic probe is brought close to a material surface and the surface is scanned over a large region to acquire imaging data. The tip of the probe is so sharp that at its very end there is only one atom as shown in the enlarged view of Fig. 4.1. Thanks to the extreme sensitivity of tunneling current to height, the resolution of SPM is comparable to the size of atoms. The first significant achievement of SPM is the determination of Si(111)-(7×7) surface reconstruction structure, also known as a dimer-adatom-stacking fault (DAS) model. Without the SPM technology, the DAS model was controversial for more than 25 years and there was only indirect evidence in reciprocal space obtained by electron-diffraction experiments [96, 68, 103, 46, 71, 77]. Then, the real-space observation of the Si(111) surface with STM by the inventors was really astonishing to the society of surface science and simultaneously this achievement established that the SPM technology is effective and promising [7].

The SPM technology has a simple measurement principle of scanning material surfaces with a sharp probe. More interestingly, SPM can be applied to measuring various physical quantities of various material surfaces just by changing stuff for its probe. In atomic force microscopy (AFM), a cantilever is used for a probe to detect atomic force [8]. Because there is atomic force such as van der Waals force even between insulator materials, AFM is used to study insulator surfaces. Besides, it was reported that AFM can be used to distinguish between different chemical species of atoms on a material surface [98]. Spin-polarized scanning tunneling microscopy (SPSTM) was invented by Wiesendanger *et al.* [107, 106]. SPSTM employs a probe whose tip is covered with thin film of magnetic materials. Because tunneling conductance depends on the direction of

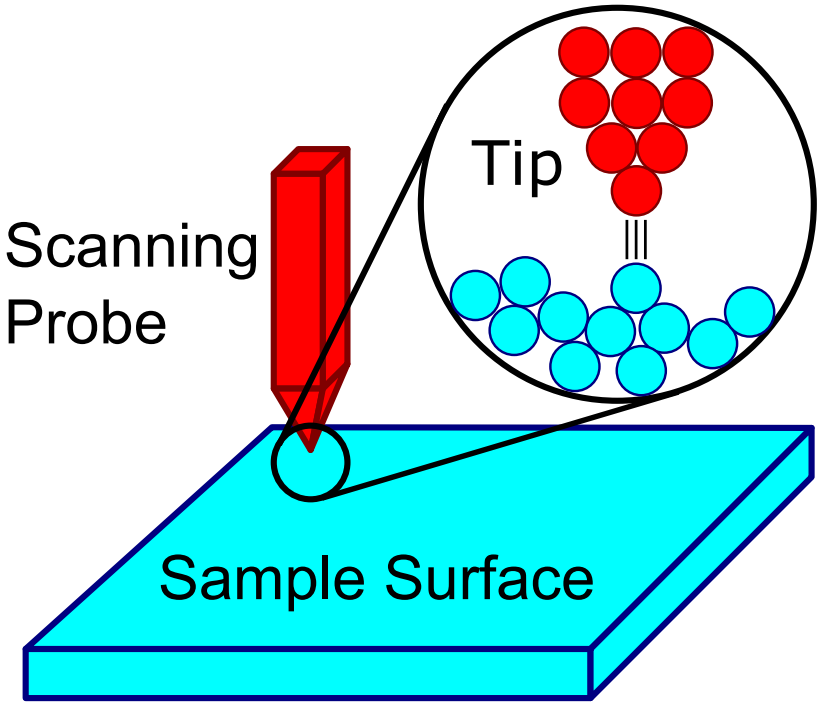

Figure 4.1: Measurement principle of scanning probe microscopy.

spin angular momentum in material surfaces, SPSTM enables us to reveal complicated magnetic nanostructure such as conical spin-spirals and skyrmions [49, 108].

We explain the mechanism of the STM measurement briefly. STM is based on the phenomenon of quantum tunneling, where particles such as electrons move through potential barriers which could not be passed in the range of classical mechanics. It means that, even if the conducting tip of STM is in no direct contact with the sample surface, a certain amount of electric current can flow between them. According to the theory of quantum mechanics, the amount of tunneling current is given by

$$I(\boldsymbol{r}, z, V) \propto \int_{-\infty}^{+\infty} \rho_{\mathrm{tip}}(E) f(E) \rho_{\mathrm{sample}}(\boldsymbol{r}, E + eV)(1 - f(E + eV)) T(\boldsymbol{r}, z, eV, E) \mathrm{d}E. \quad (4.1)$$

Here, $\boldsymbol{r}$ is the coordinates on the sample surface, z is the distance between the surface and the probe tip, V is the bias voltage, E is the energy, e is the elementary charge, ρ_{tip} is the density of states (the DOS) of the tip, ρ_{sample} is the local density of states (the LDOS) of the sample surface, f is the Fermi distribution function, and T is the tunneling transition probability. For low temperatures, we obtain

$$I(\boldsymbol{r}, z, V) \propto \int_{-eV}^{0} \rho_{\mathrm{tip}}(E) \rho_{\mathrm{sample}}(\boldsymbol{r}, E + eV) T(\boldsymbol{r}, z, eV, E) \mathrm{d}E. \quad (4.2)$$

When a simple material such as tungsten metal or a platinum-iridium alloy is used for the tip, ρ_{tip} is regarded as constant and the tunneling current is reduced to

$$I(\boldsymbol{r}, z, V) \propto \int_0^{eV} \rho_{\mathrm{sample}}(\boldsymbol{r}, E) T(\boldsymbol{r}, z, eV, E) \mathrm{d}E. \tag{4.3}$$

According to the Wentzel-Kramers-Brillouin (WKB) theory, the transition probability is given by

$$T(\boldsymbol{r}, z, eV, E) \propto \exp\left[-2\kappa(\boldsymbol{r}, eV, E) z\right], \tag{4.4}$$

where κ is expressed as

$$\kappa(\boldsymbol{r}, eV, E) = \frac{\sqrt{2m(\phi(\boldsymbol{r}) - E + eV/2)}}{\hbar}, \tag{4.5}$$

using the work function ϕ. The work function refers to the minimum energy needed to remove an electron from a material surface to a vacuum space and is considered to be dominant in κ. As a result, we obtain the following relation

$$I(\boldsymbol{r}, z, V) \propto \exp\left[-2\kappa(\boldsymbol{r}) z\right] \int_0^{eV} \rho_{\mathrm{sample}}(\boldsymbol{r}, E) \mathrm{d}E, \tag{4.6}$$

$$\kappa(\boldsymbol{r}) = \frac{\sqrt{2m\phi(\boldsymbol{r})}}{\hbar} \sim 1\text{Å}^{-1}. \tag{4.7}$$

In Eq. (4.6), we see that the amount of tunneling current gets one digit smaller as the distance between the tip and atoms on the surface increases by a length comparable to the size of atoms. Thanks to the high sensitivity, topography data of material surfaces at atom resolution are available by scanning them keeping the tunneling current and bias voltage constant.

In this work, we focus on scanning tunneling spectroscopy (STS), an application of STM. The STS technique enables us to distinguish electrons which have different energy values. STS makes use of the fact that the derivative of the tunneling current with respect to the bias voltage $\mathrm{d}I/\mathrm{d}V$, namely the tunneling conductance, is proportional to the LDOS,

$$\frac{\mathrm{d}I}{\mathrm{d}V} \propto \rho_{\mathrm{sample}}(\boldsymbol{r}, E = eV), \tag{4.8}$$

according to Eq. (4.6). Then, $\mathrm{d}I/\mathrm{d}V$ image data recorded at various bias voltage points give us a lot of information on energy dependence of LDOS maps of electrons.

4.2 Quasiparticle interference

When material surfaces are observed at atom resolution by STM, we see various kinds of patterns [47, 20]. A $\mathrm{d}I/\mathrm{d}V$ image of a surface of Au on mica is shown in Fig. 4.2

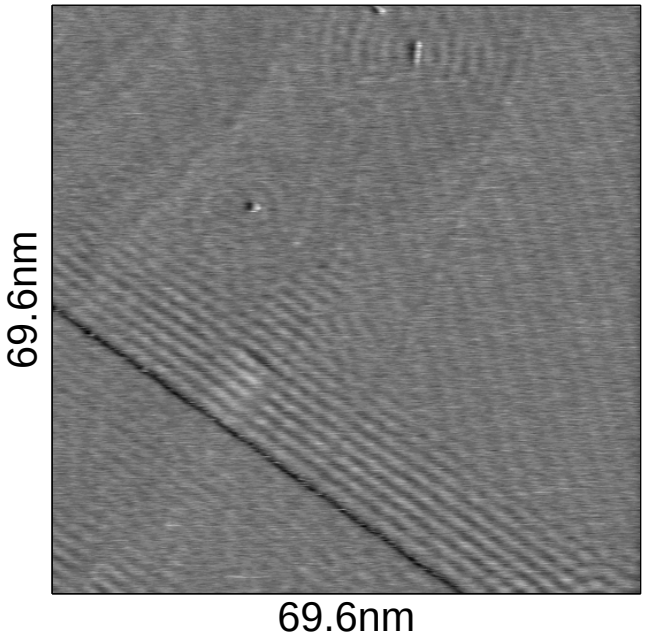

Figure 4.2: A dI/dV image of an Au-on-mica sample observed by STM (the area of the region, 69.6nm×69.6nm; the number of measurement points, 512×512; a bias voltage, -100mV).

and there is a LDOS pattern which reminds us of traditional Japanese gardens. Along the step in the bottom left is a parallel wave pattern and concentric circular patterns are formed with their centers on point defects. Standing-wave patterns on metal surfaces are caused by interference of free electrons scattered by defects and impurities and we call them patterns of electron standing wave.

Scientists not only from surface science but also from other fields of condensed matter physics pay attention to the recent results of STS measurements. The STM and STS technologies have been playing a great role in revealing the emergence mechanism of superconductivity [52, 75, 43, 44, 35] and topological insulators [95, 111, 2, 88, 90]. For example, when an iron-based superconductor material is observed by the STM measurement, a similar pattern to ones appearing on metal surfaces is seen [45]. This pattern is considered to be formed by Bogoliubov quasiparticles, which are broken pairs of Cooper pairs, and is also known as quasiparticle interference patterns. Quasiparticle interference patterns observed by STS are expected to be useful for evaluating the band dispersion of strongly correlated electron systems and the spin structure of topological insulators.

Quantum physics tells us that electrons exhibit the property of waves and their

behavior is described by wave functions. The squared absolute value of a wave function, $|\psi(\boldsymbol{r})|^2$, is interpreted as the probability density of an electron being at a location $\boldsymbol{r}$ in a two-dimensional surface. Then, wave functions ψ are linked to LDOS images in the following way,

$$\rho(\boldsymbol{r}) \propto |\psi(\boldsymbol{r})|^2. \tag{4.9}$$

In order to discuss the dispersion relation between energy and wavenumber, we are interested in the Fourier transform of wave functions, which is related to that of LDOS images as follows:

$$\tilde{\rho}(\boldsymbol{q}) \;=\; \int \mathrm{d}\boldsymbol{k}\tilde{\psi}(\boldsymbol{k})\tilde{\psi}^*(\boldsymbol{k}-\boldsymbol{q}), \tag{4.10}$$

derived from Eq. (4.9), where

$$\tilde{\rho}(\boldsymbol{q}) \;=\; \int \mathrm{d}\boldsymbol{r}\rho(\boldsymbol{r})\mathrm{e}^{2\pi\mathrm{i}\boldsymbol{q}\cdot\boldsymbol{r}}, \tag{4.11}$$

$$\tilde{\psi}(\boldsymbol{k}) \;=\; \int \mathrm{d}\boldsymbol{r}\psi(\boldsymbol{r})\mathrm{e}^{2\pi\mathrm{i}\boldsymbol{k}\cdot\boldsymbol{r}} \tag{4.12}$$

For the sake of simplicity, we have assumed the isotropy of scattering. This relation indicates that the Fourier transform of LDOS images recorded at a bias voltage is equivalent to a mapping of scattering vectors $\boldsymbol{q} = \boldsymbol{k} - \boldsymbol{k}'$ at an energy value.

Let us consider simple systems described by a free-electron model whose dispersion relation is parabolic as shown in Fig. 4.3(a). When the paraboloid is cut at the $E = eV$ plane according to the bias voltage, a contour of constant electron energy appears in $\boldsymbol{k}$ space as shown in Fig. 4.3(b). In the case of the free-electron model, contours of constant electron energy are circular and described by

$$\tilde{\psi}(\boldsymbol{k}) \propto \delta(|\boldsymbol{k}| - k_0), \tag{4.13}$$

and then a corresponding scattering-vector map is given by

$$\tilde{\rho}(\boldsymbol{q}) \propto \begin{cases} \frac{1}{\frac{|\boldsymbol{q}|}{2k_0}\sqrt{1-\left(\frac{|\boldsymbol{q}|}{2k_0}\right)^2}} & \text{if } 0 < |\boldsymbol{q}| < 2k_0 \\ 0 & \text{otherwise} \end{cases}. \tag{4.14}$$

We see that the scattering-vector map takes a infinitely large value at the origin and points on the origin-centered circle with a radius of $2k_0$ as shown in Fig. 4.3(c). The Fourier transforms of $\mathrm{d}I/\mathrm{d}V$ images obtained at various bias voltage points by STS correspond to scattering-vector maps such as Fig. 4.3(c) and are considered to be the key to dispersion relation.

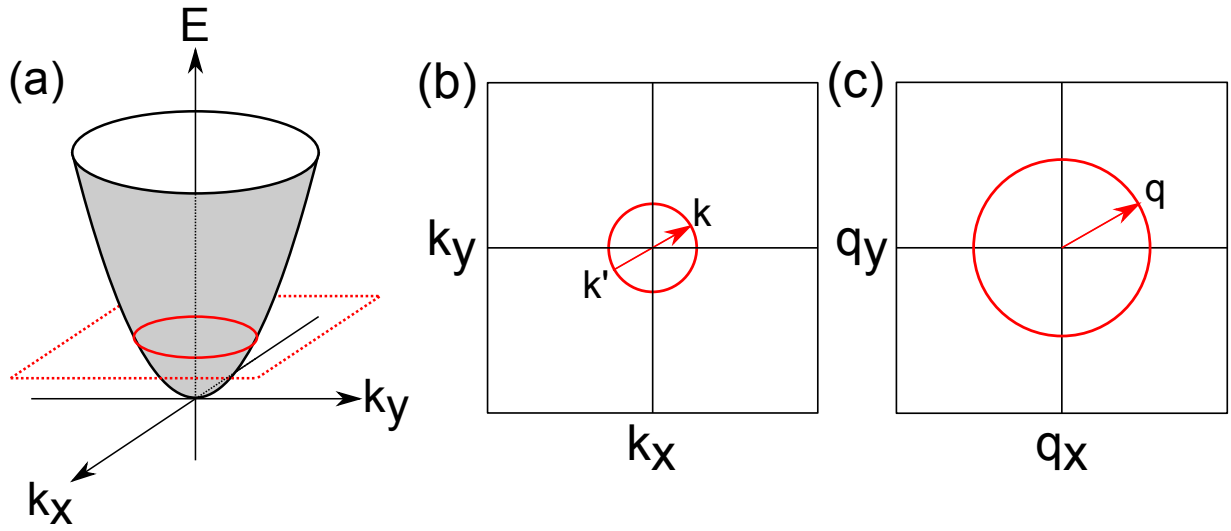

Figure 4.3: (a) Parabolic dispersion relation seen in free-electron systems, formulated by $E = \frac{\hbar^2 \boldsymbol{k}^2}{2m^*}$. (b) A contour of constant electron energy in $\boldsymbol{k}$ space, namely a cross section of (a) cut by the plane $E = eV$. (c) A map of scattering vectors which connect points on the contour of electron energy in (b).

4.3 Translation into compressed sensing

A drawback of the STM or STS measurement is that it takes a lot of experimental time to conduct spectroscopy measurement at many locations in a broad region of surfaces. We apply compressed sensing to retrieve scattering-vector maps from $\mathrm{d}I/\mathrm{d}V$ images partially obtained at a small number of measurement points. It is considered to be appropriate to assume the sparseness of scattering-vector maps, because a limited number of ways of electron scattering are allowed according to the dispersion relation.

Let us formulate the measurement system of STS according to Chap. 3. In STS measurements, a $\mathrm{d}I/\mathrm{d}V$ image at a bias voltage, $\{\rho(\boldsymbol{r}_\mu)\}$, is the data vector $\{y_\mu\}$, a scattering-vector map $\{\tilde{\rho}(\boldsymbol{q}_i)\}$ is the original signal $\{x_i^0\}$ to be estimated, and Fourier transform connects them as follows:

$$\boldsymbol{y} = \boldsymbol{A}\boldsymbol{x}^0 + \boldsymbol{n}, \tag{4.15}$$

where $\boldsymbol{A}$ represents the Fourier basis and $\boldsymbol{n}$ is a vector which represents measurement noise.

Previous studies of STM or STS often employ a fast Fourier transform (FFT) algorithm to estimate $\boldsymbol{x}^0$ from $\boldsymbol{y}$ by carrying out Fourier transform,

$$\hat{\boldsymbol{x}}_{\mathrm{FT}} = \boldsymbol{A}^* \boldsymbol{y}, \tag{4.16}$$

where $\boldsymbol{A}^*$ is the conjugate transpose matrix of $\boldsymbol{A}$. In the underdetermined case, the

Algorithm 2 Approximate message passing (AMP)

Input: data vector $\boldsymbol{y} \in \mathbb{R}^M$, basis matrix $\boldsymbol{A} = (\boldsymbol{a}_1, \ldots, \boldsymbol{a}_N) \in \mathbb{R}^{M \times N}$, regularization coefficient λ, tuning parameter δ.
$\boldsymbol{x} \leftarrow \boldsymbol{0}$, $\chi \leftarrow 0$, $\boldsymbol{r} \leftarrow \boldsymbol{y}$
while until convergence **do**
  $\hat{Q} \leftarrow \frac{1}{1+\chi}$
  $\boldsymbol{r} \leftarrow (1 - \hat{Q})\boldsymbol{r} + \hat{Q}(\boldsymbol{y} - \boldsymbol{A}\boldsymbol{x})$
  $\boldsymbol{h} \leftarrow \hat{Q}\boldsymbol{x} + \boldsymbol{A}^{\mathrm{T}}\boldsymbol{r}$
  for $i = 1$ to N **do**
    $x_i \leftarrow (1 - \delta)x_i + \delta \frac{1}{\hat{Q}} \mathrm{sign}(h_i)(|h_i| - \lambda)\Theta(|h_i| - \lambda)$
  end for
  $\chi \leftarrow (1 - \delta)\chi + \delta \frac{1}{\hat{Q}} \frac{1}{M} \sum_i \Theta(|h_i| - \lambda)$
end while
Output: the sparse vector $\boldsymbol{x}$

($\mathrm{sign}(\cdot)$ represents the sign function, and $\Theta(\cdot)$ represents Heaviside's step function)

estimator $\hat{\boldsymbol{x}}_{\mathrm{FT}}$ is equivalent to the solution of the l_2-norm minimization method,

$$\min_{\boldsymbol{x}} ||\boldsymbol{x}||_2 \text{ subject to } \boldsymbol{y} = \boldsymbol{A}\boldsymbol{x}. \tag{4.17}$$

As illustrated in Fig. 3.1, the l_2-norm minimization is not suitable for compressed sensing based on sparseness. In addition, the constraint $\boldsymbol{y} = \boldsymbol{A}\boldsymbol{x}$ is too strict in noisy situations.

We adopt the convex-relaxation approach for compressed sensing, and considering the noise we use least absolute shrinkage and selection operator (LASSO) instead of basis pursuit [102]. LASSO is carried out by solving the following optimization problem

$$\min_{\boldsymbol{x}} \left\{ ||\boldsymbol{y} - \boldsymbol{A}\boldsymbol{x}||_2^2 + \lambda ||\boldsymbol{x}||_1 \right\}, \tag{4.18}$$

where λ is a regularization parameter and is set to a positive value. LASSO is known to be equivalent to the following optimization problem,

$$\min_{\boldsymbol{x}} \{||\boldsymbol{x}||_1\} \text{ subject to } ||\boldsymbol{y} - \boldsymbol{A}\boldsymbol{x}||_2^2 < \epsilon. \tag{4.19}$$

Comparing with the basis pursuit method, Eq. (3.7), we see that LASSO adopts a weaker constraint regarding data fitting and is considered to be robust against measurement noise.

We carry out LASSO using the approximate-message-passing (AMP) algorithm [30]. The AMP algorithm is shown in Algorithm 2. LASSO is reformulated by a quadratic program. Quadratic programming is a well-studied class of optimization problems and can be solved with a computational cost of the order $O(N^3)$. On the other hand, AMP needs only a computational cost of the order $O(N^2)$ per update. AMP is a modification of belief propagation methods and was developed in the field of statistical mechanics.

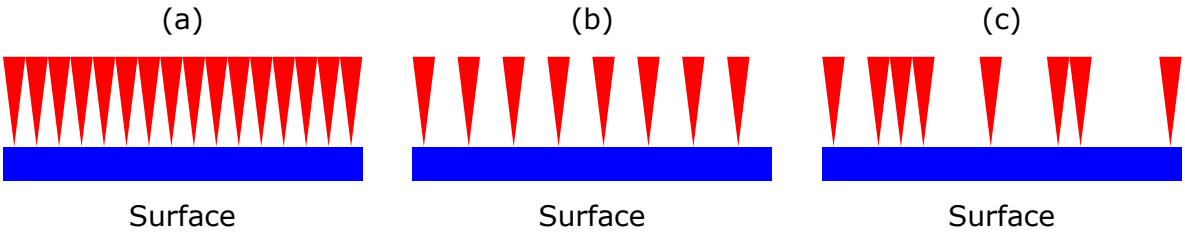

Figure 4.4: Methods of the STM measurement. (a) A conventional time-consuming method recording at a large number of measurement spots. (b) The regular downsampling method in which measurement spots are thinned out at regular intervals. (c) The random downsampling method in which measurement spots are thinned out randomly.

We use a cross-validation method to determine the parameter of LASSO λ [32, 63, 9]. Hopefully, the value of the parameter is determined so as to minimize the predictive error on new data, but one misses the original purpose of decreasing measurement time if one gets new data just for this purpose. Cross validation methods are used to estimate the predictive error without new data. We explain the procedure of cross-validation methods. First, one divides the data set $\{y_\mu\}$ into two sets, namely a training set $\{y_\mu^{\rm train}\}$ and a testing set $\{y_\mu^{\rm test}\}$. Second, one operates LASSO to the training set with various values of λ to obtain estimates of $\boldsymbol{x}$, denoted by $\hat{\boldsymbol{x}}^{\rm train}(\lambda)$, as follows:

$$\hat{\boldsymbol{x}}^{\rm train}(\lambda) = \arg\min_{\boldsymbol{x}} ||\boldsymbol{y}^{\rm train} - \boldsymbol{A}^{\rm train}\boldsymbol{x}||_2^2 + \lambda||\boldsymbol{x}||_1, \tag{4.20}$$

where $\boldsymbol{A}^{\rm train}$ is a submatrix of $\boldsymbol{A}$ composed of row vectors corresponding to the training set. Third, one calculates the cross validation error (CVE) defined by

$$\mathrm{CVE}(\lambda) = \sqrt{\frac{1}{M^{\rm test}}||\boldsymbol{y}^{\rm test} - \boldsymbol{A}^{\rm test}\hat{\boldsymbol{x}}^{\rm train}(\lambda)||_2^2}, \tag{4.21}$$

where $M^{\rm test}$ is the number of elements of the testing set and $\boldsymbol{A}^{\rm test}$ is a submatrix of $\boldsymbol{A}$ composed of row vectors corresponding to the testing set. Finally, we adopt a value of λ which gives the smallest CVE. The value of CVE depends on how to select the training data in the first step and one often uses the mean value of CVE over several trials on different training sets, such as leave-one-out cross validation and K-fold cross validation.

Putting compressed sensing into practice, we stress that there is room for improvement not only in methods of analysis but also in measurement methods. The point is how to decrease the number of measurement spots. The STM measurement is usually conducted at a large number of measurement spots to obtain a full set of image data as shown in Fig. 4.4(a). Naively, it could be fine to thin out spots at regular intervals as shown in Fig. 4.4(b), but we need not stick to do so because we do not use an FFT algorithm now. Instead, we propose to decrease the number of spots at random intervals as shown in Fig. 4.4(c). We compare the performance of the regular downsampling and the random downsampling when data obtained by the methods are analyzed using a method of compressed sensing, LASSO.

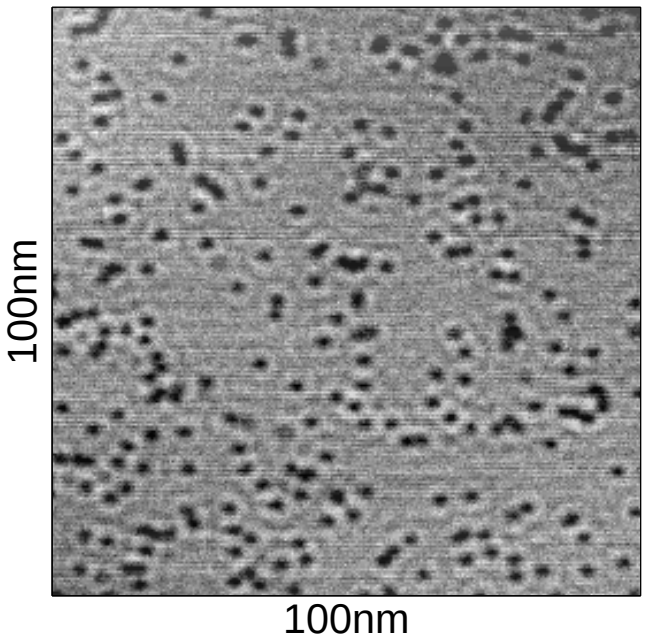

Figure 4.5: A topographic image of an Ag(111) surface obtained by STM (the area of the measurement region, 100nm×100nm; the number of measurement points, 256×256; a bias voltage, 50mV).

4.4 Demonstration

We investigate the effects of compressed sensing on the STM and STS measuments by numerical simulation using a set of raw data. Figure 4.5 shows an STM image to be used in all numerical simulations. The experiments to obtain the image data were performed using an ultrahigh vacuum STM setup (USM-1300, Unisoku, and SPM-1000, RHK) in which the tip and sample can be cooled down to approximately 2.6K at the Institute for Solid State Physics, the University of Tokyo. A single crystalline Ag(111) substrate was cleaned by repetitive Ar sputtering and annealing at approximately 800°C. The STM image of the Ag(111) surface was obtained at 4.2K. An electrochemically etched W tip, which was annealed at approximately 900°C in situ for removing the oxide layer from the tip apex, was used for the imaging. Topographic images are obtained based on the amount of tunneling current I, not $\mathrm{d}I/\mathrm{d}V$. According to Eq. (4.6), the quantity I is proportional to the integral of the sample LDOS over the energy interval between 0 and eV. Given at a low bias voltage $V = 50\mathrm{mV}$, however, topographic images can be regarded as LDOS maps at the Fermi energy because the range of integration in the right-hand-side of Eq. (4.6) is small. The full set of the image data is composed of 256×256 pixels and the

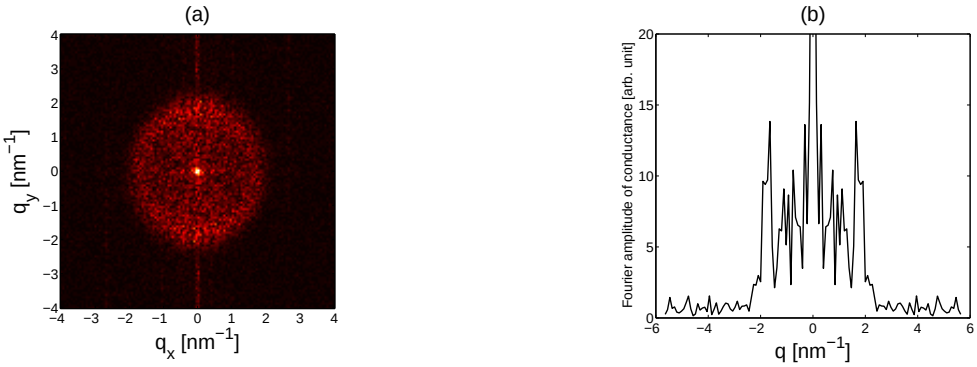

Figure 4.6: (a) A scattering-vector map obtained by the Fourier transform of the image data shown in Fig. 4.5. (b) Intensity of the scattering-vector map on the white diagonal line.

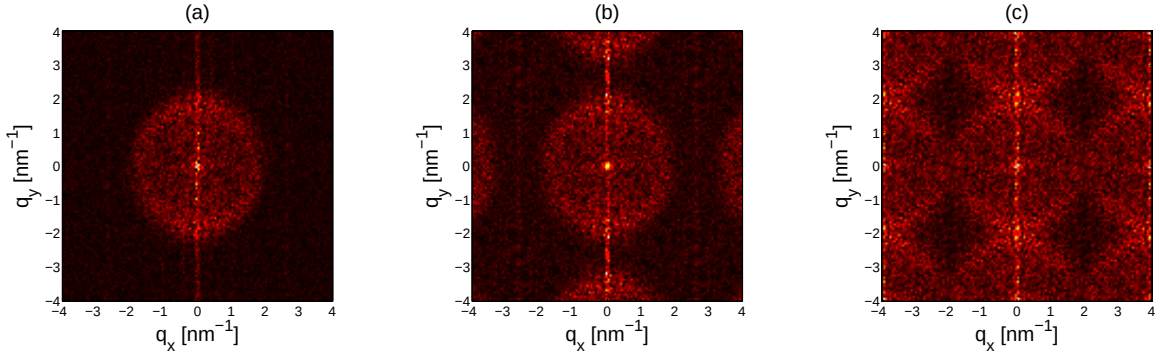

Figure 4.7: Scattering-vector maps estimated by Fourier transform without LASSO. The STM data of Fig. 4.5 is thinned out by the regular downsampling. The number of data points used for estimation is (a) 128×128, (b) 85×85, (c) 64×64.

data are normalized to be regarded as random variable whose mean and variance are zero and one, respectively. We try retrieving scattering-vector maps from only a part of the raw data to simulate downsampling methods numerically and evaluate the performance of compressed sensing.

When a conventional method of Fourier transform is applied to the image data of Fig. 4.5, we obtain a scattering-vector map shown in Fig. 4.6. The surface state of Ag(111) can be described by a free-electron-like model and a circular pattern is clearly seen in Fig. 4.6(a). This pattern is the 'answer' pattern in simulations below. Figure 4.6(b) plots the intensity of the scattering-vector map on the white diagonal line and we are sure that there is a peak where the circular pattern is located. When we operate Fourier transform to regularly downsampled data without a method of compressed sensing, the circular pattern in the scattering-vector map is hidden, as shown in Fig. 4.7. At a glance, unexpected arc-shaped patterns appear in the case of 85×85, Fig. 4.7(b), and they get closer to the answer circle as the degree of downsampling is higher. We attribute

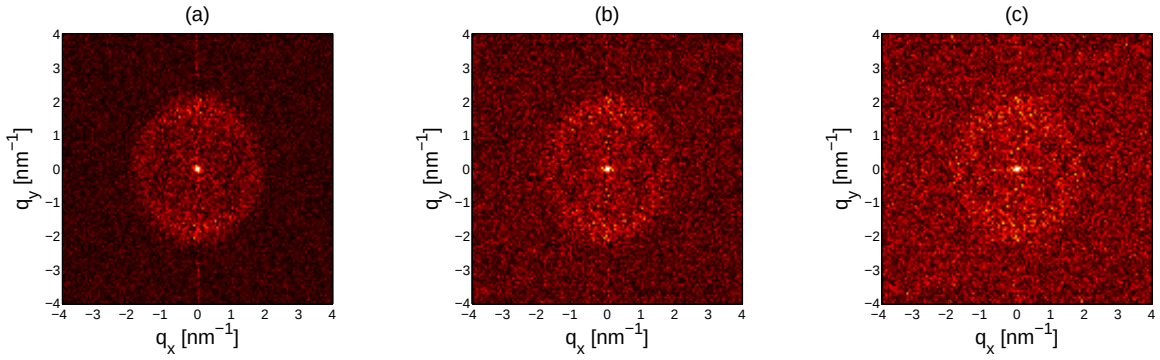

Figure 4.8: Scattering-vector maps estimated by Fourier transform without LASSO. The STM data of Fig. 4.5 is thinned out by the random downsampling. The number of data points used for estimation is (a) 16384, (b) 7225, (c) 4096.

it to the aliasing phenomenon also known as a cause of Moiré patterns, where different wavenumber components in an image data obtained with a constant spatial period become indistinguishable from one another.

In order to remove the aliasing effect, we operate the same Fourier transform to randomly downsampled data. Figure 4.8 shows the results. We see that there is no aliasing pattern and random sampling is effective in the treatment of aliasing. Comparing Fig. 4.8 with the answer pattern in Fig. 4.6, the circular pattern is hidden behind high-wavenumber components. In the case of the Ag(111) surface, the strength of high-wavenumber components is considered to be zero, but this method based on conventional Fourier transform captures measurement noise including high-wavenumber components and results in overfitting.

Now, we apply compressed sensing to randomly downsampled data. Instead of conventional Fourier transform, we use LASSO, which is carried out by the approximate message passing (AMP) algorithm shown in Algorithm 2. The regularization parameter of LASSO, λ, is determined by 10-fold cross validation. Figure 4.9 shows the results of LASSO. The circular pattern is clearly seen even in the case of 4096 data points in Fig. 4.9(c). The aliasing pattern does not appear around the circle. Figure 4.10 shows the intensity values on the diagonal line of scattering maps shown in Figs. 4.8 and 4.9. We see that peaks at the circular pattern are prominent in the results of LASSO while they are comparable with the magnitude of noise in the results of Fourier transform. We claim that LASSO enables us to decrease the number of measurement points without degrading the quality of scattering maps.

In order to make sure of the effect of random sampling, we operate LASSO to regularly downsampled data. Figure 4.11 shows the results. The pattern of aliasing still remains around the circular pattern in the same way with Fig. 4.7. We have checked that the aliasing pattern is not removed just by using LASSO. In order to realize compressed sensing, we should pay attention not only to analysis methods but also to measurement

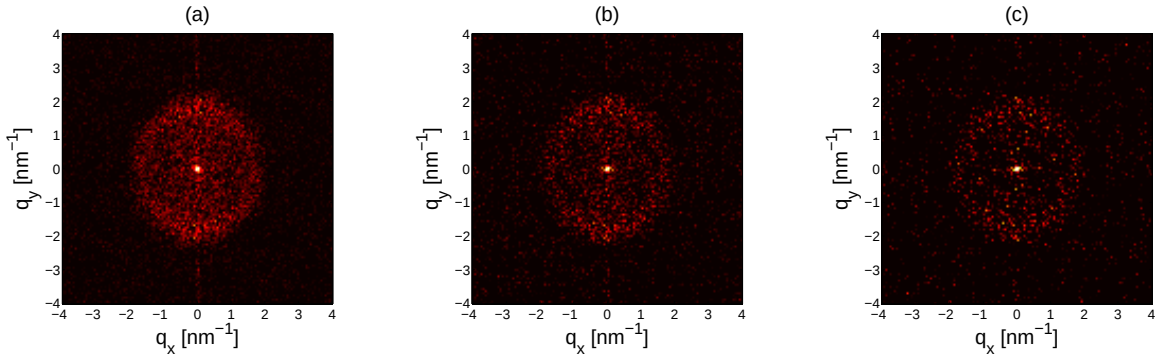

Figure 4.9: Scattering-vector maps estimated by LASSO. The STM data of Fig. 4.5 is thinned out by the random downsampling. The number of data points used for estimation is (a) 16384, (b) 7225, (c) 4096.

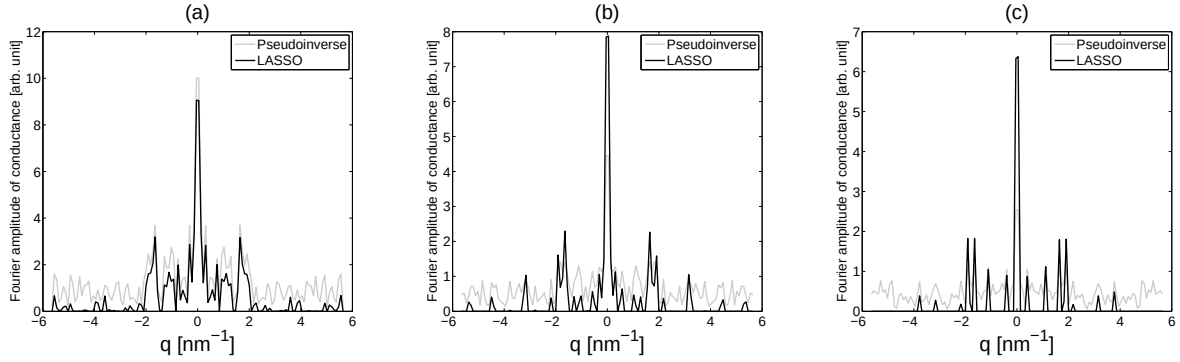

Figure 4.10: Intensity is plotted on the diagonal line of scattering maps shown in Figs. 4.8 and 4.9. The STM data of Fig. 4.5 is thinned out by the random downsampling. The number of data points used for estimation is (a) 16384, (b) 7225, (c) 4096.

methods, and in this case LASSO and the random sampling are necessary.

A further interest is what happens if the number of measurements is decreased more than the cases studied so far. Figure 4.12 shows the results of such cases where the number of data points is 2601 and 1764. In the case of 2601 pixels shown in Fig. 4.12(a), we can narrowly see the circular pattern, and in the case of 1764 pixels shown in Fig. 4.12(b), we cannot at all. However, we have to say that this judgment is biased. Without a prior knowledge that the dispersion relation of the Ag(111) surface is parabolic, it could be possible to think that the result in Fig. 4.12(b) is true.

We are forced to make a criterion to see if the given result is trustworthy or not, but it is really challenging. We focus on the behavior of CVE values, which are calculated to determine the value of λ in LASSO. Figure 4.13 shows CVE values calculated in 10-fold cross validation conducted to acquire scattering maps in Figs. 4.9 and 4.12. Noting that the data $\boldsymbol{y}$ has been normalized, the value of CVE is equal to one in the limit of $\lambda \to +\infty$ because the estimate $\hat{\boldsymbol{x}}$ obtained by LASSO with an infinitely large λ is equal to the

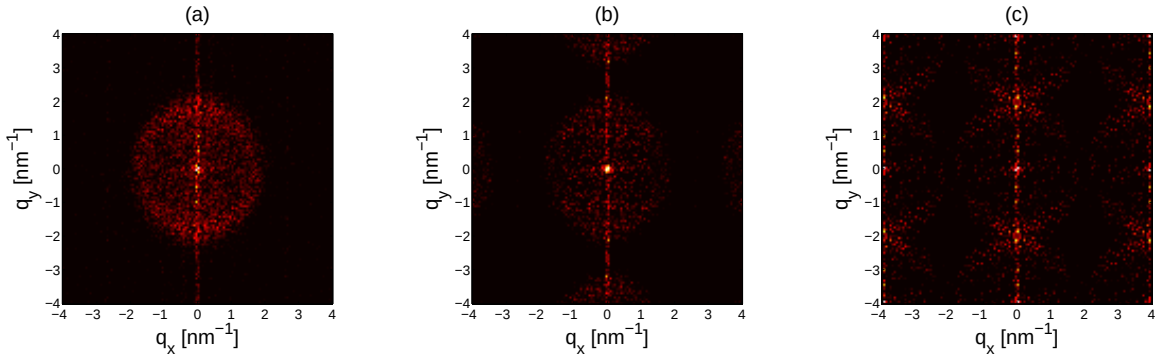

Figure 4.11: Scattering-vector maps estimated by LASSO. The STM data of Fig. 4.5 is thinned out by the regular downsampling. The number of data points used for estimation is (a) 128×128, (b) 85×85, (c) 64×64.

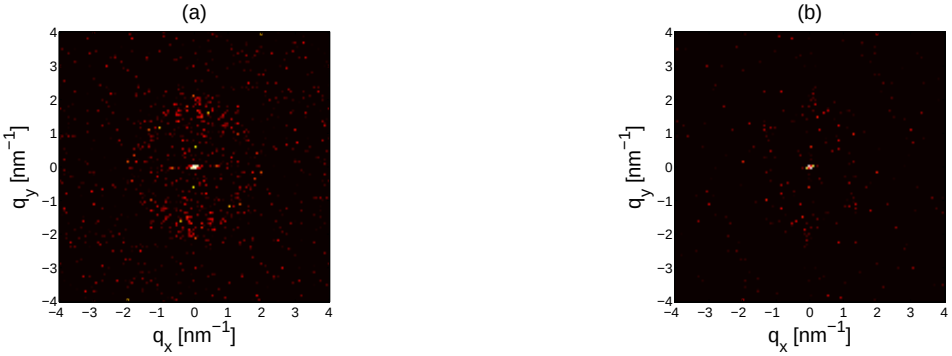

Figure 4.12: Scattering-vector maps estimated by LASSO. The STM data of Fig. 4.5 is thinned out by the random downsampling. The number of data points used for estimation is (a) 2601, (b) 1764.

zero vector. In the case of 16384 pixels, 7225 pixels, and 4096 pixels where the circular pattern is clearly seen in scattering maps, CVE values are much smaller than one. In contrast, in the case of fewer pixels where the circular pattern is not seen, CVE values are comparable to one and it means that the estimate of LASSO is equivalent to the zero vector, a nonsense solution. Consequently, the behavior of CVE values are considered to be useful for evaluating the reliability of the data. Future work will complement the theoretical approach to the role of CVE.

4.5 Discussion

We have explained the performance of compressed sensing when it is applied to STS measurement. We demonstrated that LASSO enables us to obtain the circular pattern on scattering maps from partial data of STS. Besides the analysis method, we proposed

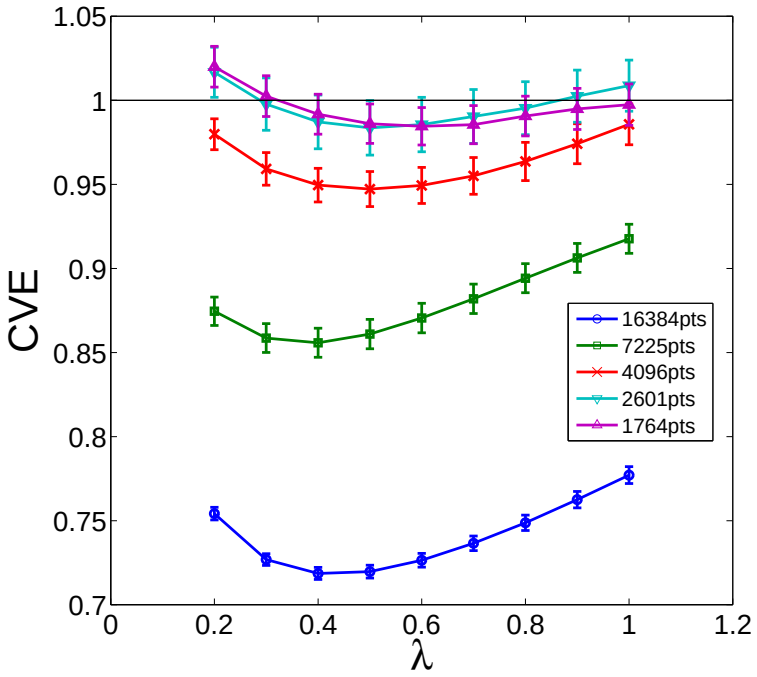

Figure 4.13: Plots of CVE values against λ calculated in 10-fold cross validation to determine the value of λ to obtain Figs. 4.9 and 4.12.

a new measurement method of random sampling and revealed that the random sampling is effective in the removal of aliasing. It is always controversial whether the quality of measurement is enough or not, but we showed a possibility that CVE plays a role of criterion for the judgment.

We have shown that compressed sensing is useful for recovering the circle on the $\boldsymbol{q}$-space, but our end goal is the dispersion relation of materials in the $(\boldsymbol{k}, E)$-space, that is represented by a parabola (refer to Fig. 4.3(a)) or more complicated forms. Obviously, we should study more about measurement along the energy axis E. There is still room to improve it from both the aspect of data analysis and the aspect of measurement method. A more challenging topic is how to transform the $\boldsymbol{k}$-space representation from the $\boldsymbol{q}$-space representation. Let us recall Eq. (4.10) to find that both representations are connected in a nonlinear way. In order to solve this nonlinear problem, it is considered to be promising to compare STS data with other data from angle resolved photoemission spectroscopy [21, 55, 2] and *ab initio* calculation [79, 78].

Chapter 5

Solution-Space Analysis

5.1 Sparse approximation problem

Let us formulate the problem of sparse approximation. Given a data vector $\boldsymbol{y} \in \mathbb{R}^M$ and a proper basis matrix $\boldsymbol{A} = (\boldsymbol{a}_1, \ldots, \boldsymbol{a}_N) \in \mathbb{R}^{M \times N}$, the purpose of sparse approximation is to find a sparse vector $\boldsymbol{x} \in \mathbb{R}^N$, the number of whose non-zero elements is K ($< M$), such that the data is represented in the following way,

$$\boldsymbol{y} \approx \boldsymbol{A}\boldsymbol{x}, \tag{5.1}$$

keeping the distortion as small as possible. We measure the distortion ϵ using a mean squared error,

$$\epsilon \;=\; \frac{1}{2M}||\boldsymbol{y} - \boldsymbol{A}\boldsymbol{x}||_2^2, \tag{5.2}$$

where $||\cdot||_2$ is the l_2-norm of a vector, defined as $||\boldsymbol{y}||_2 = \sqrt{\sum_i y_i^2}$. In addition, We call the constant $r = K/M$ the compression rate. We are interested in the performance of sparse approximation evaluated by the relation between the distortion and the compression rate.

Conventional methods of sparse approximation employ a square basis matrix such as Fourier and wavelet bases. In order to achieve a good trade-off relation, we discuss the use of an overcomplete basis. An overcomplete basis is composed of more column vectors than the dimension of the data vector, namely $N > M$. Thanks to the extra column vectors, this strategy based on overcomplete bases is expected to outperform the conventional methods.

In the discussion of sparse approximation, it is beneficial to divide its procedure into two steps. In the first step basis vectors are selected, often called support estimation, and in the second step the coefficients of basis vectors are determined. Once a certain combination of basis vectors is chosen, it is relatively easy to determine the coefficients so as to minimize the distortion by using the method of least squares. Therefore, we focus on the step of support estimation. Naively, we conceive of calculating the distortion of

all possible combinations of basis vectors and choosing the optimal combination. We call this the exhaustive-search method. We will analyze the performance when the exhaustive-search method is carried out exactly, using methods of statistical mechanics.

The exhaustive-search method is, if conducted literally, an absolute method, but is not practical from the viewpoint of computational complexity. There are ${}_N\mathrm{C}_K$ options of selecting K basis vectors among N ones, and it causes a combinatorial explosion. It is important to develop an efficient method of choosing proper basis vectors used to represent the data. We discuss the convex-relaxation and greedy approaches to design a useful method of basis selection. Our adoption of these approaches is motivated by their application in compressed sensing to decrease computational time. We will examine the performance of these algorithms.

5.2 Performance of the overcomplete-basis strategy

The distortion of sparse approximation is highly affected by the result of support estimation. It is important to analyze a histogram which represents a frequency distribution of distortion values when all possible sets of basis vectors are examined. We will analyze it using methods of statistical mechanics. Statistical mechanics provides useful methods of analyzing behaviors of systems in the large-size limit, $M \to +\infty$ with $r = K/M$ and $\alpha = N/M$ fixed, called the thermodynamic limit. We note that the definition of α here is different from that in Chap. 3. The meaning of α here is the degree of overcompleteness here, while in Chap. 3 it means how small the number of measurements is compared to the number of unknown variables. In the context of statistical mechanics, the frequency distribution can be regarded as the Boltzmann entropy. The minimum distortion value is evaluated at the zero-entropy point.

For the sake of simplicity, our analysis deals with the situation where the data are composed of independent and identically distributed random variables from a normal distribution whose mean and variance are zero and σ_y^2 respectively, denoted by $\mathcal{N}(0, \sigma_y^2)$, and a basis whose components are independent and identically distributed random variables from $\mathcal{N}(0, M^{-1})$ is used.

5.2.1 Theoretical analysis

In order to interpret the problem of support estimation as that of statistical mechanics, let us introduce a binary vector $\boldsymbol{c} \in \{1, 0\}^N$ to store information on whether each basis vector is chosen ($c_i = 1$) or not ($c_i = 0$), and then they can be regarded as spin variables. We discuss a system characterized by a Hamiltonian,

$$\mathcal{H}_{\mathrm{ls}}(\boldsymbol{c}; \beta_1) = -\frac{1}{\beta_1} \ln \int \mathrm{d}_{\boldsymbol{c}}\boldsymbol{x} \mathrm{e}^{-\frac{\beta_1}{2}||\boldsymbol{y}-\boldsymbol{A}(\boldsymbol{c}\circ\boldsymbol{x})||_2^2}, \tag{5.3}$$

where $\circ$ represents the Hadamard product of two vectors, defined as $(\boldsymbol{v} \circ \boldsymbol{w})_i = v_i w_i$, $\int \mathrm{d}_{\boldsymbol{c}}\boldsymbol{x} = \prod_{i=1}^N \int \mathrm{d}_{c_i} x_i$, and $\int \mathrm{d}_{c_i} x_i = \int \mathrm{d}x_i$ ($c_i = 1$) or 1 ($c_i = 0$). This Hamiltonian is

related to the cost function of the method of least squares, when a set of basis vectors labeled by $\boldsymbol{c}$ is used, as follows:

$$\mathcal{H}_{\rm ls}(\boldsymbol{c};\beta_1) \to \min_{\boldsymbol{x}} \frac{1}{2}||\boldsymbol{y}-\boldsymbol{A}(\boldsymbol{c}\circ\boldsymbol{x})||_2^2, \text{ as } \beta_1 \to +\infty. \tag{5.4}$$

The parameter β_1 plays a role of inverse temperature regarding the use of the method of least squares, and taking the limit of $\beta_1 \to +\infty$ corresponds to carrying out the least-squares methods. Based on this Hamiltonian, we naturally introduce a canonical distribution of spin variables $\boldsymbol{c}$ as follows:

$$p(\boldsymbol{c}|\beta) = \frac{1}{Z(\beta)}\delta(||\boldsymbol{c}||_0 - K)\mathrm{e}^{-\beta\mathcal{H}_{\rm ls}(\boldsymbol{c};\beta_1)}, \tag{5.5}$$

where $||\cdot||_0$ denotes the so-called l_0-norm of a vector. The l_0-norm represents the number of non-zero elements of a vector, defined as $||\boldsymbol{v}||_0 = \sum_i |v_i|_0$, where $|v_i|_0$ is equal to 1 ($v_i \neq 0$) or 0 ($v_i = 0$). The normalization factor Z is called a partition function, defined as

$$Z(\beta) = \sum_{\boldsymbol{c}} \delta(||\boldsymbol{c}||_0 - K)\mathrm{e}^{-\beta\mathcal{H}_{\rm ls}(\boldsymbol{c},\beta_1)}. \tag{5.6}$$

The parameter β plays a role of inverse temperature regarding the step of support estimation. Taking the limit of $\beta \to +0$ tells us the performance in the case of random choice, and better sets of basis vectors tend to be sampled from a canonical distribution with a larger β.

The typical value of the distortion at a temperature point β is given by

$$\epsilon(\beta) = \lim_{\beta_1\to+\infty} \frac{1}{M}\left[\langle\mathcal{H}_{\rm ls}(\boldsymbol{c};\beta_1)\rangle_{\boldsymbol{c}|\beta}\right]_{\boldsymbol{y},\boldsymbol{A}}, \tag{5.7}$$

where $\langle\cdot\rangle_{\boldsymbol{c}|\beta}$ represents the thermal average with regard to $\boldsymbol{c}$, and $[\cdot]_{\boldsymbol{y},\boldsymbol{A}}$ represents the configurational average with regard to $\boldsymbol{y}$ and $\boldsymbol{A}$. Employing the partition function Z, the distortion is also expressed as

$$\epsilon(\beta) = \lim_{\beta_1\to+\infty} -\frac{1}{M}\frac{\partial}{\partial\beta}[\ln Z(\beta)]_{\boldsymbol{y},\boldsymbol{A}}. \tag{5.8}$$

Now, let us define an entropy-density function of interest as

$$s(\epsilon,\beta_1) = \frac{1}{M}\ln\left(\#\{\boldsymbol{c} \mid ||\boldsymbol{c}||_0 = Mr \wedge \mathcal{H}_{\rm ls}(\boldsymbol{c};\beta_1) = M\epsilon\}\right), \tag{5.9}$$

and then the partition function can be also expressed as

$$Z(\beta,\beta_1) = \sum_{\epsilon} \mathrm{e}^{M(s(\epsilon,\beta_1)-\beta\epsilon)}. \tag{5.10}$$

In the thermodynamic limit $M \to +\infty$ as will be taking, the typical value of the entropy density is also expressed as a function of β

$$s(\beta) = \beta\epsilon(\beta) + \lim_{\beta_1 \to +\infty} \frac{1}{M}[\ln Z(\beta, \beta_1)]_{\boldsymbol{y},\boldsymbol{A}}. \tag{5.11}$$

For the sake of convenience, we define a free-energy density as

$$f(\beta) = \lim_{\beta_1 \to +\infty} -\frac{1}{M\beta}[\ln Z(\beta, \beta_1)]_{\boldsymbol{y},\boldsymbol{A}}, \tag{5.12}$$

and its relations to the distortion and the entropy density are given by

$$\epsilon(\beta) = \frac{\partial}{\partial\beta}(\beta f(\beta)), \tag{5.13}$$

$$s(\beta) = \beta(\epsilon(\beta) - f(\beta)). \tag{5.14}$$

The point of the analysis is assessing the free-energy density f in the thermodynamic limit. Though the details of calculation are described in Appendix B.1, this assessment can be performed by using the saddle-point method and the replica method, which yields

$$\begin{aligned} &\lim_{M\to\infty} f(\beta) \\ = \; & -\frac{1}{\beta}\left[\frac{1}{2}\ln\frac{1+\chi_1}{1+\chi_1+\beta(Q-q)} - \frac{\beta}{2}\frac{q+\sigma_y^2}{1+\chi_1+\beta(Q-q)}\right. \\ & +\hat{r}r + \beta(\hat{Q}Q - (\hat{\chi}_1+\hat{q})\chi_1) - \beta^2((\hat{\chi}_1+\hat{q})Q - \hat{q}q) \\ & \left.-\alpha\int \mathrm{D}z \ln(1-\rho(z))\right], \end{aligned} \tag{5.15}$$

where

$$\rho(z) = \frac{1}{\sqrt{\frac{\hat{Q}-\beta\hat{\chi}_1}{\hat{Q}}}\exp\left[\hat{r} - \frac{\beta}{2}\frac{\hat{q}}{\hat{Q}-\beta\hat{\chi}_1}z^2\right] + 1}, \tag{5.16}$$

and the parameters $\{Q, \chi_1, q, \hat{r}, \hat{Q}, \hat{\chi}_1, \hat{q}\}$ are substituted for by the solution of the

equations of state:

$$\hat{Q} = \frac{1}{2}\frac{1}{1+\chi_1}, \tag{5.17a}$$

$$\hat{\chi}_1 = \frac{1}{2}\frac{Q-q}{(1+\chi_1)(1+\chi_1+\beta(Q-q))}, \tag{5.17b}$$

$$\hat{q} = \frac{1}{2}\frac{q+\sigma_y^2}{(1+\chi_1+\beta(Q-q))^2}, \tag{5.17c}$$

$$r = \alpha \int \mathrm{D}z\rho(z), \tag{5.17d}$$

$$Q = \alpha \int \mathrm{D}z\rho(z)\left(\frac{1}{2}\frac{\hat{\chi}_1}{\hat{Q}(\hat{Q}-\beta\hat{\chi}_1)} + \frac{1}{2}\frac{\hat{q}}{(\hat{Q}-\beta\hat{\chi}_1)^2}z^2\right), \tag{5.17e}$$

$$\chi_1 = \alpha \int \mathrm{D}z\rho(z)\left(\frac{1}{2}\frac{1}{\hat{Q}}\right), \tag{5.17f}$$

$$q = \frac{\alpha}{\beta}\int \mathrm{D}z\rho(z)\left(\frac{1}{2}\frac{1}{\hat{Q}-\beta\hat{\chi}_1} - \frac{1}{2}\frac{\hat{Q}-\beta(\hat{\chi}_1+\hat{q})}{(\hat{Q}-\beta\hat{\chi}_1)^2}z^2\right). \tag{5.17g}$$

The distortion and the entropy density are analyzed as follows:

$$\lim_{M\to+\infty}\epsilon(\beta) = \hat{\chi}_1+\hat{q}, \tag{5.18}$$

$$\lim_{M\to+\infty}s(\beta) = \beta(\epsilon(\beta)-f(\beta)). \tag{5.19}$$

5.2.2 Numerical Analysis

When the system size M is sufficiently small, we can obtain the free-energy density f by exhaustively searching all possible combinations of basis vectors. In the case where M is less small, we use the exchange Monte Carlo method to sample basis vector combinations obeying the canonical distribution at various temperature points [99, 56], and then are able to estimate the free-energy density f using the multi-histogram method [34].

In simulations, we set $\sigma_y^2 = 1$ and $\alpha = 2$. We treat two values of r equal to 0.2 and 0.4. In the case of $r = 0.2$ (0.4), we calculate the values of free-energy density at 15 temperature points, which are distributed according to a geometric progression in the range between 1 and 10 (between 1 and 35) in the value of β. We conduct the exhaustive-search method for $M \leq 25$ (15), and use the exchange Monte Carlo method for larger M. The configurational average with regard to $(\boldsymbol{y}, \boldsymbol{A})$ is dealt with by taking the median over 1000 different trials. The error bars are estimated by using the Bootstrap method.

The exchange Monte Carlo simulations are conducted as follows. At every temperature point, we randomly choose the initial vector $\boldsymbol{c}$ among those satisfying $||\boldsymbol{c}||_0 = K$. For $r = 0.2$, the number of Monte Carlo steps required for sufficient sampling is $2, 3, 4, 7, 10 \times 10^4$

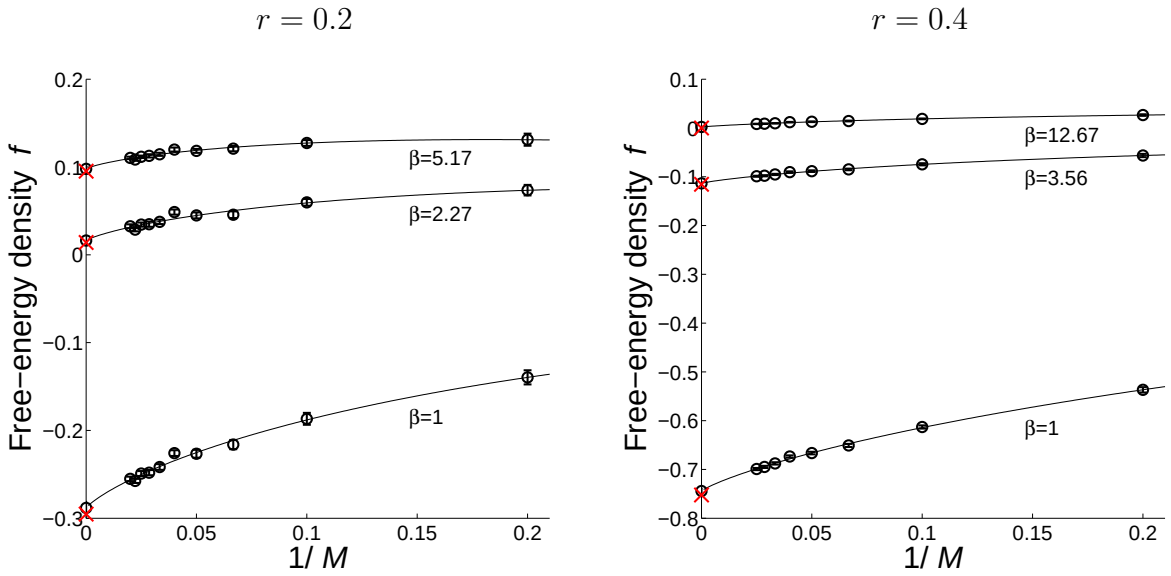

Figure 5.1: Theoretically and numerically estimated free-energy density values f at some temperature points β. Red crosses and black circles on the vertical axis represent theoretical and numerical estimates, respectively. Numerical estimates are extrapolated from the results of finite-size numerical simulations, represented by black circles. Some error bars are smaller than markers. The related parameters are set to $\sigma_y^2 = 1$, $\alpha = 2$, and $r = 0.2$ (left), 0.4 (right).

for $M = 30, 35, 40, 45, 50$, respectively, while for $r = 0.4$ it is $2, 4, 8, 15, 30 \times 10^4$ for $M = 20, 25, 30, 35, 40$, respectively. The first half of the Monte Carlo steps are discarded in order to decrease the effects of initial values. One Monte Carlo step consists of two parts. First, updating once at every temperature point, and then exchanging once between every pair of neighboring temperature points. In each update of $\boldsymbol{c}$, we randomly choose one index i such that $c_i = 0$ and another j such that $c_j = 0$ to flip into the opposite state, namely we set $c_i = 0$ and $c_j = 1$, and accept or reject this trial according to the Metropolis criterion [76]. The Metropolis criterion is also used in $\boldsymbol{c}$'s exchange between different temperature points.

The results of numerical simulations are shown in Fig. 5.1. Numerically estimated free-energy density values f are represented by black circles on the vertical axis. They are extrapolated from finite-size results by linear regression, in which the asymptotic form is given by $f \approx a + bM^{-1} + cM^{-1} \ln M^{-1}$. This asymptotic form is exact at $\beta = 0$ as is derived from Stirling's approximation,

$$M! \approx \sqrt{2\pi M} \left(\frac{M}{\mathrm{e}} \right)^M \quad \text{if } M \gg 1, \tag{5.20}$$

and this exactness motivates us to employ the same form for $\beta \neq 0$ as well. Theoretically estimated values, Eq. (5.15), are represented by red crosses in Fig. 5.1. We compare

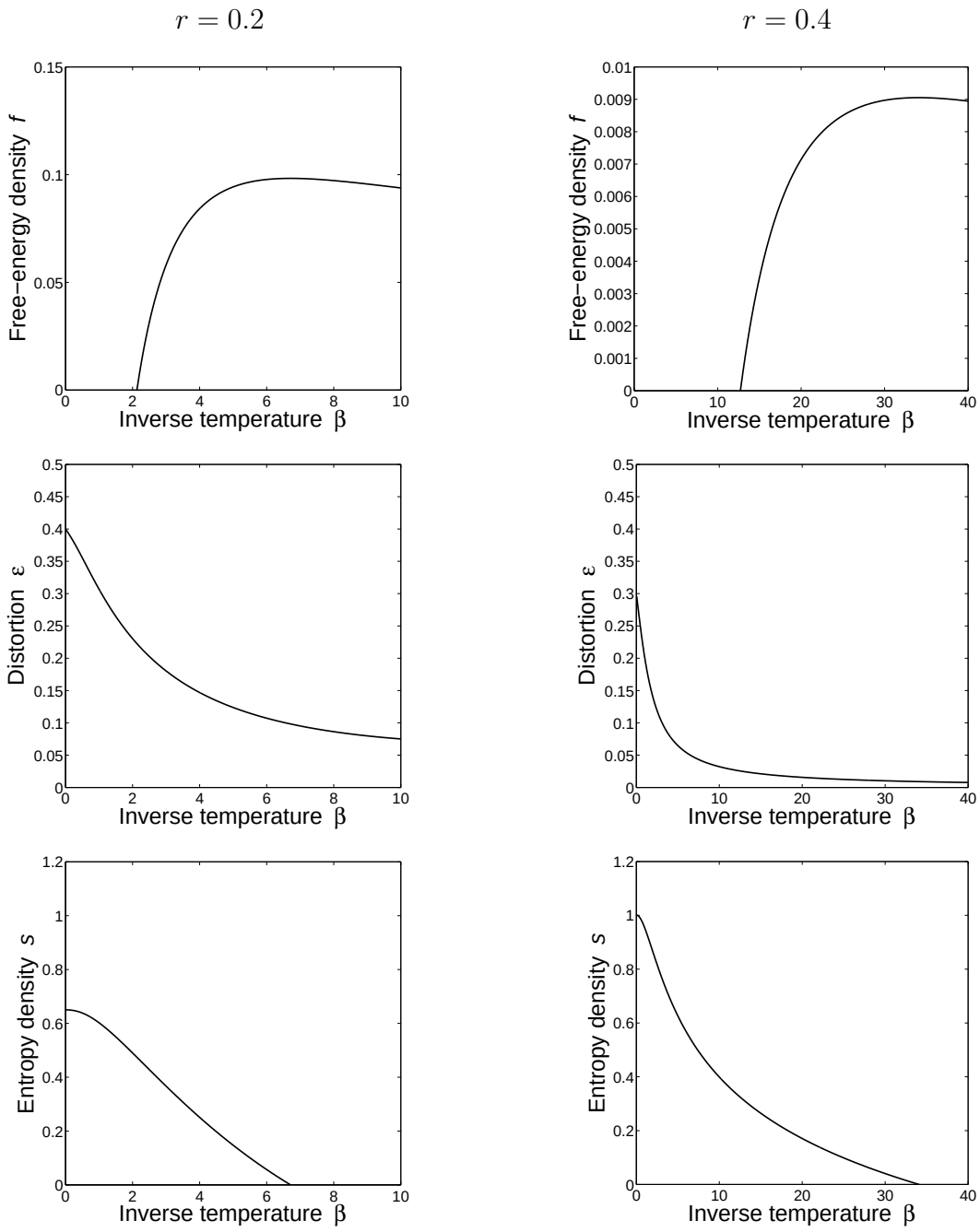

Figure 5.2: Theoretically estimated free-energy density f, distortion ϵ, and entropy density s. The related parameters are set to $\sigma_y^2 = 1$, $\alpha = 2$, and $r = 0.2$ (left), 0.4 (right).

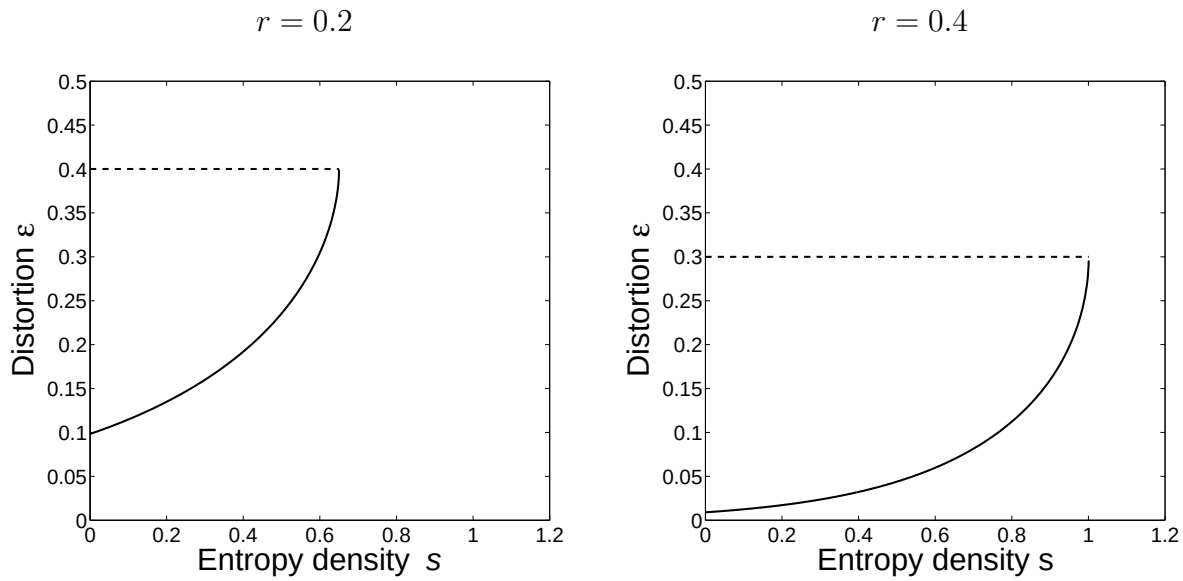

Figure 5.3: Plots of entropy density s against distortion ϵ. The related parameters are set to $\sigma_y^2 = 1$, $\alpha = 2$, and $r = 0.2$ (left), 0.4 (right).

theoretically and numerically estimated values to find that they are very close to each other. Consequently, our theoretical analysis is considered to be correct.

5.2.3 Trade-off relation

We discuss the relation between the distortion and the compression rate from the results of our theoretical analysis. The theoretically estimated free-energy density f, distortion ϵ, and entropy density s are shown in Fig. 5.2. There is a significant point where the entropy is equal to zero. Zero entropy means that there is only one set of basis vectors which gives the corresponding distortion value. Conversely, it is impossible for our overcomplete-basis strategy to achieve a smaller distortion. Then, the region of smaller β than the zero-entropy point is of interest. In the region of interest, the free-energy is a monotonically increasing function of β. Without any computational cost, the state tends to be $\beta \to 0$ according to the slope of the free-energy. In this way, we are convinced that the random method is related to the limit of $\beta \to 0$. When we spend so much computational cost as to conduct the exhaustive-search method, the state is brought up to the summit of the free energy and the minimum value of distortion is achieved.

Figure 5.3 plots the entropy density s against the distortion ϵ. The curves in Fig. 5.3 are equivalent to the frequency distributions of all the values of distortion that are smaller than one obtained by the random method. The entropy has the maximum at the random-method point and decreases as the distortion decreases. The value of distortion at the zero-entropy point is explicitly shown and the minimum distortion is smaller in the case of $r = 0.4$ than in the case of $r = 0.2$. In Fig. 5.4, the compression rate is plotted

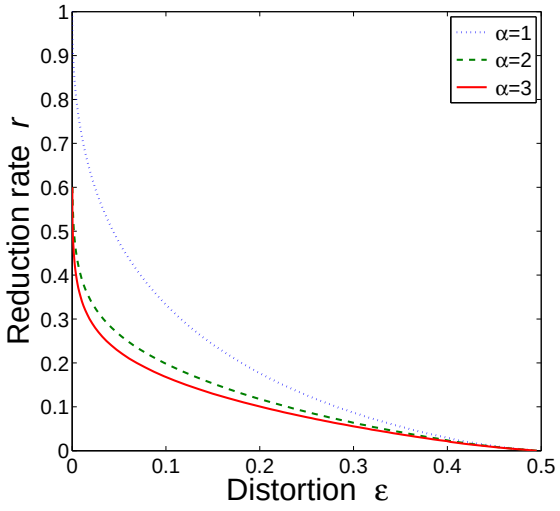

Figure 5.4: Plots of compression rate r against distortion ϵ obtained by the exhaustive-search method. The related parameters are set to $\sigma_y^2 = 1$, $\alpha = 1, 2, 3$.

against the distortion. It is certain that there is a trade-off relation between the distortion and the compression rate, regardless of the degree of overcompleteness represented by the parameter α. Another interesting finding is that the trade-off curve is nearer to the origin as α is larger. When the degree of overcompleteness increases, the performance of sparse approximation improves.

5.3 Performance of practical algorithms

We have seen that the overcomplete-basis strategy is promising for the task of sparse approximation. However, it is more difficult to choose the best combination of basis vectors when the degree of overcompleteness is higher. It is important to investigate the performance of well-known sparseness-inducing algorithms and to develop an practical and efficient algorithm.

As stated above, an absolute method is the exhaustive-search method, but it causes a combinatorial explosion. If one selects basis vectors randomly, the distortion value is given by

$$\lim_{M \to +\infty} \epsilon = \frac{1 - r}{2} \sigma_y^2, \tag{5.21}$$

as mentioned at the end of Appendix B.1. In order to improve the practical performance, we examine the performance of least absolute shrinkage and selection operator (LASSO) and orthogonal matching pursuit (OMP) when they are used for sparse approximation.

LASSO and OMP are representative algorithms of the convex-relaxation approach and of the greedy approach, respectively. Both algorithms are famous in the context of compressed sensing and refer to Sec. 3.2 and Sec. 4.3.

5.3.1 Least absolute shrinkage and selection operator

Least absolute and shrinkage and selection operator (LASSO) is carried out by solving the following minimization problem

$$\min_{\boldsymbol{x}} \left\{ \frac{1}{2}||\boldsymbol{y} - \boldsymbol{A}\boldsymbol{x}||_2^2 + \lambda||\boldsymbol{x}||_1 \right\}, \tag{5.22}$$

where $||\cdot||_1$ is the l_1-norm of a vector, defined by $||\boldsymbol{x}||_1 = \sum_i |x_i|$, with the absolute value denoted by $|\cdot|$. LASSO is not so computationally hard because the minimization problem can be reformulated as a form of quadratic programming, that is carried out exactly with $O(M^3)$ computational cost. In addition, the l_1-norm term causes the sparsifying effect of choosing a small set of basis vectors and its coefficient λ can be adjusted according to the desired compression rate.

Unfortunately, LASSO alone is not considered to work well in sparse approximation because the intention to minimize distortion might be blurred by the l_1-norm term. To remove the extra distortion caused by the l_1-norm term, we propose that, after the support estimation of the compressed vector obtained by LASSO, the values of coefficients are determined again by the method of least squares. When the solution of LASSO is denoted by $\boldsymbol{\gamma}$, this procedure is described as follows:

$$\min_{\boldsymbol{x}} \frac{1}{2}||\boldsymbol{y} - \boldsymbol{A}(|\boldsymbol{\gamma}|_0 \circ \boldsymbol{x})||_2^2, \tag{5.23}$$

where $|\cdot|_0$ of a vector is defined as $(|\boldsymbol{\gamma}|_0)_i = |\gamma_i|_0$.

Using methods of statistical mechanics, the performance of LASSO can be evaluated theoretically in a similar way to the analysis of compressed sensing by Kabashima *et al.* [59]. The details of calculation are described in Appendix B.2. The compression rate and the distortion of the compressed vector given by LASSO alone

$$\lim_{M\to+\infty} r = \alpha \mathrm{erfc}(\theta), \tag{5.24}$$

$$\lim_{M\to+\infty} \epsilon_{\mathrm{LASSO}} = \hat{\chi}_p, \tag{5.25}$$

where $\theta = \frac{\lambda}{\sqrt{4\hat{\chi}_p}}$ and $\mathrm{erfc}(\cdot)$ is the complementary error function defined by

$$\mathrm{erfc}(x) = \frac{2}{\sqrt{\pi}} \int_x^{+\infty} \mathrm{d}t \mathrm{e}^{-t^2}. \tag{5.26}$$

The parameter $\hat{\chi}_p$ is substituted for by the solution of the equations of state with regard to $\{P, \chi_p, \hat{P}, \hat{\chi}_p\}$:

$$\hat{P} = \frac{1}{2}\frac{1}{1+\chi_p}, \tag{5.27a}$$

$$\hat{\chi}_p = \frac{1}{2}\frac{P+\sigma_y^2}{(1+\chi_p)^2}, \tag{5.27b}$$

$$P = \alpha\frac{\hat{\chi}_p}{2\hat{P}^2}\left((1+2\theta^2)\mathrm{erfc}(\theta) - \theta\frac{2}{\sqrt{\pi}}\mathrm{e}^{-\theta^2}\right), \tag{5.27c}$$

$$\chi_p = \alpha\frac{1}{2\hat{P}}\mathrm{erfc}(\theta), \tag{5.27d}$$

When the method of least squares is operated after LASSO, the compression rate does not change, but the distortion probably improves, We can also assess the distortion obtained by the method of least squares after LASSO using a statistical-mechanical technique developed to analyze the systems described by the so-called Franz-Parisi potential [39]. For the details of calculation, see Appendix B.2. According to our analysis, the distortion is given by

$$\lim_{M\to+\infty}\epsilon = \hat{\chi}_q. \tag{5.28}$$

The parameter $\hat{\chi}_q$ is substituted for by the solution of the equations of state with regard

to $\{C, \chi_c, Q, \chi_q, \hat{C}, \hat{\chi}_c, \hat{Q}, \hat{\chi}_q\}$,

$$\hat{C} = \frac{1}{2}\frac{\chi_c}{1+\chi_p}\frac{1}{1+\chi_q}, \tag{5.29a}$$

$$\hat{\chi}_c = -\frac{1}{2}\frac{\chi_c}{(1+\chi_p)^2}\frac{P+\sigma_y^2}{1+\chi_q} + \frac{1}{2}\frac{1}{1+\chi_p}\frac{C+\sigma_y^2}{1+\chi_q}, \tag{5.29b}$$

$$\hat{Q} = \frac{1}{2}\frac{1}{1+\chi_q}, \tag{5.29c}$$

$$\hat{\chi}_q = \frac{1}{2}\left(\frac{\chi_c}{1+\chi_p}\right)^2\frac{P+\sigma_y^2}{(1+\chi_q)^2} - \frac{\chi_c}{1+\chi_p}\frac{C+\sigma_y^2}{(1+\chi_q)^2} + \frac{1}{2}\frac{Q+\sigma_y^2}{(1+\chi_q)^2}, \tag{5.29d}$$

$$C = \alpha\frac{\hat{\chi}_p}{2\hat{P}\hat{Q}}\left(\left(\frac{\hat{\chi}_c}{\hat{\chi}_p} + (1+2\theta^2)\frac{\hat{C}}{\hat{P}}\right)\mathrm{erfc}(\theta) - \frac{\hat{C}}{\hat{P}}\theta\frac{2}{\sqrt{\pi}}\mathrm{e}^{-\theta^2}\right), \tag{5.29e}$$

$$\chi_c = \alpha\frac{1}{2\hat{Q}}\left(\frac{\hat{C}}{\hat{P}}\mathrm{erfc}(\theta) + \frac{\hat{\chi}_c}{\hat{\chi}_p}\theta\frac{2}{\sqrt{\pi}}\mathrm{e}^{-\theta^2}\right), \tag{5.29f}$$

$$Q = \alpha\frac{\hat{\chi}_p}{2\hat{Q}^2}\left(\left(\frac{\hat{\chi}_q}{\hat{\chi}_p} + 2\frac{\hat{\chi}_c}{\hat{\chi}_p}\frac{\hat{C}}{\hat{P}} + (1+2\theta^2)\frac{\hat{C}^2}{\hat{P}^2}\right)\mathrm{erfc}(\theta) + \left(\frac{\hat{\chi}_c^2}{\hat{\chi}_p^2} - \frac{\hat{C}^2}{\hat{P}^2}\right)\theta\frac{2}{\sqrt{\pi}}\mathrm{e}^{-\theta^2}\right), \tag{5.29g}$$

$$\chi_q = \alpha\frac{1}{2\hat{Q}}\mathrm{erfc}(\theta) \tag{5.29h}$$

when the solution of the equation of state with regard to $\{P, \chi_p, \hat{P}, \hat{\chi}_p\}$ is substituted.

When the system size M is finite, we can carry out LASSO exactly. We extrapolate the compression rate and the distortion in the thermodynamic limit of $M \to +\infty$ from the results of finite-size systems and check if our theoretical analysis is valid. In numerical simulations, we set $\sigma_y^2 = 1$ and $\alpha = 2$. We treat two values of λ equal to 1 and 2. We use a method of quadratic programming to obtain compression rate r and distortion before and after the method of least squares, $\epsilon_{\mathrm{LASSO}}$ and ϵ. The configurational average with regard to $(\boldsymbol{y}, \boldsymbol{A})$ is dealt with by taking the median over 1000 different trials. The error bars are estimated by using the Bootstrap method.

The results of numerical simulations are shown in Fig. 5.5. Numerically estimated values in the thermodynamic limit are represented by black circles on the vertical axis. They are extrapolated from finite-size results by linear regression, in which the asymptotic form is given by $r \approx a_0 + a_1 M^{-1}$, $\epsilon_{\mathrm{LASSO}} \approx b_0 + b_1 M^{-1}$, and $\epsilon \approx c_0 + c_1 M^{-1}$. Theoretically estimated values are represented by red crosses in Fig. 5.5. We compare theoretically and numerically estimated values to see that they are very close to each other. Consequently, our theoretical analysis is considered to be valid.

Figure 5.6 plots the compression rate r and the distortion ϵ against the coefficient of the l_1-norm term λ. Judging from the left panel of Fig. 5.6, we see that LASSO has a sparsifying effect thanks to the l_1-norm term and the compression rate can be controlled

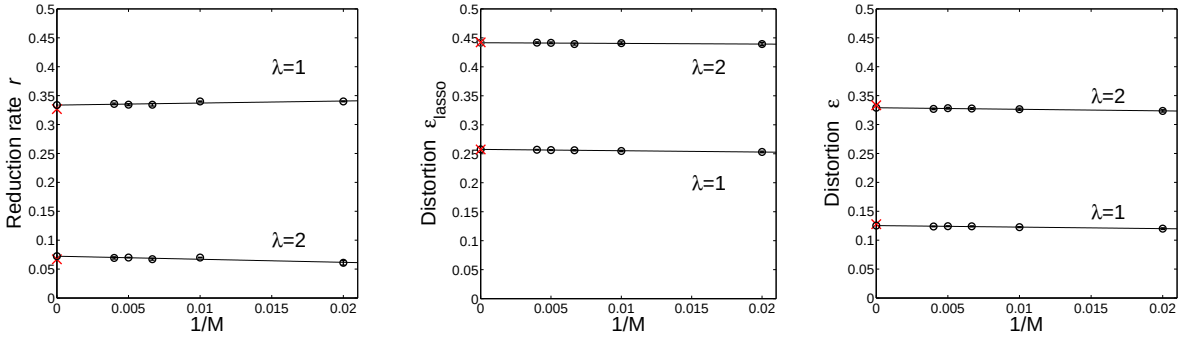

Figure 5.5: Theoretically and numerically estimated performance of LASSO. Red crosses and black circles on the vertical axis represent theoretical and numerical estimates, respectively. Numerical estimates are extrapolated from the results of finite-size numerical simulations, represented by black circles. Some error bars are smaller than markers. The related parameters are set to $\sigma_y^2 = 1$, $\alpha = 2$, and $\lambda = 1, 2$. The compression rate r, the distortion obtained by LASSO alone $\epsilon_{\mathrm{LASSO}}$, and the distortion obtained by the method of least squares after LASSO ϵ are shown from the left.

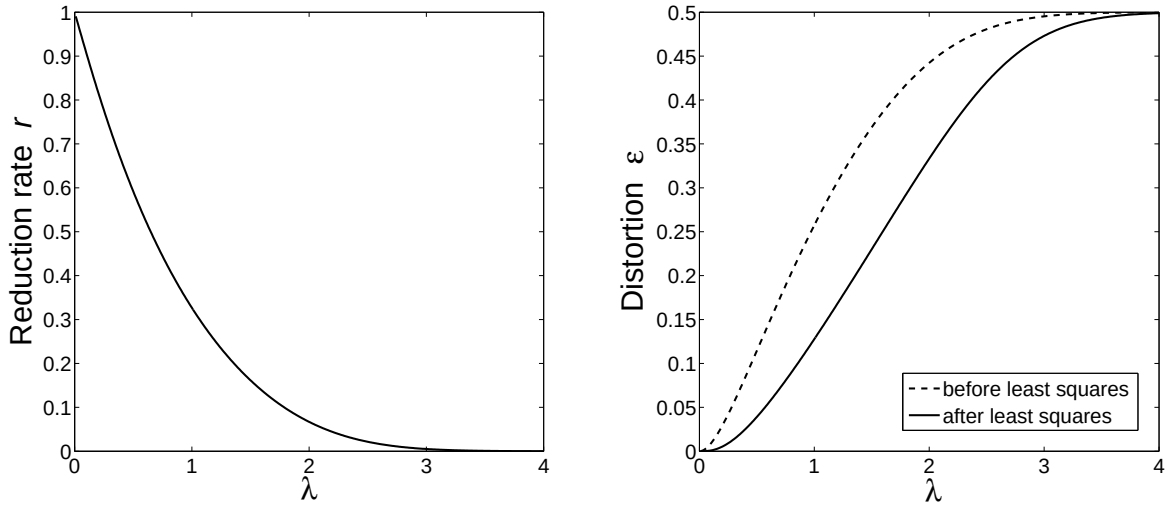

Figure 5.6: Plots of theoretically estimated compression rate and distortion against λ. The related parameters are set to $\sigma_y^2 = 1$ and $\alpha = 2$.

by changing the value of its coefficient λ. However, in the right panel, we find that the distortion obtained by LASSO alone is larger than that after using the method of least squares. We infer that this inferiority of LASSO alone can be attributed to the l_1-norm term. When LASSO is used for sparse approximation, it should be accompanied with the method of least squares to decrease the distortion. Figure 5.7 plots the compression rate against the distortion obtained by the method of least squares after LASSO. The

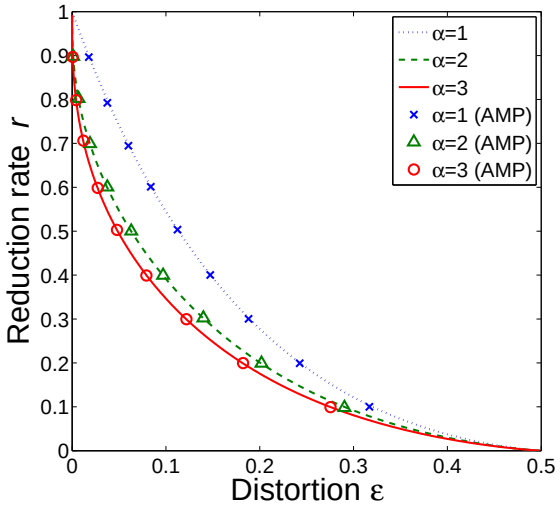

Figure 5.7: Plots of compression rate r against distortion ϵ obtained by the method of least squares after LASSO. The lines represent theoretical estimates. The circles, triangles and crosses represent extrapolated estimates from finite-size results when approximate message passing is used to carry out LASSO. The extrapolation is conducted in the same way as shown in Fig. 5.5. The related parameters are set to $\sigma_y^2 = 1$, $\alpha = 1, 2, 3$.

performance of LASSO has a trade-off relation between the compression rate and the distortion as well and improves as a more overcomplete basis is used.

Approximate message passing (AMP) is based on the concept of belief propagation and is a useful algorithm to execute LASSO. LASSO is often carried out exactly as a quadratic programming with a computational cost of order $O(M^3)$. In contrast, AMP only requires a computational time of order $O(M^2)$ per update. In spite of the low computational cost, as shown in Fig. 5.7, the performance achieved by AMP is very close to the theoretically estimated performance of LASSO.

5.3.2 Orthogonal matching pursuit

Orthogonal matching pursuit (OMP) is a well-known algorithm of the greedy approach. OMP requires a polynomial computational complexity of order $O(M^4)$ and is considered to be practical. We examine the performance of OMP when it is applied for sparse approximation. Numerically extrapolated performance of OMP in the thermodynamic limit is shown in Fig. 5.8. From the results of OMP, we are convinced of the trade-off relation in the task of sparse approximation. As well as the exhaustive-search method and LASSO, the performance is enhanced with a more overcomplete basis. This indicates that, regardless of methods, the overcompleteness of a basis is effective for sparse approximation.

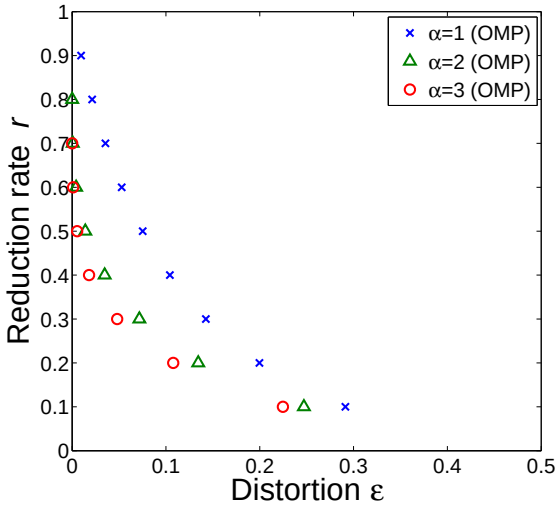

Figure 5.8: Plots of compression rate r against distortion ϵ obtained by orthogonal matching pursuit. The circles, triangles and crosses represent extrapolated estimates from finite-size results. The extrapolation is conducted in the same way as shown in Fig. 5.5. The related parameters are set to $\sigma_y^2 = 1$, $\alpha = 1, 2, 3$.

We compare the performance of OMP with that of the random method, LASSO, and the exhaustive-search method. Figure 5.9 shows the trade-off relation achieved by each of the methods. We claim that OMP outperforms LASSO as well as the random method, though it does not come up to the performance of the exhaustive search method. It is expected to be useful to develop an efficient algorithm for sparse approximation from the viewpoint of the greedy approach. In order to design a new algorithm, it is important to analyze OMP in a theoretical way to understand why OMP performs well. Previous studies provided us with a theoretical approach to OMP using a submodular property of set functions [22, 23]. sparse approximation can be regarded as a subset-selection problem and the cost function is expressed as a set function. Then, this approach gives us an upper bound in terms of the value of distortion. The theoretical relation between the compression rate and the distortion is not known and the trade-off relation achieved by greedy algorithms including OMP is a target in future work.

Let us look again at the density of states of the problem of overcomplete sparse approximation, shown in Fig. 5.10. This time, Fig. 5.10 shows the locations of the solutions obtained by various methods examined so far: the exhaustive search method, OMP, LASSO, and the random method. We confirm that this entropy curve has a simple form. The entropy decreases monotonously to zero at a certain distortion value which would probably be obtained by the exhaustive search method. If the solution space has a broad plateau, the entropy curve has an unnatural peak, but such a structure does not

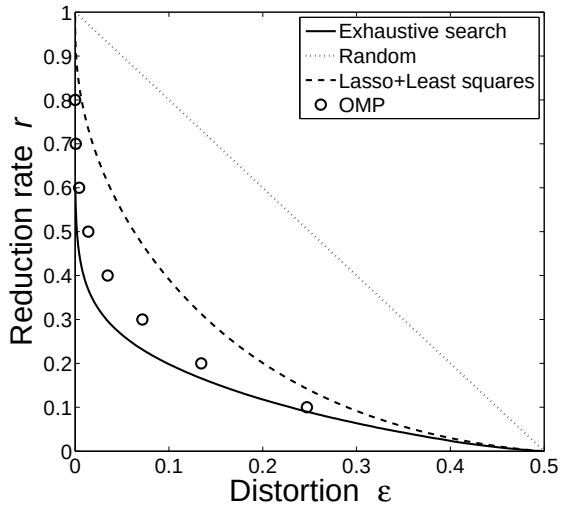

Figure 5.9: Trade-off relations achieved by the exhaustive-search method, the random method, LASSO, and OMP are plotted. The related parameters are set to $\sigma_y^2 = 1$, $\alpha = 2$.

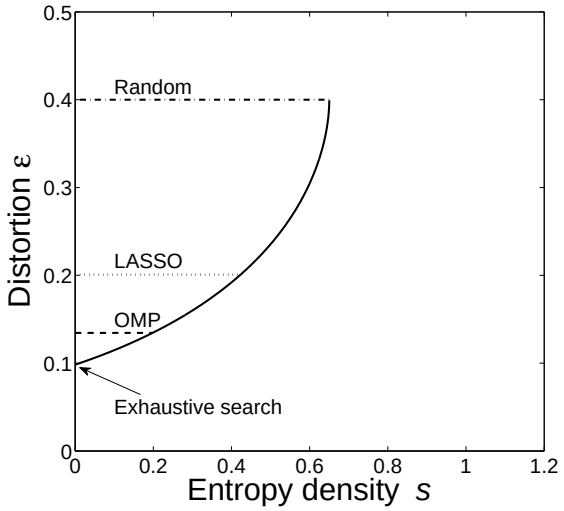

Figure 5.10: The entropy density of the problem of overcomplete sparse approximation and the solutions obtained by various methods: the exhaustive search method, OMP LASSO, and the random method. The related parameters are set to $\sigma_y^2 = 1$, $\alpha = 2$, $r = 0.5$.

exist. It is considered, therefore, that the problem of overcomplete sparse approximation is tractable enough to obtain a better solution with more computational cost.

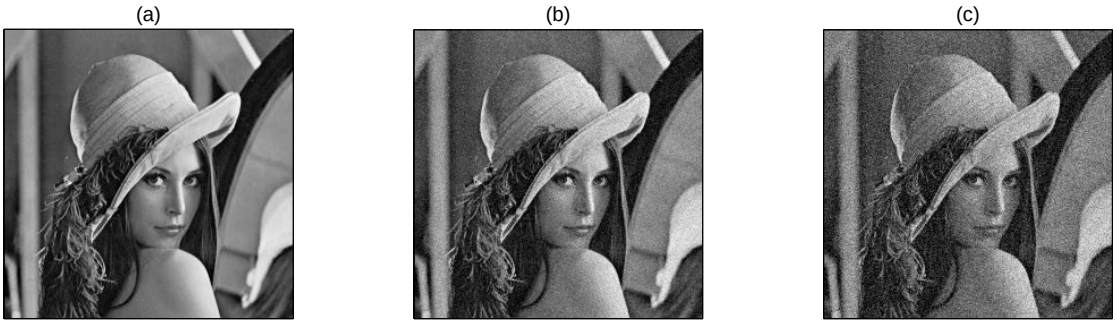

Figure 5.11: Results of image data compression on sparse approximation using the overcomplete basis strategy. The degree of overcompleteness is set to $\alpha = 2$. (a) Original image data. (b) Compressed image data recovered from the representation obtained by OMP. The compression rate is $r = 0.5$. PSNR is 28.2. The time required is approximately 55 sec. (c) Compressed image data recovered from the representation obtained by AMP. The regularization coefficient is $\lambda = 0.65$, so that $r \approx 0.5$. The AMP-compressed representation is given after the method of least squares. PSNR is 22.9. The time required is approximately 4.5 sec.

5.3.3 Application to image data

We investigate the performance of sparse approximation, when it is applied to a task of image data compression. We compress image data composed of 256×256 pixels. The experimental procedure of compression is as follows. First, image data are normalized so as to set the mean and variance to 0 and 1, respectively. Next, 256×256 pixels are randomly permuted, in order to obtain 1024 column vectors, whose dimensionality is 64. Following these operations, the data can be regarded as random numbers with a mean and variance of 0 and 1, which enables us to compare the data with the theoretical analysis we have already conducted. Finally, setting $r = 0.5$, we compress each of the column vectors into a representation vector by using a 64×128 random matrix, namely $\alpha = 2$. We examine the performances of OMP and AMP. When applying AMP, we set the regularization coefficient to 0.65, so that the compression rate r is approximately equal to 0.5, and the method of least squares is operated after carrying out LASSO. The results of experiments are shown in Fig, 5.11. Although OMP requires a computational time that is several times larger than that of AMP, OMP outperforms AMP in terms of appearance and peak signal-to-noise ratio (PSNR), defined by

$$\mathrm{PSNR} = 10 \log_{10} \frac{255^2}{\frac{1}{N} \sum_{ij} (\hat{I}_{ij} - I_{ij})^2}, \tag{5.30}$$

where $\boldsymbol{I} = \{I_{ij}\}$ and $\hat{\boldsymbol{I}} = \{\hat{I}_{ij}\}$ represent an original image and a compressed image, respectively, and N is the number of image pixels.

5.4 Discussion

We have discussed the overcomplete-basis strategy for sparse approximation. The concept of sparse approximation was formulated using statistical mechanics and the performance limit of our strategy was evaluated in terms of compression rate and distortion, using the saddle-point method and the replica ansatzes. In addition, we examined the practical performances of LASSO and OMP when they are used for sparse approximation. We indicated that OMP outperforms LASSO in the context of sparse approximation, which is surprising in light of more popularity of LASSO in compressed sensing. Though there is still room to improve the performance, it is expected that more elaborate greedy algorithms will be developed and available for dictionary learning in future work.

Let us consider the significance of the exhaustive search method and then the solution-space analysis again. Most of the intractable problems in data-driven science has a multivalley structure where exponentially increasing local minima exist or a trade-off relation where several competitive conditions should be fulfilled simultaneously. Originally, the exhaustive search is essential to the discover of the optimal solution in such a complex solution space. For example, in psychiatry, the exhaustive search was used to classify hemodynamic data of near-infrared spectroscopy in an attempt to distinguish two seemingly similar disorders [57]. In geology, the exhaustive search proposes a good geochemical criterion for estimating the inundation area of past tsunamis [67]. In condensed matter physics, a Bayesian framework for the determination of effective Hamiltonian using data of numerical simulation was proposed based on the exhaustive search [100].

When the system size is too large for a combinatorial explosion to be ignored, the exchange Monte Carlo method plays an alternative role of the exhaustive search method [81]. It is well known that the exchange Monte Carlo method searches for the global solution without being trapped in a local solution. An advantage of the exchange Monte Carlo method is that it enables us to visualize the property of solution space efficiently as the entropy function. The landscape of solution space enables us to reveal the limitation of various algorithms and our analysis method and its extension will probably give theoretical evidence.

Chapter 6

Conclusion

We here summarize the innovative points of our three topics: MRF, compressed sensing, and solution-space analysis. First, in the MRF study, we pointed out the correspondence between the diffusion equation and MRF. This correspondence enables us to estimate the diffusion coefficient, a latent variable behind image data, with Bayesian methods. We focused on the posterior distribution itself and explained our proposed method can be used to evaluate the confidence of data as well. Next, a novel application of compressed sensing to experimental physics was reported. We demonstrated that the observation of quasiparticle interference using scanning tunneling microscopy/spectroscopy can be made more efficient by methods of compressed sensing. This application would broaden the horizons of compressed sensing in two points. One is that the results of this experiment can be validated by different experiments and numerical simulations. The other is that the measurement system is simple enough to adapt to newly proposed methods of experiment. Finally, in order to evaluate the difficulty of essential problems in data-driven science, we developed a method for capturing the structure of the solution space. We utilized methods of statistical mechanics to reveal the density of states regarding the problem of overcomplete sparse approximation. Then, the performances of existing algorithms are projected onto the density of states to compare them to the performance limit derived theoretically.

Let us restate the importance of the three levels of data-driven science. The three levels are composed of computational theory, modeling and representation/algorithm. The level of modeling plays the lead role of interface between computational theory (natural science) and representation/algorithm (information science). At the modeling level, the problem to be solved in each field of natural science is explained with as few technical terms of the field as possible. These kinds of deeds would make the essence of problems familiar to people in information science. Not only that, people in natural science would probably learn to recognize similar problems in different disciplines, and the distribution of various methods would become popular, as reported in the article of *Science*. What is most important is that all people share the fundamental problems accumulated through the activities of data-driven science, and then, recall at all times that such sophisticated

problems are worth solving at all costs.

What is the relation between our three topics under the three levels of data-driven science, especially at the modeling level? A little thought of data acquisition itself from the viewpoint of the three levels will show that clearly. The goal of data acquisition is, needless to say, to see unseen objects. There are two strategies to achieve this goal. One is to acquire data as if you took a picture. Of course, nothing of interest appears in the image data explicitly. In this case, it is indispensable to model the natural phenomena and to estimate the unseen structure based on this model. The essence of this procedure is discussed in our MRF study. The other is to make an elaborate measuring system which can manage to look directly at the target. However, the cost of this experiment and the size of equipment tends to increase. Then, we need to model the measurement principles, and to make the most of this model to improve the experiment. Such an attempt is discussed in our research of compressed sensing.

These two strategies of data acquisition have a common issue. In the first strategy, we need to select the most suitable model of the target phenomena, but we take all the scenarios derived from many model candidates into consideration. In the second strategy, a lot of solution candidates remain due to insufficient data, but the best solution is salvaged in accordance with well-calculated measurement principles. Both problems cannot be solved until the whole solution space is searched. Therefore, it is confirmed that our third topic, the solution-space analysis, is beneficial to this issue.

For future work, we will first enhance the modeling level, and then make progress in data-driven science.

At the very beginning, it occurred to us that the solution space of compressed sensing should be analyzed as well as that of sparse approximation. In our research of compressed sensing, we applied LASSO to STM/S measurement as explained in Chapter 4, but it is considered that OMP and the exhaustive-search method outperform LASSO as well as in the case of sparse approximation as explained in Chapter 5. If so, it means that the reduced cost of the experiment can be diverted to a new challenging experiment. Therefore, we are curious about the solution-space analysis of various kinds of practical problems.

Next, how to combine the model of phenomena and the model of measurement to be beneficial is a natural question. The Bayesian framework of distribution estimation explained in Chapter 2 provides a clue to this issue. If the intricate measurement model is represented in a stochastic way as well as the diffusion equation, Bayesian inference connects them seamlessly. After that, we have only to evaluate the confidence of data to judge the appropriateness of experiment to the target phenomenon.

As the discussion at the modeling level heats up, a triangle between phenomenon, measurement, and analysis will be formed there, though there are only three points presented in this thesis now. What to do next is, needless to say, to enlarge the triangle. Indeed, people in natural science return to their own field to confront new problems. However, if they keep the three levels of data-driven science in mind, they are able to project the problems onto the modeling level. In most cases, these problems should be

close to one of the existing modeling topics, and could be solved with a slight modification by people in information science. Even if this is not the case, we can ask whether scientists in other fields of natural science are in similar trouble, and take advantage of an opportunity to discuss together with them. Consequently, the whole of natural science will never fail to be innovated.

Before concluding the thesis, let me introduce a Japanese athlete. His name is So Takei. He won the Japan Decathlon Championship in 1997, and he was part of the team that won the 4×100 meters relay in the World Masters Championship in 2015. I was really impressed with him talking about his way of thinking on a TV program I watched while I was writing this thesis. He said that there is an efficient training method for improving sports, and asked the master of ceremony to extend both arms straight out horizontally with both eyes closed. After doing so, the master opened his eyes to find his arms a little higher, and said optimistically, "Only three centimeters. Good, isn't it?" "Not at all," the athlete answered immediately. He explained seriously that, if you were a baseball player trying to hit a home run, the gap would be fatal. Then, he emphasized that those who aim at a certain sport must first learn to control their own body perfectly, and it is never too late to start the sport after that. In the athlete's arguments, I felt it was something close to data-driven science. How you want to move is at the level of computational theory, and your actual move is at the level of representation and algorithm. The problem is the gap between them. Then, you have to learn to control your body perfectly. This is nothing but the modeling level. At the modeling level, it is alright to begin with a simple move such as raising your arms. Later in the program, the athlete explained what to do to run fast as well, noting that all famous athletes are doing this. It is well-known that fast runners run swinging their arms, but he added why they do this. According to him, this move has an effect of reducing their weight by floating their body. In the language of the three levels, it means that he clearly stated not only the strategy but also its appropriateness. Of course, strength training remains, but it would be at the level of representation and algorithm. The athlete inspired me with the thought that the *three levels of something* applies not only to data-driven science but also to social science, humanities, and sports.

Appendix A

Appendix of Chapter 2

A.1 Correlation of stochastic diffusion systems

Stochastic diffusion systems are described by the following equation,

$$\frac{\partial u}{\partial t}(x,t) = \frac{\partial^2 u}{\partial x^2}(x,t) + \zeta(x,t), \tag{A.1}$$

where $\zeta(x,t)$ represents stochastic fluctuation added at a place and time (x,t). We consider cases where the correlation of the fluctuation is given by

$$\langle \zeta(x_1,t_1)\zeta(x_2,t_2)\rangle = \sigma^2\delta(x_1-x_2)\delta(t_1-t_2). \tag{A.2}$$

Fourier transform is useful for solving Eq. (A.1). We define the Fourier transform of u and ζ by

$$\tilde{u}(q,t) = \frac{1}{\sqrt{2\pi}}\int \mathrm{d}x \mathrm{e}^{\mathrm{i}qx} u(x,t) \tag{A.3a}$$

$$\tilde{\zeta}(q,t) = \frac{1}{\sqrt{2\pi}}\int \mathrm{d}x \mathrm{e}^{\mathrm{i}qx} \zeta(x,t), \tag{A.3b}$$

and then we obtain the Fourier representation of the diffusion equation,

$$\frac{\partial \tilde{u}}{\partial t}(q,t) = -Dq^2\tilde{u}(q,t) + \tilde{\zeta}(q,t). \tag{A.4}$$

The solution of this differential equation is given by

$$\tilde{u}(q,t) = \mathrm{e}^{-Dq^2t}\tilde{u}(q,0) + \int_0^t \mathrm{d}t' \mathrm{e}^{-Dq^2(t-t')}\tilde{\zeta}(q,t'). \tag{A.5}$$

The first term of the right-hand side of Eq. (A.5) can be ignored in the limit of $t \to +\infty$.

We are interested in the following correlation function,

$$C(x_1, x_2, t) = \left\langle \frac{\partial u}{\partial x}(x_1, t) \frac{\partial u}{\partial x}(x_2, t) \right\rangle . \tag{A.6}$$

Employing the Fourier transform of u, we obtain

$$C(x_1, x_2, t) = \frac{1}{2\pi} \int \mathrm{d}q_1 \mathrm{e}^{\mathrm{i}q_1 x_1} (\mathrm{i}q_1) \int \mathrm{d}q_2 \mathrm{e}^{\mathrm{i}q_2 x_2} (\mathrm{i}q_2) \langle \tilde{u}(q_1, t) \tilde{u}(q_2, t) \rangle. \tag{A.7}$$

Substituting the solution, Eq. (A.5), we obtain

$$\begin{aligned} C(x_1, x_2, t) &= \frac{1}{2\pi} \int \mathrm{d}q_1 \mathrm{e}^{\mathrm{i}q_1 x_1} (\mathrm{i}q_1) \int \mathrm{d}q_2 \mathrm{e}^{\mathrm{i}q_2 x_2} (\mathrm{i}q_2) \\ &\quad \times \int_0^t \mathrm{d}t_1' \mathrm{e}^{-Dq_1^2 (t - t_1')} \int_0^t \mathrm{d}t_2' \mathrm{e}^{-Dq_2^2 (t - t_2')} \langle \tilde{\zeta}(q_1, t_1') \tilde{\zeta}(q_2, t_2') \rangle. \end{aligned} \tag{A.8}$$

The property of fluctuation, Eq. (A.2) gives us

$$\langle \tilde{\zeta}(q_1, t_1') \tilde{\zeta}(q_2, t_2') \rangle = \sigma^2 \delta(q_1 + q_2) \delta(t_1' - t_2'), \tag{A.9}$$

where we have used the Fourier representation of the delta function

$$\delta(q) = \frac{1}{2\pi} \int \mathrm{d}x \mathrm{e}^{-\mathrm{i}qx}. \tag{A.10}$$

We substitute Eq. (A.9) into Eq. (A.8) to yield

$$C(x_1, x_2, t) = \frac{\sigma^2}{2D} \delta(x_1 - x_2) \left[1 - \mathrm{e}^{-2Dq^2 t} \right] \tag{A.11}$$

$$\to \frac{\sigma^2}{2D} \delta(x_1 - x_2), \text{ as } t \to +\infty. \tag{A.12}$$

Appendix B

Appendix of Chapter 5

B.1 Entropy of the overcomplete-basis strategy

We explain the calculation of the free-energy density f in detail. Let us introduce a variable $\nu = \beta/\beta_1$ and a function

$$\mathcal{Z}(\boldsymbol{c};\beta,\nu) = \mathrm{e}^{-\frac{\beta}{\nu}\mathcal{H}_{\mathrm{ls}}(\boldsymbol{c};\beta/\nu)}, \tag{B.1}$$

and we obtain

$$f(\beta) = \lim_{\nu\to+0} -\frac{1}{M\beta}\left[\ln\sum_{\boldsymbol{c}}\delta(||\boldsymbol{c}||_0 - Mr)(\mathcal{Z}(\boldsymbol{c};\beta,\nu))^{\nu}\right]_{\boldsymbol{y},\boldsymbol{A}}. \tag{B.2}$$

We define a function

$$g(n,\nu;\beta) = -\frac{1}{M\beta}\ln\left[\left(\sum_{\boldsymbol{c}}\delta(||\boldsymbol{c}||_0 - Mr)(\mathcal{Z}(\boldsymbol{c};\beta,\nu))^{\nu}\right)^n\right]_{\boldsymbol{y},\boldsymbol{A}}, \tag{B.3}$$

to express the free-energy density as

$$f(\beta) = \lim_{n,\nu\to+0}\frac{\partial}{\partial n}g(n,\nu;\beta), \tag{B.4}$$

derived from an identity

$$[\ln Z] = \lim_{n\to+0}\frac{\partial}{\partial n}\ln[Z^n]. \tag{B.5}$$

When (n,ν) are positive integers, we obtain

$$g(n,\nu;\beta) \;=\; -\frac{1}{M\beta}\ln\operatorname*{Tr}_{\{\boldsymbol{c}^a\}}\operatorname*{Tr}_{\{\boldsymbol{x}^{a\alpha}\}}\left(\left[\mathrm{e}^{-\frac{\beta}{2\nu}\sum_a\sum_\alpha(y_\mu-\sum_i A_{\mu i}c_i^a x_i^{a\alpha})^2}\right]_{\boldsymbol{y},\boldsymbol{A}}\right)^M, \tag{B.6}$$

where

$$\underset{\{\boldsymbol{c}^a\}}{\mathrm{Tr}} = \prod_{a=1}^{n} \sum_{\boldsymbol{c}^a} \delta\left(\sum_i c_i^a - Mr\right), \tag{B.7}$$

$$\underset{\{\boldsymbol{x}^{a\alpha}\}}{\mathrm{Tr}} = \prod_{a=1}^{n} \prod_{\alpha=1}^{\nu} \int \mathrm{d}_{\boldsymbol{c}^a} \boldsymbol{x}^{a\alpha}. \tag{B.8}$$

Let us introduce variables such as

$$s_\mu^{a\alpha} = \sum_i A_{\mu i} c_i^a x_i^{a\alpha}, \tag{B.9}$$

$$Q_{(a\alpha)(b\beta)} = \frac{1}{M} \sum_i (c_i^a x_i^{a\alpha})(c_i^b x_i^{b\beta}), \tag{B.10}$$

According to the central limit theorem, we regard the variables $\{\boldsymbol{s}^{a\alpha}\}$ as random variables which follow a zero-mean multivariate normal distribution and its covariances are given as follows:

$$[s_\mu^{a\alpha} s_{\mu'}^{b\beta}]_{\boldsymbol{A}} = \delta_{\mu\mu'} Q_{(a\alpha)(b\beta)}. \tag{B.11}$$

Using these variables, we obtain

$$\begin{aligned} & g(n, \nu; \beta) \\ = & -\frac{1}{M\beta} \ln \underset{\{\boldsymbol{c}^a\}}{\mathrm{Tr}} \underset{\{\boldsymbol{x}^{a\alpha}\}}{\mathrm{Tr}} \underset{\{Q_{(a\alpha)(b\beta)}\}}{\mathrm{Tr}} \left(\left[\mathrm{e}^{-\frac{\beta}{2\nu} \sum_a \sum_\alpha (y - s^{a\alpha})^2} \right]_{y, \{s^{a\alpha}\} | \{Q_{(a\alpha)(b\beta)}\}} \right)^M, \end{aligned} \tag{B.12}$$

where

$$\underset{\{Q_{(a\alpha)(b\beta)}\}}{\mathrm{Tr}} = \prod_{(a\alpha),(b\beta)} \int \mathrm{d}Q_{(a\alpha)(b\beta)} \delta\left(\sum_i (c_i^a x_i^{a\alpha})(c_i^b x_i^{b\beta}) - M Q_{(a\alpha)(b\beta)} \right). \tag{B.13}$$

After introducing the Fourier representation of the delta function, such as

$$\delta\left(\sum_i c_i^a - Mr\right) = \frac{1}{2\pi} \int \mathrm{d}\tilde{r}_a \mathrm{e}^{-\mathrm{i}\tilde{r}_a \left(\sum_i c_i^a - Mr\right)}, \tag{B.14}$$

the saddle-point method is employed to obtain

$$\begin{aligned} & \lim_{M \to +\infty} g(n, \nu; \beta) \\ = & \underset{\Theta}{\mathrm{extr}} \Bigg\{ -\frac{1}{\beta} \Bigg[\ln \left[\mathrm{e}^{-\frac{\beta}{2\nu} \sum_a \sum_\alpha (y - s^{a\alpha})^2} \right]_{y, \{s^{a\alpha}\} | \{Q_{(a\alpha)(b\beta)}\}} \\ & + \sum_a \mathrm{i}\tilde{r}_a r + \sum_{(a\alpha),(b\beta)} \mathrm{i}\tilde{Q}_{(a\alpha)(b\beta)} Q_{(a\alpha)(b\beta)} \\ & + \alpha \ln \sum_{\{c^a\}} \underset{\{x^{a\alpha}\}}{\mathrm{Tr}} \mathrm{e}^{-\sum_a \mathrm{i}\tilde{r}_a c^a - \sum_{(a\alpha)(b\beta)} \mathrm{i}\tilde{Q}_{(a\alpha)(b\beta)} (c^a x^{a\alpha})(c^b x^{b\beta})} \Bigg] \Bigg\}, \end{aligned} \tag{B.15}$$

where $\Theta = \{Q_{(a\alpha)(b\beta)}, \tilde{r}_a, \tilde{Q}_{(a\alpha)(b\beta)}\}$. Considering replica symmetry, the extremizer is assumed to be in the subspace parameterized by

$$(Q_{(a\alpha)(b\beta)}, \tilde{Q}_{(a\alpha)(b\beta)}) = \begin{cases} (Q, \tilde{Q}) & \text{if } a = b \wedge \alpha = \beta \\ (q_1, \tilde{q}_1) & \text{if } a = b \wedge \alpha \neq \beta \\ (q, \tilde{q}) & \text{if } a \neq b \end{cases}, \tag{B.16a}$$

$$\tilde{r}_a = \tilde{r}. \tag{B.16b}$$

If this is the case, we obtain

$$\begin{aligned} &\lim_{M\to+\infty} g(n,\nu;\beta) \\ = \ &\underset{\tilde{\Theta}}{\mathrm{extr}}\left\{ -\frac{1}{\beta}\left[\ln \int \mathrm{D}y\mathrm{D}w \left(\int \mathrm{D}v \left(\int \mathrm{D}u \mathrm{e}^{-\frac{\beta}{2\nu}(\sqrt{Q-q_1}u+\sqrt{q_1-q}v+\sqrt{q}w-\sigma_y y)^2} \right)^\nu \right)^n \right. \\ &+ni\tilde{r}r + n\nu \mathrm{i}\tilde{Q}Q + n\nu(\nu-1)\mathrm{i}\tilde{q}_1 q_1 + n(n-1)\nu^2 \mathrm{i}\tilde{q}q \\ &\left. +\alpha \ln \int \mathrm{D}z \left(\sum_c \mathrm{e}^{-\mathrm{i}\tilde{r}c} \int \mathrm{D}t \left(\underset{x}{\mathrm{Tr}}\, \mathrm{e}^{-\mathrm{i}(\tilde{Q}-\tilde{q}_1)cx^2 + t\sqrt{-2\mathrm{i}(\tilde{q}_1-\tilde{q})}cx + z\sqrt{-2\mathrm{i}\tilde{q}}cx} \right)^\nu \right)^n \right] \right\}, \end{aligned} \tag{B.17}$$

where $\tilde{\Theta} = \{Q, q_1, q, \tilde{r}, \tilde{Q}, \tilde{q}_1, \tilde{q}\}$.

We assume that Eq. (B.17) is true not only for positive integers (n, ν) but also for real numbers (n, ν). We define the following parameters

$$\chi_1 = \beta_1(Q - q_1), \tag{B.18a}$$

$$\hat{r} = \mathrm{i}\tilde{r}, \tag{B.18b}$$

$$\hat{Q} = \beta_1^{-1}\mathrm{i}(\tilde{Q} - \tilde{q}_1), \tag{B.18c}$$

$$\hat{\chi}_1 = \beta_1^{-2}\mathrm{i}(\tilde{q}_1 - \tilde{q}), \tag{B.18d}$$

$$\hat{q} = -\beta_1^{-2}\mathrm{i}\tilde{q}, \tag{B.18e}$$

and $\hat{\Theta} = \{Q, \chi_1, q, \hat{r}, \hat{Q}, \hat{\chi}_1, \hat{q}\}$ are assumed to be of the order $O(1)$. Taking the limits of $(n, \nu) \to (0, 0)$ gives us

$$\begin{aligned} &\lim_{M\to\infty} f(\beta) \\ = \ &\underset{\hat{\Theta}}{\mathrm{extr}}\left\{ -\frac{1}{\beta}\left[\frac{1}{2}\ln\frac{1+\chi_1}{1+\chi_1+\beta(Q-q)} - \frac{\beta}{2}\frac{q+\sigma_y^2}{1+\chi_1+\beta(Q-q)} \right.\right. \\ &+\hat{r}r + \beta(\hat{Q}Q - (\hat{\chi}_1+\hat{q})\chi_1) - \beta^2((\hat{\chi}_1+\hat{q})Q - \hat{q}q) \\ &\left.\left. -\alpha \int \mathrm{D}z \ln(1-\rho(z)) \right] \right\}, \end{aligned} \tag{B.19}$$

where

$$\rho(z) = \frac{1}{\sqrt{\frac{\hat{Q}-\beta\hat{\chi}_1}{\hat{Q}}}\exp\left[\hat{r} - \frac{\beta}{2}\frac{\hat{q}}{\hat{Q}-\beta\hat{\chi}_1}z^2\right] + 1}. \tag{B.20}$$

The extremization conditions with regard to $\hat{\Theta}$ lead to the equations of state

$$\hat{Q} = \frac{1}{2}\frac{1}{1+\chi_1}, \tag{B.21a}$$

$$\hat{\chi}_1 = \frac{1}{2}\frac{Q-q}{(1+\chi_1)(1+\chi_1+\beta(Q-q))}, \tag{B.21b}$$

$$\hat{q} = \frac{1}{2}\frac{q+\sigma_y^2}{(1+\chi_1+\beta(Q-q))^2}, \tag{B.21c}$$

$$r = \alpha\int \mathrm{D}z\rho(z), \tag{B.21d}$$

$$Q = \alpha\int \mathrm{D}z\rho(z)\left(\frac{1}{2}\frac{\hat{\chi}_1}{\hat{Q}(\hat{Q}-\beta\hat{\chi}_1)} + \frac{1}{2}\frac{\hat{q}}{(\hat{Q}-\beta\hat{\chi}_1)^2}z^2\right), \tag{B.21e}$$

$$\chi_1 = \alpha\int \mathrm{D}z\rho(z)\left(\frac{1}{2}\frac{1}{\hat{Q}}\right), \tag{B.21f}$$

$$q = \frac{\alpha}{\beta}\int \mathrm{D}z\rho(z)\left(\frac{1}{2}\frac{1}{\hat{Q}-\beta\hat{\chi}_1} - \frac{1}{2}\frac{\hat{Q}-\beta(\hat{\chi}_1+\hat{q})}{(\hat{Q}-\beta\hat{\chi}_1)^2}z^2\right). \tag{B.21g}$$

Using the extremizer of the right-hand side of Eq. (B.19) and the equations of state,

Eqs. (B.21), the distortion and the entropy density are calculated as follows:

$$\lim_{M\to+\infty}\epsilon(\beta) = \lim_{M\to+\infty}\frac{\partial}{\partial\beta}(\beta f(\beta)) \tag{B.22}$$

$$\begin{aligned} &= \frac{1}{2}\frac{Q+\sigma_y^2}{1+\chi_1+\beta(Q-q)} - \frac{\beta}{2}\frac{(q+\sigma_y^2)(Q-q)}{(1+\chi_1+\beta(Q-q))^2} \\ &\quad -(\hat{Q}Q-(\hat{\chi}_1+\hat{q})\chi_1) + 2\beta((\hat{\chi}_1+\hat{q})Q-\hat{q}q) \\ &\quad -\alpha\int \mathrm{D}z\rho(z)\left(\frac{1}{2}\frac{\hat{\chi}_1}{\hat{Q}-\beta\hat{\chi}_1}+\frac{1}{2}\frac{\hat{Q}\hat{q}}{(\hat{Q}-\beta\hat{\chi}_1)^2}z^2\right) \end{aligned} \tag{B.23}$$

$$= \hat{\chi}_1+\hat{q}, \tag{B.24}$$

$$\lim_{M\to+\infty}s(\beta) = \lim_{M\to+\infty}\beta(\epsilon(\beta)-f(\beta)) \tag{B.25}$$

$$\begin{aligned} &= \frac{1}{2}\ln\frac{1+\chi_1}{1+\chi_1+\beta(Q-q)} + \frac{1}{2}\frac{\beta(Q-q)}{1+\chi_1+\beta(Q-q)} - \frac{\beta}{2}\frac{\beta(Q-q)(q+\sigma_y^2)}{(1+\chi_1+\beta(Q-q))^2} \\ &\quad +\hat{r}r+\beta^2((\hat{\chi}_1+\hat{q})Q)-\hat{q}q) \\ &\quad -\alpha\int \mathrm{D}z\rho(z)\left(\frac{1}{2}\frac{\hat{\chi}_1}{\hat{Q}-\beta\hat{\chi}_1}+\frac{1}{2}\frac{\hat{Q}\hat{q}}{(\hat{Q}-\beta\hat{\chi}_1)^2}z^2\right) - \alpha\int \mathrm{D}z\ln(1-\rho(z)). \end{aligned} \tag{B.26}$$

In the limit of $\beta\to 0$, the equations of state (B.21) are solved analytically to obtain

$$\lim_{M\to+\infty}\epsilon(\beta\to 0) = \frac{1-r}{2}\sigma_y^2, \tag{B.27}$$

which corresponds to the value of distortion achieved by the random method.

B.2 Performance of the l_1-norm regularization approach

B.2.1 Statistical-mechanical representation

We explain the performance analysis of the l_1-norm regularization approach in detail. We use some methods of statistical mechanics as well as the entropy analysis of the overcomplete-basis strategy. The l_1-norm regularization is represented by a Hamiltonian

$$\mathcal{H}_1(\boldsymbol{\gamma};\lambda) = \frac{1}{2}||\boldsymbol{y}-\boldsymbol{A}\boldsymbol{\gamma}||_2^2+\lambda||\boldsymbol{\gamma}||_1. \tag{B.28}$$

This Hamiltonian is equal to the cost function of LASSO, Eq. (5.22). The corresponding canonical distribution is given by

$$p_1(\boldsymbol{\gamma}|\beta,\lambda) = \frac{1}{Z_1(\beta,\lambda)}\mathrm{e}^{-\beta\mathcal{H}_1(\boldsymbol{\gamma};\lambda)}. \tag{B.29}$$

The parameter β plays a role of inverse temperature. The normalization factor Z_1 is called a partition function defined as

$$Z_1(\beta, \lambda) = \int \mathrm{d}\boldsymbol{\gamma} \mathrm{e}^{-\beta \mathcal{H}_1(\boldsymbol{\gamma}; \lambda)}. \tag{B.30}$$

The typical value of compression rate determined by the l_1-norm regularization is expressed as

$$r_1(\lambda) = \lim_{\beta \to +\infty} \frac{1}{M} \left[\langle ||\boldsymbol{\gamma}||_0 \rangle_{\gamma|\beta,\lambda} \right]_{\boldsymbol{y},\boldsymbol{A}}. \tag{B.31}$$

The compression rate is also expressed as

$$r_1(\lambda) \;\; = \;\; \lim_{\kappa \to 0} \frac{\partial}{\partial \kappa} f_1(\beta, \kappa, \lambda), \tag{B.32}$$

using a free-energy density defined by

$$f_1(\lambda, \kappa) = \lim_{\beta \to +\infty} -\frac{1}{M\beta} \left[\ln \int \mathrm{d}\boldsymbol{\gamma} \mathrm{e}^{-\beta \mathcal{H}_1(\boldsymbol{\gamma}) - \beta\kappa ||\boldsymbol{\gamma}||_0} \right]_{\boldsymbol{y},\boldsymbol{A}}. \tag{B.33}$$

The typical value of distortion obtained by the l_1-norm regularization is expressed as

$$\epsilon_{\mathrm{LASSO}}(\lambda) = \lim_{\beta \to +\infty} \frac{1}{M} \left[\left\langle \frac{1}{2} ||\boldsymbol{y} - \boldsymbol{A}\boldsymbol{\gamma}||_2^2 \right\rangle_{\gamma|\beta,\lambda} \right]_{\boldsymbol{y},\boldsymbol{A}} \tag{B.34}$$

The distortion is also expressed as

$$\epsilon_{\mathrm{LASSO}}(\lambda) = \lim_{\beta \to +\infty} \left(\frac{\partial}{\partial \beta} \beta - \lambda \frac{\partial}{\partial \lambda} \right) f_1(\lambda, 0) \tag{B.35}$$

After the method of least squares is used, the compression rate does not change, but the distortion is expected to improve. This distortion value is expressed as

$$\epsilon_1(\lambda) = \lim_{\beta \to +\infty} \lim_{\beta_1 \to +\infty} \frac{1}{M} \left[\langle \mathcal{H}_{\mathrm{ls}}(|\boldsymbol{\gamma}|_0; \beta_1) \rangle_{\gamma|\beta} \right]_{\boldsymbol{y},\boldsymbol{A}}, \tag{B.36}$$

where $|\cdot|_0$ of a vector is defined by $(|\boldsymbol{v}|_0)_i = |v_i|_0$, and $|v_i|_0 = 0$ ($v_i = 0$) or 1 ($v_i \neq 0$).

B.2.2 Before the method of least squares

We define a function

$$g_{\mathrm{LASSO}}(n; \beta, \kappa) = -\frac{1}{M\beta} \ln \left[\left(\int \mathrm{d}\boldsymbol{\gamma} \mathrm{e}^{-\beta \mathcal{H}_1(\boldsymbol{\gamma}) - \beta\kappa ||\boldsymbol{\gamma}||_0} \right)^n \right]_{\boldsymbol{y},\boldsymbol{A}}, \tag{B.37}$$

to express the free-energy density as

$$f_1(\lambda,\kappa) = \lim_{\beta\to+\infty}\lim_{n\to 0}\frac{\partial}{\partial n} g_{\rm LASSO}(n;\beta,\kappa), \tag{B.38}$$

derived from an identity

$$[\ln Z] = \lim_{n\to+0}\frac{\partial}{\partial n}\ln[Z^n]. \tag{B.39}$$

When (n,ν) are positive integers, we obtain

$$g_{\rm LASSO}(n;\beta,\kappa) = -\frac{1}{M\beta}\ln \mathop{\rm Tr}_{\{\boldsymbol{\gamma}^a\}}\left(\left[{\rm e}^{-\frac{\beta}{2}\sum_a (y_\mu-\sum_i A_{\mu i}\gamma_i^a)^2}\right]_{\boldsymbol{y},\boldsymbol{A}}\right)^M, \tag{B.40}$$

where

$$\mathop{\rm Tr}_{\{\boldsymbol{\gamma}^a\}} = \prod_{a=1}^n \int {\rm d}\boldsymbol{\gamma}^a {\rm e}^{-\beta\lambda\sum_i|\gamma_i^a|-\beta\kappa\sum_i|\gamma_i^a|_0}. \tag{B.41}$$

Let us introduce variables such as

$$s_\mu^a = \sum_i A_{\mu i}\gamma_i^a, \tag{B.42}$$

$$P_{ab} = \frac{1}{M}\sum_i \xi_i^a\xi_i^b. \tag{B.43}$$

According to the central limit theorem, we regard the variables $\{\boldsymbol{s}^a\}$ as random variables which follow a zero-mean multivariate normal distribution and its covariances are given as follows: $[s_\mu^a s_{\mu'}^b]_{\boldsymbol{A}} = \delta_{\mu\mu'}P_{ab}$. Using these variables, we obtain

$$g_{\rm LASSO}(n;\beta,\kappa) = -\frac{1}{M\beta}\ln \mathop{\rm Tr}_{\{\boldsymbol{\gamma}^a\}}\mathop{\rm Tr}_{\{P_{ab}\}}\left(\left[{\rm e}^{-\frac{\beta}{2}\sum_a (y-s^a)^2}\right]_{y,\{s^a\}|\{P_{ab}\}}\right)^M, \tag{B.44}$$

where

$$\mathop{\rm Tr}_{\{P_{ab}\}} = \prod_{a,b}\int {\rm d}P_{ab}\delta\left(\sum_i \gamma_i^a\gamma_i^b - MP_{ab}\right). \tag{B.45}$$

After introducing the Fourier representation of the delta function, such as

$$\delta\left(\sum_i \gamma_i^a\gamma_i^b - MP_{ab}\right) = \frac{1}{2\pi}\int {\rm d}\tilde{P}_{ab}{\rm e}^{-{\rm i}\tilde{P}_{ab}\left(\sum_i\gamma_i^a\gamma_i^b - MP_{ab}\right)}, \tag{B.46}$$

the saddle-point method is employed to obtain

$$\begin{aligned}
&\lim_{M\to+\infty} g_{\mathrm{LASSO}}(n;\beta,\kappa) \\
=\ &\operatorname*{extr}_{\Theta_{\mathrm{LASSO}}}\left\{-\frac{1}{\beta}\left[\ln\left[\mathrm{e}^{-\frac{\beta}{2}\sum_a (y-s^a)^2}\right]_{y,\{s^a\}|\{P_{ab}\}}\right.\right. \\
&+\sum_{a,b}\mathrm{i}\tilde{P}_{ab}P_{ab} \\
&\left.\left.+\alpha\ln\operatorname*{Tr}_{\{\gamma^a\}}\mathrm{e}^{-\sum_{a,b}\mathrm{i}\tilde{P}_{ab}\gamma^a\gamma^b}\right]\right\}
\end{aligned} \tag{B.47}$$

where $\Theta_{\mathrm{LASSO}} = \{P_{ab}, \tilde{P}_{ab}\}$. Considering replica symmetry, the extremizer is assumed to be in the subspace parametrized by

$$(P_{ab}, \tilde{P}_{ab}) = \begin{cases} (P, \tilde{P}) & \text{if } a = b \\ (p, \tilde{p}) & \text{if } a \neq b \end{cases}. \tag{B.48}$$

If this is the case, we obtain

$$\begin{aligned}
&\lim_{M\to+\infty} g_{\mathrm{LASSO}}(n;\beta,\kappa) \\
=\ &\operatorname*{extr}_{\tilde{\Theta}_{\mathrm{LASSO}}}\left\{-\frac{1}{\beta}\left[\ln\int \mathrm{D}y\mathrm{D}w\left(\int \mathrm{D}v\mathrm{e}^{-\frac{\beta}{2}(\sqrt{P-p}v+\sqrt{p}w-\sigma_y y)^2}\right)^n\right]\right\} \\
&+n\mathrm{i}\tilde{P}P + n(n-1)\mathrm{i}\tilde{p}p \\
&+\alpha\ln\int \mathrm{D}z\left(\operatorname*{Tr}_{\gamma}\mathrm{e}^{-\mathrm{i}(\tilde{P}-\tilde{p})\gamma^2+z\sqrt{-2\mathrm{i}\tilde{p}}\gamma}\right)^n\Bigg]\Bigg\}
\end{aligned} \tag{B.49}$$

where $\tilde{\Theta}_{\mathrm{LASSO}} = \{P, p, \tilde{P}, \tilde{p}\}$.

We assume that Eq. (B.49) is true not only for positive integers n but also for real numbers n. We define the following parameters

$$\chi_p = \beta(P-p), \tag{B.50a}$$
$$\hat{P} = \beta^{-1}\mathrm{i}(\tilde{P}-\tilde{p}), \tag{B.50b}$$
$$\hat{\chi}_p = -\beta^{-2}\mathrm{i}\tilde{p}, \tag{B.50c}$$

and $\hat{\Theta}_{\mathrm{LASSO}} = \{P, \chi_p, \hat{P}, \hat{\chi}_p\}$ are assumed to be of the order $O(1)$. Taking the limit of

$n \to 0$ gives us

$$\begin{aligned}
&\lim_{M\to+\infty} f_1(\lambda,\kappa) \\
= &\operatorname*{extr}_{\hat{\Theta}_{\mathrm{LASSO}}} \left\{ \frac{1}{2}\frac{P+\sigma_y^2}{1+\chi_p} \right. \\
&-\hat{P}P + \hat{\chi}_p\chi_p \\
&\left. -\alpha\frac{\hat{\chi}_p}{2\hat{P}}\left((1+2\theta_+\theta_-)\mathrm{erfc}(\theta_+) - \theta_-\frac{2}{\sqrt{\pi}}\mathrm{e}^{-\theta_+^2}\right)\right\},
\end{aligned} \tag{B.51}$$

where $\hat{\Theta}_{\mathrm{LASSO}} = \{P, \chi_p, \hat{P}, \hat{\chi}_p\}, \theta_\pm = \frac{\lambda \pm \sqrt{4\kappa\hat{P}}}{\sqrt{4\hat{\chi}_p}}$ and $\mathrm{erfc}(\cdot)$ is the complementary error function defined as

$$\mathrm{erfc}(x) = \frac{2}{\sqrt{\pi}}\int_x^{+\infty} \mathrm{d}t\mathrm{e}^{-t^2}. \tag{B.52}$$

Taking the limit of $\kappa \to 0$, the extremization conditions with regard to $\hat{\Theta}_{\mathrm{LASSO}}$ lead to the equations of state

$$\hat{P} = \frac{1}{2}\frac{1}{1+\chi_p}, \tag{B.53a}$$

$$\hat{\chi}_p = \frac{1}{2}\frac{P+\sigma_y^2}{(1+\chi_p)^2}, \tag{B.53b}$$

$$P = \alpha\frac{\hat{\chi}_p}{2\hat{P}^2}\left((1+2\theta^2)\mathrm{erfc}(\theta) - \theta\frac{2}{\sqrt{\pi}}\mathrm{e}^{-\theta^2}\right), \tag{B.53c}$$

$$\chi_p = \alpha\frac{1}{2\hat{P}}\mathrm{erfc}(\theta), \tag{B.53d}$$

where $\theta = \frac{\lambda}{\sqrt{4\hat{\chi}_p}}$.

Using the solution of the equations of state, Eqs. (B.53), the compression rate and the distortion are calculated as follows:

$$\lim_{M\to+\infty} r_1(\lambda) = \alpha\mathrm{erfc}(\theta) \tag{B.54}$$

$$\lim_{M\to+\infty} \epsilon_{\mathrm{LASSO}}(\lambda) = \hat{\chi}_p \tag{B.55}$$

B.2.3 After the method of least squares

We define a function

$$g_1(n,\nu;\beta,\beta_1,\lambda) = -\frac{1}{M\beta_1}\ln\left[(Z_1(\beta,\lambda))^{n-1}\int \mathrm{d}\boldsymbol{\gamma}\mathrm{e}^{-\beta\mathcal{H}_1(\boldsymbol{\gamma};\lambda)}(\mathcal{Z}_1(\boldsymbol{\gamma};\beta_1))^\nu\right]_{\boldsymbol{y},\boldsymbol{A}} \tag{B.56}$$

where

$$\mathcal{Z}_1(\boldsymbol{\gamma};\beta_1) = \mathrm{e}^{-\beta_1 \mathcal{H}_{\mathrm{ls}}(|\boldsymbol{\gamma}|_0,\beta_1)}. \tag{B.57}$$

Then, the distortion is expressed as

$$\epsilon_1(\lambda) = \lim_{\beta\to+\infty}\lim_{\beta_1\to+\infty}\lim_{n\to 0}\lim_{\nu\to 0}\frac{\partial}{\partial\nu}g_1(n,\nu,\beta,\beta_1,\lambda) \tag{B.58}$$

When (n,ν) are positive integers, we obtain

$$\begin{aligned} & g_1(n,\nu;\beta,\beta_1,\lambda) \\ = \; & -\frac{1}{M\beta_1}\ln \operatorname*{Tr}_{\{\boldsymbol{\gamma}^a\}}\operatorname*{Tr}_{\{\boldsymbol{x}^\alpha\}}\left(\left[\mathrm{e}^{-\frac{\beta}{2}\sum_a(y_\mu-\sum_i A_{\mu i}\gamma_i^a)^2-\frac{\beta_1}{2}\sum_\alpha(y_\mu-\sum_i A_{\mu i}|\gamma_i^1|_0 x_i^\alpha)^2}\right]_{\boldsymbol{y},\boldsymbol{A}}\right)^M, \end{aligned} \tag{B.59}$$

where

$$\operatorname*{Tr}_{\{\boldsymbol{\gamma}^a\}} = \prod_{a=1}^{n}\int \mathrm{d}\boldsymbol{\gamma}^a \mathrm{e}^{-\beta\lambda\sum_i|\gamma_i^a|}, \tag{B.60a}$$

$$\operatorname*{Tr}_{\{\boldsymbol{x}^\alpha\}} = \prod_{\alpha=1}^{\nu}\int \mathrm{d}_{|\boldsymbol{\xi}^1|_0}\boldsymbol{x}^\alpha. \tag{B.60b}$$

Let us introduce variables such as

$$s_\mu^a = \sum_i A_{\mu i}\gamma_i^a, \tag{B.61a}$$

$$t_\mu^\alpha = \sum_i A_{\mu i}|\gamma_i^1|_0 x_i^\alpha, \tag{B.61b}$$

and

$$P_{ab} = \frac{1}{M}\sum_i \gamma_i^a\gamma_i^b, \tag{B.62a}$$

$$C_{\alpha b} = \frac{1}{M}\sum_i (|\gamma_i^1|_0 x_i^\alpha)\gamma_i^b, \tag{B.62b}$$

$$D_{a\beta} = \frac{1}{M}\sum_i \gamma_i^a(|\gamma_i^1|_0 x_i^\beta), \tag{B.62c}$$

$$Q_{\alpha\beta} = \frac{1}{M}\sum_i (|\gamma_i^1|_0 x_i^\alpha)(|\gamma_i^1|_0 x_i^\beta). \tag{B.62d}$$

According to the central limit theorem, we regard the variables $\{\boldsymbol{s}^a,\boldsymbol{t}^\alpha\}$ as random variables which follow a zero-mean multivariate normal distribution and its covariances

are given as follows:

$$\left[s_\mu^a s_{\mu'}^b\right]_{\boldsymbol{A}} = \delta_{\mu\mu'} P_{ab}, \tag{B.63a}$$

$$\left[t_\mu^\alpha s_{\mu'}^b\right]_{\boldsymbol{A}} = \delta_{\mu\mu'} C_{\alpha b}, \tag{B.63b}$$

$$\left[s_\mu^a t_{\mu'}^\beta\right]_{\boldsymbol{A}} = \delta_{\mu\mu'} D_{a\beta}, \tag{B.63c}$$

$$\left[t_\mu^\alpha t_\mu^\beta\right]_{\boldsymbol{A}} = \delta_{\mu\mu'} Q_{\alpha\beta}. \tag{B.63d}$$

Using these variables, we obtain

$$\begin{aligned} & g_1(n,\nu;\beta,\beta_1) \\ = & -\frac{1}{M\beta_1} \ln \operatorname*{Tr}_{\{\boldsymbol{\gamma}^a\}} \operatorname*{Tr}_{\{\boldsymbol{x}^\alpha\}} \operatorname*{Tr}_{\{P_{ab},C_{\alpha b},D_{a\beta},Q_{\alpha\beta}\}} \\ & \left(\left[\mathrm{e}^{-\frac{\beta}{2}\sum_a (y-s^a)^2 - \frac{\beta_1}{2}\sum_\alpha (y-t^\alpha)^2} \right]_{y,\{s^a,t^\alpha\}|\{P_{ab},C_{\alpha b},D_{a\beta},Q_{\alpha\beta}\}} \right)^M, \end{aligned} \tag{B.64}$$

where

$$\begin{aligned} \operatorname*{Tr}_{\{P_{ab},C_{\alpha b},D_{a\beta},Q_{\alpha\beta}\}} = & \prod_{a,b} \int \mathrm{d}P_{ab} \delta\left(\sum_i \gamma_i^a \gamma_i^b - M P_{ab} \right) \\ & \prod_{\alpha,b} \int \mathrm{d}C_{\alpha b} \delta\left(\sum_i (|\gamma_i^1|_0 x_i^\alpha) \gamma_i^b - M C_{\alpha b} \right) \\ & \prod_{a,\beta} \int \mathrm{d}D_{a\beta} \delta\left(\sum_i \gamma_i^a (|\gamma_i^1|_0 x_i^\beta) - M D_{a\beta} \right) \\ & \prod_{\alpha,\beta} \int \mathrm{d}Q_{\alpha\beta} \delta\left(\sum_i (|\gamma_i^1|_0 x_i^\alpha)(|\gamma_i^1|_0 x_i^\beta) - M Q_{\alpha\beta} \right). \end{aligned} \tag{B.65}$$

After introducing the Fourier representation of the delta function, such as

$$\delta\left(\sum_i (|\gamma_i^1|_0 x_i^\alpha)(|\gamma_i^1|_0 x_i^\beta) - M Q_{\alpha\beta} \right) = \frac{1}{2\pi} \int \mathrm{d}\tilde{Q}_{\alpha\beta} \mathrm{e}^{-\mathrm{i}\tilde{Q}_{\alpha\beta}\left(\sum_i (|\gamma_i^1|_0 x_i^\alpha)(|\gamma_i^1|_0 x_i^\beta) - M Q_{\alpha\beta}\right)}, \tag{B.66}$$

the saddle-point method is employed, to obtain

$$
\begin{aligned}
& g_1(n,\nu,\beta,\beta_1) \\
= & \operatorname*{extr}_{\Theta_1}\Bigg\{ -\frac{1}{\beta_1}\Bigg[\ln\left[\mathrm{e}^{-\frac{\beta}{2}\sum_a (y-s^a)^2 - \frac{\beta_1}{2}\sum_\alpha (y-s^\alpha)^2} \right]_{y,\{s^a,t^\alpha\}|\{P_{ab},C_{\alpha b},D_{a\beta},Q_{\alpha\beta}\}} \\
& + \sum_{a,b} \mathrm{i}\tilde{P}_{ab}P_{ab} + \sum_{\alpha b} \mathrm{i}\tilde{C}_{\alpha b}C_{\alpha b} + \sum_{a\beta} \mathrm{i}\tilde{D}_{a\beta}D_{a\beta} + \sum_{\alpha\beta} \mathrm{i}\tilde{Q}_{\alpha\beta}Q_{\alpha\beta} \\
& + \alpha \ln \operatorname*{Tr}_{\{\gamma^a\}} \operatorname*{Tr}_{\{x^\alpha\}} \mathrm{e}^{-\sum_{a,b}\mathrm{i}\tilde{P}_{ab}\gamma^a\gamma^b - \sum_{\alpha,b}(|\gamma^1|_0 x^\alpha)\gamma^b - \sum_{a\beta}\gamma^a(|\gamma^1|_0 x^\beta) - \sum_{\alpha\beta}(|\gamma^1|_0 x^\alpha)(|\gamma^1|_0 x^\beta)} \Bigg] \Bigg\},
\end{aligned}
\tag{B.67}
$$

where $\Theta_1 = \{C_{\alpha b}, D_{a\beta}, Q_{\alpha\beta}, \tilde{C}_{\alpha b}, \tilde{D}_{a\beta}, \tilde{Q}_{\alpha\beta}\}$. For $\Theta_{\mathrm{LASSO}} = \{P_{ab}, \tilde{P}_{ab}\}$, we substitute the extremizer of the right-hand side of Eq. (B.47). Considering replica symmetry, the extremizer is assumed to be in the subspace parametrized by

$$
(C_{\alpha b}, \tilde{C}_{\alpha b}) = \begin{cases} (C, \tilde{C}) & \text{if } a = 1 \\ (c, \tilde{c}) & \text{if } a \neq 1 \end{cases}, \tag{B.68}
$$

$$
(D_{a\beta}, \tilde{D}_{a\beta}) = \begin{cases} (C, \tilde{C}) & \text{if } a = 1 \\ (c, \tilde{c}) & \text{if } a \neq 1 \end{cases}, \tag{B.69}
$$

$$
(Q_{\alpha\beta}, \tilde{Q}_{\alpha\beta}) = \begin{cases} (Q, \tilde{Q}) & \text{if } \alpha = \beta \\ (q, \tilde{q}) & \text{if } \alpha \neq \beta \end{cases}. \tag{B.70}
$$

If this is the case, we obtain

$$
\begin{aligned}
& \lim_{M\to+\infty} g_1(n,\nu;\beta,\beta_1) \\
= & \operatorname*{extr}_{\tilde{\Theta}_1}\Bigg\{ -\frac{1}{\beta_1}\Bigg[\ln \int \mathrm{D}y\mathrm{D}z\mathrm{D}w \left(\int \mathrm{D}v \mathrm{e}^{-\frac{\beta}{2}(\sqrt{P-p}v + \sqrt{p}w - \sigma_y y)^2} \right)^{n-1} \\
& \int \mathrm{D}v \mathrm{e}^{-\frac{\beta}{2}(\sqrt{P-p}v + \sqrt{p}w - \sigma_y y)^2} \\
& \left(\int \mathrm{D}u \mathrm{e}^{-\frac{\beta_1}{2}(\sqrt{Q-q}u + \sqrt{q - \frac{(C-c)^2}{P-p} - \frac{c^2}{p}}z + \frac{C-c}{\sqrt{P-p}}v + \frac{c}{\sqrt{p}}w - \sigma_y y)^2} \right)^{\nu} \\
& n\mathrm{i}\tilde{P}P + n(n-1)\mathrm{i}\tilde{p}p + 2\nu\mathrm{i}\tilde{C}C + 2(n-1)\nu\mathrm{i}\tilde{c}c + \nu\mathrm{i}\tilde{Q}Q + \nu(\nu-1)\mathrm{i}\tilde{q}q \\
& + \alpha \ln \int \mathrm{D}z\mathrm{D}w\mathrm{D}v\mathrm{D}u \left(\operatorname*{Tr}_{\gamma} \mathrm{e}^{-\mathrm{i}(\tilde{P}-\tilde{p})\gamma^2 + (u\sqrt{-2\mathrm{i}(\tilde{p}-\tilde{c})} + v\sqrt{-2\mathrm{i}\tilde{c}})\gamma} \right)^{n-1} \\
& \operatorname*{Tr}_{\gamma} \mathrm{e}^{-\mathrm{i}((\tilde{P}-\tilde{p})-(\tilde{C}-\tilde{c}))\gamma^2 + (u\sqrt{-2\mathrm{i}(\tilde{p}-\tilde{c})} + w\sqrt{-2\mathrm{i}(\tilde{C}-\tilde{c})} + v\sqrt{-2\mathrm{i}\tilde{c}})\gamma} \\
& \left(\operatorname*{Tr}_{x} \mathrm{e}^{-\mathrm{i}((\tilde{Q}-\tilde{q})-(\tilde{C}-\tilde{c}))(|\gamma|_0 x)^2 + (z\sqrt{-2\mathrm{i}(\tilde{q}-\tilde{c})} + w\sqrt{-2\mathrm{i}(\tilde{C}-\tilde{c})} + v\sqrt{-2\mathrm{i}\tilde{c}})|\gamma|_0 x} \right)^{\nu} \Bigg] \Bigg\}.
\end{aligned}
\tag{B.71}
$$

where $\tilde{\Theta}_1 = \{C, c, Q, q, \tilde{C}, \tilde{c}, \tilde{Q}, \tilde{q}\}$. The set of parameters $\tilde{\Theta}_{\text{LASSO}} = \{P, p, \tilde{P}, \tilde{p}\}$ corresponds to the extremizer of the right-hand side of Eq. (B.49).

We assume that Eq. (B.71) is true not only for positive integers (n, ν) but also for real numbers (n, ν). We define the following parameters

$$\chi_c = \beta(C - c) \tag{B.72a}$$
$$\chi_q = \beta(Q - q) \tag{B.72b}$$
$$\hat{C} = \beta^{-1}\mathrm{i}(\tilde{C} + \tilde{c}) \tag{B.72c}$$
$$\hat{\chi}_c = -\beta^{-2}\mathrm{i}\tilde{c} \tag{B.72d}$$
$$\hat{Q} = \beta^{-1}\mathrm{i}(\tilde{Q} - \tilde{q}) \tag{B.72e}$$
$$\hat{\chi}_q = -\beta^{-2}\mathrm{i}\tilde{q} \tag{B.72f}$$

and $\hat{\Theta}_1 = \{C, \chi_c, Q, \chi_q, \hat{C}, \hat{\chi}_c, \hat{Q}, \hat{\chi}_q\}$ are assumed to be of the order $O(1)$. Taking the limits of $(n, \nu) \to (0, 0)$ and $\beta = \beta_1 \to +\infty$ gives us

$$\begin{aligned}
&\lim_{M\to+\infty} \epsilon_1(\lambda) \\
= \ &\operatorname*{extr}_{\hat{\Theta}_1} \Bigg\{ \frac{1}{2}\left(\frac{\chi_c}{1+\chi_p}\right)^2 \frac{P+\sigma_y^2}{1+\chi_q} - \frac{\chi_c}{1+\chi_p}\frac{C+\sigma_y^2}{1+\chi_q} + \frac{1}{2}\frac{Q+\sigma_y^2}{1+\chi_q} \\
&-(\hat{Q}Q - \hat{\chi}_q\chi_q) + 2(\hat{C}C + \hat{\chi}_c\chi_c) \\
&-\alpha\frac{\hat{\chi}_p}{2\hat{Q}}\Bigg(\left(\frac{\hat{\chi}_q}{\hat{\chi}_p} + 2\frac{\hat{\chi}_c}{\hat{\chi}_p}\frac{\hat{C}}{\hat{P}} + (1+2\theta^2)\frac{\hat{C}^2}{\hat{P}^2}\right)\operatorname{erfc}(\theta) \\
&+\theta\left(\frac{\hat{\chi}_c^2}{\hat{\chi}_p^2} - \frac{\hat{C}^2}{\hat{P}^2}\right)\frac{2}{\sqrt{\pi}}\mathrm{e}^{-\theta^2}\Bigg)\Bigg\},
\end{aligned} \tag{B.73}$$

where $\hat{\Theta}_1 = \{C, \chi_c, Q, \chi_c, \hat{C}, \hat{\chi}_c, \hat{Q}, \hat{\chi}_c\}$, $\theta = \frac{\lambda}{\sqrt{4\hat{\chi}_p}}$ and $\operatorname{erfc}(\cdot)$ is the complementary error function. The set of parameters $\tilde{\Theta}_{\text{LASSO}} = \{P, \chi_p, \hat{P}, \hat{\chi}_p\}$ corresponds to the extremizer of the right-hand side of Eq. (B.51). The extremization conditions with regard to $\hat{\Theta}_1$ lead

to the equations of state

$$\hat{C} = \frac{1}{2}\frac{\chi_c}{1+\chi_p}\frac{1}{1+\chi_q}, \tag{B.74a}$$

$$\hat{\chi}_c = -\frac{1}{2}\frac{\chi_c}{(1+\chi_p)^2}\frac{P+\sigma_y^2}{1+\chi_q} + \frac{1}{2}\frac{1}{1+\chi_p}\frac{C+\sigma_y^2}{1+\chi_q}, \tag{B.74b}$$

$$\hat{Q} = \frac{1}{2}\frac{1}{1+\chi_q}, \tag{B.74c}$$

$$\hat{\chi}_q = \frac{1}{2}\left(\frac{\chi_c}{1+\chi_p}\right)^2\frac{P+\sigma_y^2}{(1+\chi_q)^2} - \frac{\chi_c}{1+\chi_p}\frac{C+\sigma_y^2}{(1+\chi_q)^2} + \frac{1}{2}\frac{Q+\sigma_y^2}{(1+\chi_q)^2}, \tag{B.74d}$$

$$C = \alpha\frac{\hat{\chi}_p}{2\hat{P}\hat{Q}}\left(\left(\frac{\hat{\chi}_c}{\hat{\chi}_p} + (1+2\theta^2)\frac{\hat{C}}{\hat{P}}\right)\mathrm{erfc}(\theta) - \frac{\hat{C}}{\hat{P}}\theta\frac{2}{\sqrt{\pi}}\mathrm{e}^{-\theta^2}\right), \tag{B.74e}$$

$$\chi_c = \alpha\frac{1}{2\hat{Q}}\left(\frac{\hat{C}}{\hat{P}}\mathrm{erfc}(\theta) + \frac{\hat{\chi}_c}{\hat{\chi}_p}\theta\frac{2}{\sqrt{\pi}}\mathrm{e}^{-\theta^2}\right), \tag{B.74f}$$

$$Q = \alpha\frac{\hat{\chi}_p}{2\hat{Q}^2}\left(\left(\frac{\hat{\chi}_q}{\hat{\chi}_p} + 2\frac{\hat{\chi}_c}{\hat{\chi}_p}\frac{\hat{C}}{\hat{P}} + (1+2\theta^2)\frac{\hat{C}^2}{\hat{P}^2}\right)\mathrm{erfc}(\theta) + \left(\frac{\hat{\chi}_c^2}{\hat{\chi}_p^2} - \frac{\hat{C}^2}{\hat{P}^2}\right)\theta\frac{2}{\sqrt{\pi}}\mathrm{e}^{-\theta^2}\right), \tag{B.74g}$$

$$\chi_q = \alpha\frac{1}{2\hat{Q}}\mathrm{erfc}(\theta) \tag{B.74h}$$

Bibliography

[1] Aki, K. and Lee, W. H. K., *Journal of Geophysical Research*, **81**(23), 4381–4399 (1976).

[2] Alpichshev, Z., Analytis, J. G., Chu, J.-H., Fisher, I. R., Chen, Y. L., Shen, Z. X., Fang, A., and Kapitulnik, A., *Physical Review Letters*, **104**(1), 016401-1–016401-4 (2010).

[3] Attias, H., in *Proceedings of the Fifteenth Conference on Uncertainty in Artificial Intelligence*, 21–30 (1999).

[4] Bally, J., *Nature*, **524**, 301–302 (2015).

[5] Binnig, G. and Rohrer, H., *Review of Modern Physics*, **59**(3), 615–625 (1987).

[6] Binnig, G., Rohrer, H., Gerber Ch., and Weibel, E., *Physical Review Letters*, **49**(1), 57–60 (1982).

[7] Binnig, G., Rohrer, H., Gerber, Ch., and Weibel, E., *Physical Review Letters*, **50**(2), 120–123 (1983).

[8] Binnig, G., Quate, C. F., and Gerber, Ch., *Physical Review Letters*, **56**(9), 930–933 (1986).

[9] Bishop, C. M., *Pattern Recognition and Machine Learning*, Springer, New York (2006).

[10] Bloomfield, B. and Steiger, W. L., *Least Absolute Deviations*, Birkhäuser, Boston (1983).

[11] Cai, T. T., Wang, L., and Xu, G., *IEEE Transactions on Signal Processing*, **58**(10), 1300–1308 (2010).

[12] Cai, T. T., Wang, L., and Xu, G., *IEEE Transactions on Information Theory*, **56**(9), 4388–4394 (2010).

[13] Candès, E. J., *Comptes Rendus Mathématique*, **346**(9–10), 589–592 (2008).

[14] Candès, E. J., Romberg, J., and Tao, T., *IEEE Transactions on Information Theory*, **52**(2), 489–509 (2006).

[15] Candès, E. J., Romberg, J., and Tao, T., *Communications on Pure and Applied Mathematics*, **59**(8), 1207–1223 (2006).

[16] Candès, E. J. and Tao, T., *IEEE Transactions on Information Theory*, **51**(12), 4203–4215 (2005).

[17] Candès, E. J. and Tao, T., *IEEE Transactions on Information Theory*, **52**(12), 5406–5425 (2006).

[18] Chen, S. and Donoho, D., in *1994 Conference Record of the Twenty-Eighth Asilomar Conference on Signals, Systems and Computers*, **1**, 41–44 (1994).

[19] Chen, S., Donoho, D., and Saunders, M., *SIAM Journal on Scientific Computing*, **20**(1), 33–61 (1998).

[20] Crommie, M. F., Lutz, C. P., and Eigler, D. M. *Science*, **262**(5131), 218–220 (1993).

[21] Damascelli, A., Hussain, Z., and Shen, Z.-X., *Reviews of Modern Physics*, **75**(2), 473–541 (2003).

[22] Das, A. and Kempe, D., in *Proceedings of the forty-first annual ACM symposium on Theory of computing*, 45–54 (2008).

[23] Das, A. and Kempe, D., in *Proceedings of the 28th International Conference on Machine Learning*, 1057–1064 (2011).

[24] Davies, E. and Gribonval, R., *IEEE Transactions on Information Theory*, **55**(5), 2203–2214 (2009).

[25] Doeleman, S. S., Fish, V. L., Schenck, D. E., Beaudoin, C., Blundell, R., Bower, G. C., Broderick, A. E., Chamberlin, R., Freund, R., Friberg, P., Gurwell, M. A., Ho, P. T. P., Honma, M., Inoue, M., Krichbaum, T. P., Lamb, J., Loeb, A., Lonsdale, C., Marrone, D. P., Moran, J. M., Oyama, T., Plambeck, R., Primiani, R. A., Rogers, A. A. E., Smythe, D. L., SooHoo, J., Strittmatter, P., Tilanus, R. P. J., Titus, M., Weintroub, J., Wright, M., Young, K. H., and Ziurys, L. M., *Science*, **338**(6105), 355–358 (2012).

[26] Donoho, D. L., *Discrete & Computational Geometry*, **35**(4), 617–652 (2006).

[27] Donoho, D. L., *Communications on Pure and Applied Mathematics*, **59**(6), 797–829 (2006).

[28] Donoho, D. L. and Elad, M., *Proceedings of the National Academy of Sciences of the United States of America*, **100**(5), 2197–2202 (2003).

[29] Donoho, D. L. and Huo X., *IEEE Transactions on Information Theory*, **47**(7), 2845–2862 (2001).

[30] Donoho, D. L., Maleki, A., and Montanari, A., *Proceedings of the National Academy of Sciences of the United States of America*, **106**(45), 18914-18919 (2009).

[31] Donoho, D. L. and Tanner, J., *Proceedings of the National Academy of Sciences of the United States of America*, **102**(27), 9452–9457 (2005).

[32] Efron, B. and Gong, G., *The American Statistician*, **37**(1), 36–48 (1983).

[33] Elad, M. and Bruckstein, A. M., *IEEE Transactions on Information Theory*, **48**(9), 2558–2567 (2002).

[34] Ferrenberg, A. M. and Swendsen, R. H., *Physical Review Letters*, **61**(23), 2635–2638 (1988).

[35] Fisher, Ø, Kugler, M., Maggio-Aprile, I., Berthod, C., *Reviews of Modern Physics*, **79**(1), 353–419 (2007).

[36] Foucart, S., *Applied and Computational Harmonic Analysis*, **29**(1), 97–103 (2010).

[37] Foucart, S. and Lai, M-J., *Applied and Computational Harmonic Analysis*, **26**(3), 395–407 (2009).

[38] Foucart, S. and Rauhat, H., *A Mathematical Introduction to Compressive Sensing*, Springer, Berlin (2013).

[39] Franz, S. and Parisi, G., *Physical Review Letters*, **79**(13), 2486–2489 (1997).

[40] Ganguli, S. and Sompolinsky, H., *Physical Review Letters*, **104**(18), 188701-1–188701-4 (2010).

[41] Geman, S. and Geman, D., *IEEE Transactions on Pattern Analysis and Machine Intelligence*, **PAMI-6**(6), 721–741 (1984).

[42] Grünbaum, B., *Convex Polytopes*, Springer, New York (2003).

[43] Hanaguri, T., Lupien, C., Kohsaka, Y., Lee, D. H., Azuma, M., Takano, M., and Davis, J. C., *Nature*, **430**(7003), 1001–1005 (2004).

[44] Hanaguri, T., Kohsaka, Y., Davis, J. C., Lupien, C., Yamada, I., Azuma, M., Takano, M., Ohishi, K., Ono, M., and Takagi, H., *Nature Physics*, **3**(12), 865–871 (2007).

[45] Hanaguri, T., Niitaka, S., Kuroki, K., and Takagi, H., *Science*, **328**(5977), 474–476 (2010).

[46] Harison, W. A., *Surface Science*, **55**(1), 1–19 (1976).

[47] Hasegawa, Y, and Avouris, Ph., *Physical Review Letters*, **71**(7), 1071–1074 (1993).

[48] Hasemi, A. H., Ishii, H., and Takagi, A., *Tectonophysics*, **101**(3–4), 245–265 (1984).

[49] Heinze, S., von Bergmann, K., Menzel, M., Brede, J., Kubetzka, A., Wiesendanger, R., Bihlmayer, G., and Blügel, S., *Nature Physics*, **7**, 713–718 (2011).

[50] Hirahara, K., *Journal of Physics of the Earth*, **25**(4), 393–417 (1977).

[51] Hirahara, K., *Journal of Physics of the Earth*, **28**(3), 221–241 (1980).

[52] Hoffman, J. E., McElroy, K., Lee, D.-H., Lang, K. M., Eisaki, H., Uchida, S., and Davis, J. C., *Science*, **297**(5584), 1148–1151 (2002).

[53] Holland, D. J., Bostock, M. J., Gladden, L. F., and Nietlispach, D., *Angewandte Chemie International Edition*, **123**(29), 6678–6681 (2011).

[54] Honma, M., Akiyama, K., Uemura, M., and Ikeda, S., *Publications of the Astronomical Society of Japan*, **66**(5), 95-1–95-14 (2014).

[55] Hsieh, D., Qian, D., Wray, L., Xia, Y., Hor, Y. S., Cava, R. J., and Hasan, M. Z., *Nature*, **452**(7190), 970–974 (2008).

[56] Hukushima, K. and Nemoto, K., *Journal of the Physical Society of Japan*, **65**(6), 1604–1608 (1996).

[57] Ichikawa, H., Kitazono, J., Nagata, K., Manda, A., Shimamura, K., Sakuta, R., Okada, M., Yamaguchi, M. K., Kanazawa, S., and Kakigi, R., *Frontiers in Human Neuroscience*, **8**(480), 1–10 (2014).

[58] Igarashi, Y., Nagata, K., Kuwatani, T., Omori, T., Nakanishi-Ohno, Y., and Okada, M., *Proceedings of International Meeting on "High-Dimensional Data Driven Science" (HD^3-2015)* (2015).

[59] Kabashima, Y., Wadayama, T., and Tanaka, T., *Journal of Statistical Mechanics: Theory and Experiment*, **2009**, L09003-1–L09003-12 (2009).

[60] Kawamoto, T., Nakajima, J., Reynard, B., and Toh, H., *Earth Planets and Space*, **67**(46), 1–4 (2015).

[61] Kazimierczuk, K. and Orekhov, V. Y., *Angewandte Chemie International Edition* **50**(24), 5556–5559 (2011).

[62] Khachiyan, L. G., *USSR Computational Mathematics and Mathematical Physics*, **20**(1), 53–72 (1980).

[63] Kohavi, R., in *Proceedings of the Fourteenth International Joint Conference on Artificial Intelligence*, **2**(12), 1137–1143 (1995).

[64] Kuwatani, T., Nagata, K., Okada, M., and Toriumi, M., *Contributions to Mineralogy and Petrology*, **163**(3), 547–562 (2012).

[65] Kuwatani T., Nagata, K., Okada, M., and Toriumi, M., *Earth, Planets and Space*, **66**(5), 1–9 (2014).

[66] Kuwatani T., Nagata, K., Okada, M., and Toriumi, M., *Physical Revoew E*, **90**(4) 042137-1–042137-7 (2014).

[67] Kuwatani, T., Nagata., K., Okada, M., Watanabe, T., Ogawa, Y., Komai, T., and Tsuchiya, N., *Scientific Reports*, **4**(7077), 1–6 (2014).

[68] Lander, J. J. and Morrison, J., *Journal of Applied Physics*, **34**(5), 1403–1410 (1963).

[69] Lattes, C. M. G., Occhialini G. P. S., and Powell, C. F., *Nature*, **160**(4066), 447–480 (1947).

[70] Lauterbur, P. C., *Nature*, **242**(5394), 190–191 (1973).

[71] Levine, J. D., McFarlane, S. H., and Mark, P., *Physical Review B*, **16**(12), 5415–5425 (1977).

[72] Lustig, M., Donoho, D., and Pauly, J. M., *Magnetic Resonance in Medicine*, **58**(6), 1182–1195 (2007).

[73] Lustig, M., Donoho, D. L., Santos, J. M., and Pauly, J. M., *IEEE Signal Processing Magazine* **25**(2), 72–82 (2008).

[74] Marr, D., *Vision*, MIT Press, Cambridge (1982).

[75] McElroy, K., Simmonds, R. W., Hoffman, J. E., Lee, D.-H., Orenstein, J., Eisaki, H., Uchida, S., Davis, J. C., *Nature*, **422**(6932), 592–596 (2003).

[76] Metropolis, N., Rosenbluth, A. W., Rosenbluth, M. N., Teller, A. H., and Teller, E., *The Journal of Chemical Physics*, **21**(6), 1087–1092 (1953).

[77] Miller, D. J., Haneman, D., and Walker, L. W., *Surface Science*, **94**(2–3), 555–563 (1980).

[78] Misawa, T. and Imada, M., *Nature Communications*, **5**(5738), 1-11 (2014).

[79] Miyake, T., Nakamura, K., Arita, R., and Imada, M., *Journal of the Physical Society of Japan*, **79**(4), 044705-1–044705-20 (2010).

[80] Mo, Q. and Li, S., *Applied and Computational Harmonic Analysis*, **31**(3), 460–468 (2011).

[81] Nagata, K., Kitazono, J., Nakajima, S., Eifuku, S., Tamura, R., and Okada M., *IPSJ Transactions on Mathematical Modeling and Its Applications*, **8**(2), 23–30 (2015).

[82] Nakanishi-Ohno, Y., Nagata, K., Shouno, H., and Okada, M., *Journal of Physics A: Mathematical and Theoretical*, **47**(4), 045001-1–045001-14 (2014).

[83] Nakanishi-Ohno, Y., Obuchi, T., Okada, M., and Kabashima, Y., submitted to *Journal of Statistical Mechanics*; arXiv:1510.02189.

[84] Nakanishi-Ohno, Y., Haze, M., Yoshida, Y., Hukushima, K., Hasegawa, Y., and Okada, M., in preparation.

[85] Natarajan, K., *SIAM Journal on Computing*, **24**(2), 227–234 (1995).

[86] Nishimori, H., *Statistical Physics of Spin Glasses and Information Processing: An Introduction*, Oxford University Press, Oxford (2001).

[87] Ohno, Y., Nagata, K., Kuwatani, T., Shouno, H., and Okada, M. *Journal of the Physical Society of Japan*, **81**(6), 064006-1–064006-6 (2012).

[88] Okada, Y., Dhital, C., Zhou, W., Huemiller, E. D., Lin, H., Basak, S., Bansil, A., Huang, Y.-B., Ding, H., Wang, Z., Wilson, S. D., and Madhavan, V., *Physical Review Letters*, **106**(20), 206805-1–206805-4 (2011).

[89] Pryce, J. M. and Bruce, A. D., *Journal of Physics A: Mathematical and General*, **28**(3), 511–532 (1995).

[90] Qi, X.-L. and Zhang, S.-C., *Reviews of Modern Physics*, **83**(4), 1057–1110 (2011).

[91] Reed, S., *Science*, **331**(6018), 696–697 (2011).

[92] Rish, I. and Grabarnik, G., *Sparse Modeling: Theory, Algorithms, and Applications*, CRC Press, Boca Raton (2014).

[93] Röntgen, W. C., *Science*, **3**(59), 227–231 (1896).

[94] Rodrigues, I., Sanches, J., and Bioucas-Dias, J., in *15th IEEE International Conference on Image Processing*, 1756–1759 (2008).

[95] Roushan, P., Seo, J., Parker, C. V., Hor, Y. S., Hsieh, D., Qian, D., Richardella, A., Hasan, M. Z., Cava, R. J., and Yazdani, A., *Nature*, **460**(7259), 1106–1109 (2009).

[96] Schlier, R. E. and Farnsworth, H. F., *The Journal of Chemical Physics*, **30**(4), 917–926 (1959).

[97] Shimomura, O., Johnson, F. H., and Saiga, Y., *Journal of Cellular and Comparative Physiology*, **59**(3), 223–239 (1962).

[98] Sugimoto, Y., Pou, P., Abe, M., Jelinek, P., Pŕez, R., Morita, S., and Custance, Ó, *Nature*, **446**, 64–67 (2007).

[99] Swendsen, R. H. and Wang, J.-S., *Physical Review Letters*, **57**(21), 2607–2609 (1986).

[100] Takenaka, H., Nagata, K., Mizokawa, T., and Okada, M., *Journal of the Physical Society of Japan*, **83**(12), 124706-1–124706-5 (2014).

[101] Tanaka, K., *Journal of Physics A: Mathematical and General*, **35**(37), R81–R150 (2002).

[102] Tibshirani, R., *Journal of the Royal Statistical Society. Series B (Methodological)*, **58**(1), 267–288 (1996).

[103] Tosatti, E. and Anderson, P. W., *Japanese Journal of Applied Physics*, **13**(S2), 381–388 (1974).

[104] Vershik, A. M. and Sporyshev, P. V., *Selecta Mathematica Sovietica*, **11**, 181–201 (1992).

[105] Vio, R., Bardsley, J., and Wamsteker, W., *Astronomy and Astrophysics*, **436**(2), 741–755 (2005).

[106] Wiesendanger, R., *Reviews of Modern Physics*, **81**(4), 1495–1550 (2009).

[107] Wiesendanger, R., Güntherodt, H. -J., Güntherodt, G., Gambino, R. J., and Ruf, R., *Physical Review Letters*, **65**(2), 247–250 (1990).

[108] Yoshida, Y., Schröder, S., Ferriani, P., Serrate, D., Kubetzka, A., von Bergmannm K., Heinze, S., and Wiesendanger, R., *Physical Review Letters*, **108**(8), 087205-1–087205-4 (2012).

[109] Yukawa, H., *Proceedings of the Physico-Mathematical Society of Japan. 3rd Series*, **17**, 48–57 (1935).

[110] Zhang, T., *IEEE Transactions on Information Theory*, **57**(9), 6215–6221 (2011).

[111] Zhang, T., Cheng, P., Chen, X., Jia, J.-F., Ma, X., He, K., Wang, L., Zhang, H., Dai, X., *Physical Review Letters*, **103**(26), 266803-1–266803-4 (2009).